DEPARTMENT OF PHYSICS
UNIVERSITY OF JYVÄSKYLÄ
RESEARCH REPORT No. 8/2007

FLOW BEHAVIOUR OF FIBRE SUSPENSIONS IN STRAIGHT PIPES: NEW EXPERIMENTAL TECHNIQUES AND MULTIPHASE MODELING

BY
ARI JÄSBERG

Academic Dissertation
for the Degree of
Doctor of Philosophy

To be presented, by permission of the
Faculty of Mathematics and Science
of the University of Jyväskylä,
for public examination in FYS-1of the
University of Jyväskylä on November 23, 2007
at 12 o'clock noon

Jyväskylä, Finland
October 2007

ISBN 978-951-39-3187-2
URN:ISBN:978-951-39-3187-2

Preface

The work described in this monograph has been carried out during the years 1995-2006 in the Department of Physics at the University of Jyväskylä.

First I would like to thank my supervisors Professor Jussi Timonen and Professor Markku Kataja for the possibility to work in the field of multiphase flows as a member of their group. Especially I would like to express my deep gratitude to Markku Kataja for his professional and encouraging guidance throughout these years. I also wish to thank Docent Antti Koponen, Dr. Pasi Raiskinmäki, Dr. Urpo Aaltosalmi, and Mr. Esa Rehn for their invaluable contributions to this thesis. For inspiring discussions in the field of physics and, most of all, on everyday life, I would like to thank my work-mates Dr. Markko Myllys, Dr. Jussi Maunuksela, Dr. Jari Hyväluoma, Docent Juha Merikoski, Mrs. Viivi Koivu, Mr. Janne Juntunen, Mr. Tuomas Turpeinen, Mr. Keijo Mattila, as well as all the others I may have forgotten to mention.

The financial support from the Finnish Funding Agency for Technology and Innovation (TEKES), the Academy of Finland, and the University of Jyväskylä is gratefully acknowledged.

Finally, I wish to thank my mother and parents-in-law for all kind of support (child care, housework, *etc.*) during these years. But most of all I would like to thank my beloved wife Anne for all encouragement, support, understanding and patience, and my daughter Charlotte and my son Jaani for all the happiness they give me every day.

Jyväskylä, October 2007

Ari Jäsberg

Author's contribution

The author has had an active role in all stages of the research described in this thesis. He has designed the laser-optical device for lubrication layer measurements, as well as carried out all the measurements with laser-optical and ultrasound techniques. He has done all the data analysis excluding the parameterization of turbulent velocity profiles in Chap. 6. He has also carried out single-particle simulations described in Chap. 3, and derived the two-phase model for the plug flow of wood fibre suspensions.

Abstract

Jäsberg, Ari
Flow behaviour of fibre suspensions in straight pipes: new experimental techniques and multiphase modeling
Jyväskylä: University of Jyväskylä, 2007, 171 p.
(Research report/Department of Physics, University of Jyväskylä,
ISSN 0075-465X; 8/2007)
ISBN 978-951-39-2937-4
diss.

The work described in this thesis consists of two main topics. First, the hydrodynamic forces acting on solid particles suspended in a flow of a Newtonian fluid were studied with direct numerical simulations. Second, the flow behaviour of wood fibre suspensions in straight pipes was studied.

The hydrodynamic forces acting on long solid cylinders suspended in a flow of Newtonian liquid near a solid wall were studied with direct numerical simulations separately for a single cylinder and a matrix of stationary cylinders with random positions. In the single-cylinder case, it was found that the nondimensional hydrodynamic drag and lift forces mainly depend on two nondimensional parameters, namely the dimensionless distance from the wall, and the ratio of the slip Reynolds number to the shear Reynolds number. It was found that the hydrodynamic force acting on a matrix of long cylinders is qualitatively similar both for unidirectional cylinders and for cylinders with random orientation. The drag force is largest near a moving wall and approaches zero monotonically with increasing distance from the wall. Close to the moving wall the simulated drag force deviates considerably from the drag force predicted by Darcy's law. Strongly repulsive lift force was found near the moving wall, and the maximum value of repulsion decreases as the the width of the gap between the moving wall and the matrix is increased. The total lift force acting on the cylinders was found strongly repulsive when the gap width is small, and decreases monotonically with increasing gap width. For unidirectional cylinders, the total lift force changes into attraction at the distance that is of the order of the cylinder radius.

The flow behaviour of wood fibre suspensions in straight pipes exhibits a peculiar plug-flow regime where frictional losses stay constant or even decrease with increasing flow rate. Moreover, in the turbulent regime the losses are usually lower than those for pure water at the same flow rate. New experimental methods were utilized in order to gain more detailed understanding on the flow behaviour and the relevant rheological material properties of wood fibre suspensions. The suspensions used in this study consisted of water and chemically released pine or birch fibres. The experiments were carried out with consistency 0.5–2.0% by weight in a flow loop with pipe diameter 40 mm. The thickness of a lubrication layer appearing in the plug-flow regime was determined by measuring the intensity of laser light reflected by fibres. An observable lubrication layer is found above the flow rate corresponding to the local maximum in the loss curve (birch) or to the point where the loss curve levels off (pine). The observed thickness of the layer decreases with increasing consistency, and the largest observed thickness was 0.4 mm and 0.11 mm for the pine and birch fibre suspensions, respectively. The transient behaviour of the flow after a sudden step that acted as a turbulence generator, approach to steady state flow, and the main features of fully developed flow were studied. The detailed time-dependent velocity profiles in such developing flow were measured with a pulsed ultra-sound velocimetry technique. From these velocity profiles, the local intensity of velocity fluctuations was calculated. Based on the results, it is proposed that the flow may be divided into five different regimes according to flow rate, namely plug flow with wall contact, plug flow with a lubrication layer, plug flow with a smearing annulus, mixed flow, and fully turbulent flow. A semiempirical correlation formula for the loss was derived by utilizing the modeled velocity profile in the plug flow regimes and the parametrized experimental velocity profile in the mixed and turbulent regimes.

Keywords wood fibre suspension, friction loss, plug flow, drag reduction, lubrication layer

Author's address Ari Jäsberg
Department of Physics
University of Jyväskylä
Finland

Supervisors Professor Markku Kataja
Department of Physics
University of Jyväskylä
Finland

Professor Jussi Timonen
Department of Physics
University of Jyväskylä
Finland

Reviewers Professor Jean-Francis Bloch
Paper Phys. Dept
Ecole Française de Papeterie et des Industries Graphiques
France

Docent Pentti Saarenrinne
Institute of Energy and Process Engineering
Tampere University of Technology
Finland

Opponent Professor Mark Martinez
Department of Chemical and Biological Engineering
University of British Columbia
Canada

Nomenclature

a, d	particle radius and diameter
R, D	pipe radius and diameter
c	percentage consistency (by weight)
c_m	consistency (by weight)
c_0, c_{m0}	threshold consistency for fibre network
C_{D}	drag coefficient
C_{L}	lift coefficient
E_α	total energy per unit mass
$\mathbf{F}_\alpha$	external force density
$\mathbf{F}_{\mathrm{D}}$	drag force
$\mathbf{F}_{\mathrm{L}}$	lift force
$\mathbf{g}$	gravitation vector
$J_{\mathrm{E}\alpha}$	heat source density
$\mathbf{J}_{\mathrm{q}\alpha}$	heat flux into phase α
k	permeability
K	dimensionless permeability
$\mathbf{M}_\alpha$	averaged interfacial momentum source terms for phase α
$\mathbf{W}_\alpha$	averaged interfacial momentum source terms for phase α
$\mathbf{D}$	volumetric drag force density
$\mathbf{L}$	volumetric lift force density
$\hat{\mathbf{n}}_\alpha$	outer unit normal vector of phase α
MR	moisture ratio
MR_{b}	moisture ratio of bound water
p_α	pressure of pure phase α
$\mathrm{R}e, \mathrm{R}e_p$	particle Reynolds number based on slip velocity

Re_γ	particle Reynolds number based on shear rate
v_p	particle velocity
$\mathbf{u}_\alpha$	velocity of pure phase α
$\mathbb{1}$	second rank unit tensor
$\langle f \rangle$	volume/ensemble average of f
$\tilde{f}$	phasic average of f
$\bar{f}$	de Favre average of f
s, f	subscripts for solid and liquid phase
x, y, z	subscripts for x,y, and z components of vector (tensor)
Q	volumetric flow rate
q	mean flow velocity
P	pressure

Greek symbols

Γ_α	rate of mass generation of phase α at phase interface
Γ_G	ratio of shear Renolds number to slip Reynolds number
θ	phase indicator characteristic function
μ_α	dynamic viscosity of phase α
ν_α	kinematic viscosity of phase α
ρ_α	density of pure phase α
σ_α	total stress tensor of phase α
τ_α	shear stress tensor of phase α
$\tau_{\delta\alpha}$	pseudo-turbulent stress tensor
τ_w	wall shear stress
$\sigma_{\alpha\beta}$	interface surface tension between phases α and β
ϕ_α	volume fraction of phase α
ϕ	porosity
ω	fibre coarseness

Contents

Chapter 1

Introduction

A central issue in many engineering problems involving fluid flow is estimating frictional losses. For simple Newtonian fluids, loss in a fully developed flow in a straight pipe is relatively accurately given by the famous Moody's diagram, or the related correlation formulas, which summarize the existing (yet incomplete) theoretical understanding on frictional flow in closed channels and a vast amount of carefully measured and analyzed experimental data.

The flows found in many industrial processes are inherently multiphase flows, and their behaviour is frequently much more complex than that of Newtonian liquids. For example, the flow behaviour of wood fibre suspensions in straight pipes exhibits a peculiar flow regime where frictional losses stay constant or even decrease with increasing flow rate. It has been known for a long time that in this regime the (more or less) rigid plug formed by fibres slide on top of a thin lubrication layer of pure water at pipe wall. Moreover, in the turbulent regime the losses are usually lower than those for pure water at the same flow rate. Although this flow behaviour is relatively well known, this general knowledge is not sufficient for providing us with loss correlations that are similar to those of Newtonian fluids. The practical design equations used in the industry are based on experimental correlations utilizing a large amount of data but relatively vague theoretical reasoning. The design principles are thus quite conservative and omit many fine details of the flow behaviour.

In this work, new experimental methods were utilized in order to gain more detailed understanding on the flow behaviour and the relevant rheological material properties of wood fibre suspensions. These methods have only recently become available, and they were partly developed during the experimental work described in this thesis. The suspensions used in this study consisted of water and chemically released pine or birch fibres. No fillers were used and the amount of fines was very low. During the experiments the consistency was varied between 0.5% and 2.0% by weight. Moreover, direct numerical simulation were performed to get qualitative insight into the relevant force interaction occurring in flows of wood fibre suspensions. The information extracted from these experiments and simulations was then utilized in an effort to develop improved methods for predicting frictional losses in straight pipe flow of fibre suspensions.

In the second chapter of this thesis equations are reviewed that govern the flows of multiphase systems consisting of two or more insoluble materials. Such flows are frequently found in various processes within, *e.g.*, paper and pulp industry, chemical industry and petroleum industry. At first the equations are stated in a general form that applies to a wide range of multiphase systems that consist of insoluble materials, and then refine the equations into specific form that can be used to solve flows of wood fibre suspensions.

The multi-phase equations that are recapitulated in the second chapter form a set of equations that are coupled with interaction terms. These interactions terms include, *e.g.*, the hydrodynamic forces acting between the phases. In the third chapter the hydrodynamic interactions in liquid-particle systems are studied by direct numerical simulations. Specifically, the hydrodynamic forces acting on stationary long cylinders suspended in a flow of Newtonian liquid near a solid wall are studied. Emphasis will be on the so-called lift force that is responsible for, *e.g.*, the lubrication layer in the plug flow regime of fibre suspension flow.

In the fourth chapter the somewhat peculiar flow behaviour of wood fibre suspensions in straight pipes is described at a qualitative level. Some characteristic features found in experimental frictional loss correlations are summarized after which various flow regimes are studied, and the flow phenomena are shortly discussed that are known to produce the observed loss correlation. Next the most relevant efforts on modeling the flow of wood fibre suspension in straight pipes and on design equations and methods for determining friction loss are reviewed.

In the fifth chapter the experimental work carried out in this study on the flow properties of wood fibre suspensions on straight pipes are described. New experimental methods were used to acquire better grasp on the flow phenomena responsible for the peculiar flow properties. The thickness of the lubrication layer in the plug-flow regime was measured with a laser-optical device. The detailed time-dependent velocity profiles in a developing flow were measured with a pulsed ultra-sound velocimetry techniques. The experimental results are extensively analyzed, and based on the results, a plausibler explanation to the observed flow behaviour is proposed. While still qualitative, this explanation contains more detailed physical reasoning than the previous studies on the phenomenon; it is based on direct and detailed measurements of flow profiles.

In the sixth chapter the correlations are derived that can be used to estimate frictional losses of wood fibre suspension flow in a straight pipe. This effort summarizes the work that has been described in the previous chapters, and it utilizes multiphase modeling results from the second chapter, numerical result of the third chapter, and the experimental results from the fifth chapter.

Chapter 2

Multiphase flow dynamics

2.1 Introduction

In this chapter the equations are presented that govern the flow of a multicomponent system consisting of two or more insoluble materials. In such a system each point can be identified as belonging to exactly one of the materials, thus the materials form distinct domains that are separated by well-defined boundaries. Different physical states of one material (solid, liquid, and gas) are usually treated as separate components of the system, thus a generic *phase* is used to refer to each of the components and the system is called a multiphase system.

Flows of insoluble multiphase systems include a wide range of flows found in industrial processes. Flows of insoluble liquids are common in oil extraction, while bubbly flows occur quite frequently in cooling systems and cavitation processes. Gas-particle suspensions or liquid-particle suspensions are characteristic to combustion processes as well as many processes in chemical industry. This work will concentrate on flows of liquid-particle suspensions, and especially on liquid-fibre suspensions that are fundamental within paper and pulp industry.

To start with, the generic equations governing the microscopic flow inside each phase are shortly reviewed, and various boundary conditions are described that can be applied on interphase boundaries and external boundaries of the system. In most of the practical cases (and most definitely in liquid-fibre suspensions) inter-phase boundaries have very complicated shape that may change with time, and one can not find an exact solution to the flow equations. The analytical studies are usually restricted to simple cases where there is, *e.g.*, one stationary solid object immersed in a flow field. There are computational methods, *e.g.* the lattice-Boltzmann method, that can be used to numerically solve flow fields in complex geometries that may change with time.

In analytical studies one have to resort to averaged equations, in general. To that end, the governing mesoscopic multiphase equations are derived by applying volume averaging on the microscopic flow equations. These averaged equations are at first given in a generic form that applies to many kinds of multiphase systems. These equations have to be equipped with additional closure relations that bring the equations into a closed form by taking into account specific features of the system under study. These relations include, *e.g.*, the forces acting between the phases. Basic principles are presented that have to be followed in inferring the closure relations for any multiphase system. Following these general guidelines, the closure relations are presented for liquid-particle suspensions, *i.e.* binary systems of solid particles suspended in a Newtonian liquid. Finally, the closure relations for flow in porous media are presented. These relations apply, *e.g.*, for plug flow regime of fibre suspensions where fibres form a rigid porous network through which water flows.

2.2 Microscopic flow equations

Consider a representative sample volume V which contains distinct domains of each phase such that $V = \sum_\alpha V_\alpha$ where V_α is the volume occupied by phase α within V (see Fig. 2.1). It is assumed that for each phase α the usual fluid mechanical equations for mass, momentum and energy conservation are valid at any interior point of V_α, namely

$$\frac{\partial}{\partial t}\rho_\alpha + \nabla\cdot(\rho_\alpha \mathbf{u}_\alpha) = 0 \tag{2.1}$$

$$\frac{\partial}{\partial t}(\rho_\alpha \mathbf{u}_\alpha) + \nabla\cdot(\rho_\alpha \mathbf{u}_\alpha \mathbf{u}_\alpha) = +\nabla\cdot\sigma_\alpha + \mathbf{F}_\alpha \tag{2.2}$$

$$\begin{aligned}\frac{\partial}{\partial t}(\rho_\alpha E_\alpha) + \nabla\cdot(\rho_\alpha \mathbf{u}_\alpha E_\alpha) &= \\ &+\nabla\cdot(\mathbf{u}_\alpha\cdot\sigma_\alpha) + \mathbf{u}_\alpha\cdot\mathbf{F}_\alpha - \nabla\cdot\mathbf{J}_{q\alpha} + J_{E\alpha}.\end{aligned} \tag{2.3}$$

Here,

ρ_α = density of pure phase α

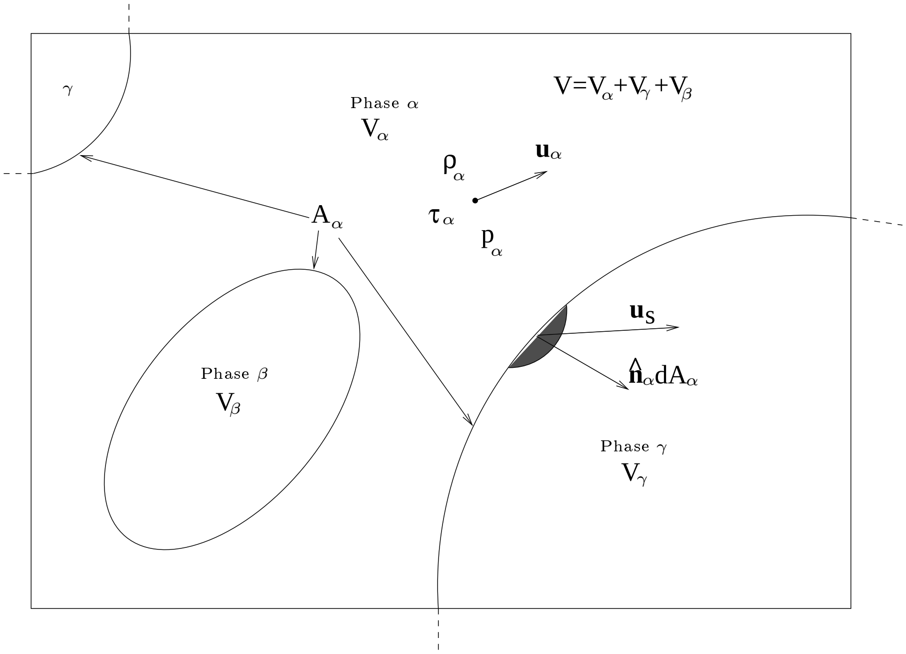

Figure 2.1: A control volume V including three phases α, β, and γ.

$\mathbf{u}_\alpha$ = flow velocity
σ_α = stress tensor
E_α = total energy per unit mass
$\mathbf{F}_\alpha$ = external force density
$\mathbf{J}_{q\alpha}$ = heat flux into phase α
$J_{E\alpha}$ = heat source density.

The energy equation (2.3) is necessary only in the presence of heat transfer. For simplicity, the energy equation will be neglected from now on and only mass and momentum equations will be considered.

For a fluid phase, the stress tensor is normally written in the form

$$\sigma_\alpha = -p_\alpha \mathbb{1} + \tau_\alpha, \tag{2.4}$$

where

p_α = pressure
$\mathbb{1}$ = second rank unit tensor
τ_α = traceless shear stress tensor

Hence the momentum equation becomes

$$\frac{\partial}{\partial t}(\rho_\alpha \mathbf{u}_\alpha) + \nabla \cdot (\rho_\alpha \mathbf{u}_\alpha \mathbf{u}_\alpha) = -\nabla p_\alpha + \nabla \cdot \tau_\alpha + \mathbf{F}_\alpha \tag{2.5}$$

Notice however, that the concept of 'pressure' is, in general, not useful for a solid material. In such cases it is preferable to use the total stress tensor σ_α and equation (2.2) instead.

In order to render the equations in closed form, constitutive relations stating the properties of individual phases have to be given. These relations relate the stress tensor to strain (solids) and/or rate of strain (fluids). For an incompressible fluid, this relation is commonly given in the form

$$\tau_\alpha = 2\mu_\alpha \epsilon_\alpha \tag{2.6}$$

where the rate of strain tensor is given by

$$\epsilon_\alpha = \frac{1}{2}\left((\nabla \mathbf{u}_\alpha) + (\nabla \mathbf{u}_\alpha)^{\mathrm{T}}\right) \tag{2.7}$$

and μ_α is the dynamic viscosity of the liquid. For a Newtonian liquid, viscosity is constant (may depend on temperature), while for a non-Newtonian liquid it may depend on, *e.g.*, on the local rate of strain ϵ_α.

2.2.1 Boundary conditions

Equations (2.1) and (2.2) for phase α are subject to the following jump conditions at the interface $A_{\alpha\gamma}$ between phase α and any other phase γ inside volume V (see Fig. 2.2).

$$\rho_\alpha(\mathbf{u}_\alpha - \mathbf{u}_{\mathrm{s}}) \cdot \hat{\mathbf{n}}_\alpha + \rho_\gamma(\mathbf{u}_\gamma - \mathbf{u}_{\mathrm{s}}) \cdot \hat{\mathbf{n}}_\gamma = 0 \tag{2.8}$$

$$\begin{aligned}\rho_\alpha \mathbf{u}_\alpha(\mathbf{u}_\alpha - \mathbf{u}_{\mathrm{s}}) \cdot \hat{\mathbf{n}}_\alpha + \rho_\gamma \mathbf{u}_\gamma(\mathbf{u}_\gamma - \mathbf{u}_{\mathrm{s}}) \cdot \hat{\mathbf{n}}_\gamma = \\ \sigma_\alpha \cdot \hat{\mathbf{n}}_\alpha + \sigma_\gamma \cdot \hat{\mathbf{n}}_\gamma - \nabla_{\mathrm{s}}\sigma_{\alpha\gamma} + \frac{2\sigma_{\alpha\gamma}}{|\mathbf{R}_{\mathrm{s}}|}\hat{\mathbf{R}}_{\mathrm{s}},\end{aligned} \tag{2.9}$$

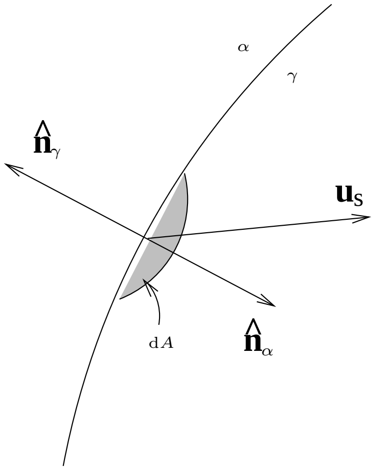

Figure 2.2: A portion of the interface between phases α and γ.

where

$\hat{\mathbf{n}}_\alpha$ = unit outward normal vector of phase α
$\mathbf{u}_\mathrm{s}$ = velocity of the interface
$\hat{\mathbf{R}}_\mathrm{s}$ = $\mathbf{R}_\mathrm{s}/|\mathbf{R}_\mathrm{s}|$
$\mathbf{R}_\mathrm{s}$ = interface curvature radius vector
$\sigma_{\alpha\gamma}$ = interface surface tension
∇_s = $\nabla - \hat{\mathbf{R}}_\mathrm{s} \cdot \nabla$ = surface gradient operator

Equations (2.8) and (2.9) express the conservation of mass and momentum at the interface, respectively. Terms on the left hand side of Eq. (2.9) give the momentum carried by the material crossing the interface due to phase change. The first two terms on the right side give the momentum exchange due to mechanical stresses. The remaining terms give the momentum transfer due to interface surface tension, and can usually be neglected at the interface involving solid phase.

In principle, equations (2.1) and (2.2) can be solved for a selected phase to get a detailed flow field. To pick up the specific solution, proper boundary conditions must be specified at each point of the boundary of the phase. In addition to the boundaries with other phases, this may also include parts of the external boundary of the entire system under study. In addition to the jump conditions (2.8) and (2.9) which are valid for all interfaces, boundary conditions should take into account the material and case dependent special features of the interface. Furthermore the interface $A_\alpha = \bigcup_\gamma A_{\alpha\gamma}$ may have a very complicated shape which depends on time and which actually should be solved simultaneously with the flow equations.

There are three general classes of boundary conditions. Dirichlet's boundary condition specifies the value of an unknown quantity at the boundary. In the present case the unknown quantity is flow velocity, and the boundary condition can be written as

$$\mathbf{u}_\alpha = \mathbf{u}_{\mathrm{Dir}}. \tag{2.10}$$

where $\mathbf{u}_{\mathrm{Dir}}$ is the known flow velocity at the boundary. This condition is often used to set a no-slip condition for a fluid phase at the solid boundary by setting $\mathbf{u}_{\mathrm{Dir}}$ equal to the local velocity of the solid surface. This condition can also be used to specify the flow velocity at the inlet and outlet boundaries of the system.

Neumann's boundary condition imposes a constraint on the derivatives of an unknown quantity. The stress tensor depends on the gradient of the velocity field, thus a special case of Neumann's boundary condition can be written in the form

$$\sigma_\alpha \cdot \hat{\mathbf{n}}_\alpha = \sigma_{\mathrm{Neu}}. \tag{2.11}$$

where σ_{Neu} is the known stress at the boundary. In some cases the friction at the interface can be neglected and the tangential shear stress set to zero. This may happen, *e.g.*, at a gas-liquid interface, where the shear stress of the liquid can be approximately neglected due to relatively low viscosity of the gas phase.

Robin's boundary condition is a combination of the two first types

$$\sigma_\alpha \cdot \hat{\mathbf{n}}_\alpha + \mathbf{A}_{\mathrm{Rob}} \cdot \mathbf{u}_\alpha = \sigma_{\mathrm{Rob}}. \tag{2.12}$$

This boundary condition is far less frequently used compared to Dirichlet's and Neumann's boundary conditions. It has been used, *e.g.*, for the outflow through the tube bank when calculating the flow of dilute fibre suspension inside head box of paper machine[Häm93].

In the context of continuum fluid mechanics, the no-slip boundary condition at the solid-fluid interface is quite often considered as an exact law of nature. However, it is only an approximate result which breaks down when the Knudsen number becomes large. A practical case of such breakdown is gas flow in micron-sized channels in some modern Micro-Electro-Mechanical-Systems (MEMS) [MRC02]. The Knudsen number Kn is defined as the ratio of the mean-free path of the fluid molecules λ to the characteristic length scale of the flow field L,

$$\mathrm{Kn} = \frac{\lambda}{L}. \tag{2.13}$$

For internal flows, L is the length scale associated with the volume available to the flow, *e.g.* the diameter of the flow channel, while for external flows L is the characteristic scale of the object immersed in the flow. The mean-free path for ideal gas at standard temperature and pressure is approximately $\lambda = 10^{-7}$ m, hence the Knudsen number for a micron-sized channel is $\mathrm{Kn} = 0.1$. This is just at the limit where the continuum flow assumption begins to fail, and the gas cannot be considered to be in a thermodynamic equilibrium anymore. Above this limit the system must be solved by using kinetic theory and Boltzmann's equation. Moreover, even well below this limit, *i.e.* when the continuum approach is justified, the no-slip condition may not be valid at the interface. This can be shown with a simple model where the kinetic theory is used near the interface and continuum approach for the rest of the flow [MRC02]. The slip velocity v_{slip} predicted by such a model is a special case of Robin's boundary condition (2.12):

$$v_{\text{slip}} = \frac{2-\sigma}{\sigma}\frac{\lambda}{\mu_\alpha}\tau_{\text{wall}} \tag{2.14}$$

where τ_{wall} is the tangential shear stress at the interface, and σ is the tangential accommodation coefficient. This dimensionless number gives the relative amount of the tangential momentum lost by gas molecules as they collide with the solid phase. For an idealized interface (perfectly smooth) the molecules conserve their tangential momentum ($\sigma = 0$), whereas in the case of an extremely rough surface, the molecules lose, on average, their entire tangential momentum ($\sigma = 1$). For very smooth interfaces, the slip velocity is thus large or, putting it the other way round, tangential shear stress is small.

It is straightforward to show that for laminar flow in a pipe of circular cross-section, the ratio of the slip velocity given by Eq. (2.14) to the average flow velocity q is given by

$$\frac{v_{\text{slip}}}{q} = 8\mathrm{Kn} \tag{2.15}$$

where the Knudsen number is defined with pipe diameter D, *i.e.* $\mathrm{Kn} = \frac{\lambda}{D}$ As an example, consider the flow of oxygen at the normal temperature $T = 273.15\,\mathrm{K}$ and at the pressure $P = 750\,\mathrm{mmHg} = 100.0\,\mathrm{kPa}$. The mean free path of oxygen in this state is $\lambda = 90.5\,\mathrm{nm}$ [Wea74]. In order to keep the velocity ratio given by Eq. (2.15) below 5%, the Knudsen number should be less than 0.00625. Hence, the minimum pipe diameter would be $D = 14\,\mu\mathrm{m}$.

Due to many complicated features discussed above, it is not always possible to apply the boundary conditions and to solve the microscopic equations (2.1) and (2.2) in the usual manner. This is the basic reason why one have to resort to averaged equations, in general. These averaged equations are reviewed in the next section.

2.3 Multiphase equations

In this section the 'equations of multi-phase flow' appropriate within the Eulerian approach are reviewed by closely following the approach used by Soo [Soo90]. First, suitable averaged dynamic flow quantities are defined, and then the required flow equations are derived by averaging the corresponding 'microscopic' phasial equations (2.1), and (2.2). For derivation of the energy equation for multi-phase flows see *e.g.* Refs. [Soo90] and [Hwa89].

The averaging procedure can be carried out in several alternative ways. Perhaps the most common approaches are time averaging [Ish75, Dre83], volume averaging [Ish75, Dre83, Soo90, Dre71, DS71, Nig79] and ensemble averaging [Ish75, Dre83, Buy71, Hwa89, JL90]. Various combinations of these basic methods can also been considered [Ish75]. Also, a homogenization method of multiple-scale asymptotic expansions has been used to derive the governing equations at the mesoscopic level from the microscopic equations [BA98, CP07]. It appears, however, that irrespectively of the method used, the averaging procedure leads to equations of the same generic form, namely the form of the original phasial equations except for a few additional terms which include the interactions *i.e.* exchange of mass, momentum and energy between the phases. Each averaging procedure may, however, provide a slightly different view in the physical interpretation of the interaction terms and, consequently, may suggest different solutions to the closure problem that is invariably associated with the solution of these equations. The manner, in which the various possible interaction mechanisms are naturally divided between these additional terms, may also depend on the averaging procedure being used. While ensemble averaging appears as the most elegant approach from the theoretical point of view, volume averaging provides perhaps the most intuitive and straightforward interpretation of the dynamic quantities and interaction terms involved. Volume averaging also illustrates the potential problems and intricacies that are common to all averaging methods. Thus the study is restricted to volume averaging method which is based on the assumption that a length scale L_c exists such that $L_m << L_c << L_S$, where L_m is the 'mesoscopic' length scale associated with the distribution of the various phases within the mixture and L_S is the 'macroscopic' length scale of the entire system.

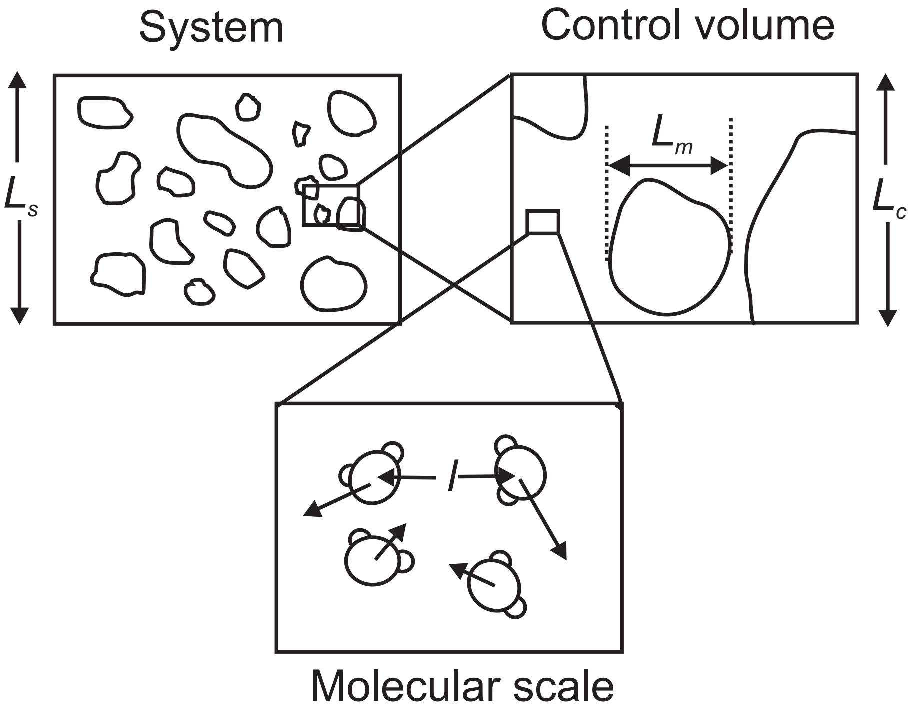

Figure 2.3: Characteristic length scales in a multiphase flow system.

2.3.1 Volume Averaged Equations

For any quantity q_α (scalar, vector or tensor) defined in phase α the following averages are defined [Ish75, Hwa89]

$$\langle q_\alpha \rangle = \frac{1}{V}\int_{V_\alpha} q_\alpha \, dV \tag{2.16}$$

$$\tilde{q}_\alpha = \frac{1}{V_\alpha}\int_{V_\alpha} q_\alpha \, dV = \frac{1}{\phi_\alpha}\langle q_\alpha \rangle \tag{2.17}$$

$$\bar{q}_\alpha = \frac{\int_{V_\alpha} \rho_\alpha q_\alpha \, dV}{\int_{V_\alpha} \rho_\alpha \, dV} = \frac{\langle \rho_\alpha q_\alpha \rangle}{\phi_\alpha \tilde{\rho}_\alpha}, \tag{2.18}$$

where

$$\phi_\alpha = V_\alpha / V. \tag{2.19}$$

is the volume ratio of phase α and is subject to the constraint that

$$\sum_{\alpha} \phi_\alpha = 1. \tag{2.20}$$

The quantities defined by Eqs. (2.16), (2.17) and (2.18) are called the partial average, the intrinsic or phasic average and the Favré or mass weighted average of q_α, respectively. At this point the decision is postponed of which particular average of each flow quantity one should choose to appear as the final dynamic quantity of the averaged theory.

In order to derive the governing equations for the averaged quantities defined above, averaging is applied to the microscopic equations (2.1) and (2.2). To this end, it is first noticed that the following rules apply to the partial averages (and to the other two averages),

$$\langle f + g \rangle = \langle f \rangle + \langle g \rangle \tag{2.21}$$

$$\langle \langle f \rangle g \rangle = \langle f \rangle \langle g \rangle \tag{2.22}$$

$$\langle C \rangle = C \text{ for constant } C. \tag{2.23}$$

It is also rather straightforward to show that the following rules hold for partial averages of various derivatives of q_α [Soo90],

$$\langle \nabla q_\alpha \rangle = \nabla \langle q_\alpha \rangle + \frac{1}{V} \int_{A_\alpha} q_\alpha \hat{\mathbf{n}}_\alpha \, dA \tag{2.24}$$

$$\langle \nabla \cdot \mathbf{q}_\alpha \rangle = \nabla \cdot \langle \mathbf{q}_\alpha \rangle + \frac{1}{V} \int_{A_\alpha} \mathbf{q}_\alpha \cdot \hat{\mathbf{n}}_\alpha \, dA \tag{2.25}$$

$$\langle \frac{\partial}{\partial t} q_\alpha \rangle = \frac{\partial}{\partial t} \langle q_\alpha \rangle - \frac{1}{V} \int_{A_\alpha} q_\alpha \mathbf{u}_{\mathrm{s}} \cdot \hat{\mathbf{n}}_\alpha \, dA. \tag{2.26}$$

Applying partial averaging on both sides of Eqs. (2.1) and (2.2) and using Eqs. (2.21)-(2.26) the following equations are obtained

$$\frac{\partial}{\partial t} \langle \rho_\alpha \rangle + \nabla \cdot \langle \rho_\alpha \mathbf{u}_\alpha \rangle = \Gamma_\alpha \tag{2.27}$$

$$\frac{\partial}{\partial t} \langle \rho_\alpha \mathbf{u}_\alpha \rangle + \nabla \cdot \langle \rho_\alpha \mathbf{u}_\alpha \mathbf{u}_\alpha \rangle = -\nabla \langle p_\alpha \rangle + \nabla \cdot \langle \tau_\alpha \rangle + \langle \mathbf{F}_\alpha \rangle + \mathbf{M}_\alpha, \tag{2.28}$$

where the 'transfer integrals' Γ_α and $\mathbf{M}_\alpha$ are defined by

$$\Gamma_\alpha = -\frac{1}{V}\int_{A_\alpha} \rho_\alpha(\mathbf{u}_\alpha - \mathbf{u}_\mathrm{s})\cdot\hat{\mathbf{n}}_\alpha\, dA \tag{2.29}$$

$$\begin{aligned}\mathbf{M}_\alpha = {} & \frac{1}{V}\int_{A_\alpha} (-p_\alpha \mathbb{1} + \tau_\alpha)\cdot\hat{\mathbf{n}}_\alpha\, dA \\ & -\frac{1}{V}\int_{A_\alpha} \rho_\alpha \mathbf{u}_\alpha(\mathbf{u}_\alpha - \mathbf{u}_\mathrm{s})\cdot\hat{\mathbf{n}}_\alpha\, dA.\end{aligned} \tag{2.30}$$

Obviously, the flow equations (2.27) and (2.28) are not yet given in a closed form amenable for solution. Firstly, the properties of each pure phase are not specified at this point. Secondly, the transfer integrals (2.29) and (2.30), which include the interactions (mass and momentum transfer) between phases, are still given in terms of integrals of the original microscopic quantities over the unknown phase boundaries. The additional constitutive relations, which are required to specify the material properties and to relate the transfer integrals with the proper averaged quantities, are discussed in more detail below. Thirdly, averages of various products of original variables that appear on the left side of the equations are, in principle, independent of each other. Even in the case that all the necessary constitutive relations are assumed to be known, one still has more independent variables than equations for each phase. In order to reduce the number of independent variables, one must express averages of these products in terms of products of suitable averages. This can be done in several alternative ways which may lead to slightly different results. Here, Favré averaging is used for velocity and, depending on which is more convenient, either partial or intrinsic averaging is used for density and pressure. Defining the velocity fluctuation $\delta\mathbf{u}_\alpha$ by

$$\mathbf{u}_\alpha = \bar{\mathbf{u}}_\alpha + \delta\mathbf{u}_\alpha, \tag{2.31}$$

it is easy to see that the averages of products that appear in Eqs. (2.27) and (2.28) can be written as

$$\langle\rho_\alpha\mathbf{u}_\alpha\rangle = \langle\rho_\alpha\rangle\bar{\mathbf{u}}_\alpha = \phi_\alpha\tilde{\rho}_\alpha\bar{\mathbf{u}}_\alpha \tag{2.32}$$

$$\begin{aligned}\langle\rho_\alpha\mathbf{u}_\alpha\mathbf{u}_\alpha\rangle &= \langle\rho_\alpha\rangle\bar{\mathbf{u}}_\alpha\bar{\mathbf{u}}_\alpha + \langle\rho_\alpha\delta\mathbf{u}_\alpha\delta\mathbf{u}_\alpha\rangle \\ &= \phi_\alpha\tilde{\rho}_\alpha\bar{\mathbf{u}}_\alpha\bar{\mathbf{u}}_\alpha + \langle\rho_\alpha\delta\mathbf{u}_\alpha\delta\mathbf{u}_\alpha\rangle\end{aligned} \tag{2.33}$$

The averaged equations now acquire the form

$$\frac{\partial}{\partial t}(\phi_\alpha \tilde{\rho}_\alpha) + \nabla \cdot (\phi_\alpha \tilde{\rho}_\alpha \bar{\mathbf{u}}_\alpha) = \Gamma_\alpha \tag{2.34}$$

$$\frac{\partial}{\partial t}(\phi_\alpha \tilde{\rho}_\alpha \bar{\mathbf{u}}_\alpha) + \nabla \cdot (\phi_\alpha \tilde{\rho}_\alpha \bar{\mathbf{u}}_\alpha \bar{\mathbf{u}}_\alpha) = \\ -\nabla(\phi_\alpha \tilde{p}_\alpha) + \nabla \cdot \langle \tau_\alpha \rangle + \phi_\alpha \tilde{\mathbf{F}}_\alpha + \mathbf{M}_\alpha + \nabla \cdot \tau_{\delta\alpha}, \tag{2.35}$$

where

$$\tau_{\delta\alpha} = -\langle \rho_\alpha \delta \mathbf{u}_\alpha \delta \mathbf{u}_\alpha \rangle. \tag{2.36}$$

This tensor is sometimes called a pseudo-turbulent stress tensor since it is analogous to the usual Reynolds stress tensor of turbulent one-phase flow. Notice however, that tensor $\tau_{\delta\alpha}$ is defined here as a volume average instead of a time average as in the case of the usual Reynolds stress. It also contains momentum fluxes that arise both from the turbulent fluctuations of the microscopic flow and from the fluctuations of the velocity of phase α due to the presence of other phases. Consequently, tensor $\tau_{\delta\alpha}$ does not necessarily vanish even in the case that the microscopic flow is laminar.

Integrating the microscopic boundary conditions (2.8) and (2.9) over the interface $A_{\alpha\gamma}$, summing over α and γ and using definitions (2.29) and (2.30), it is found that

$$\sum_\alpha \Gamma_\alpha = 0 \tag{2.37}$$

$$\sum_\alpha \mathbf{M}_\alpha = -\frac{1}{2V} \sum_{\substack{\alpha,\gamma \\ \alpha \neq \gamma}} \int_{A_{\alpha\gamma}} (-\nabla_{\mathrm{s}} \sigma_{\alpha\gamma} + \frac{2\sigma_{\alpha\gamma}}{|\mathbf{R}_{\mathrm{s}}|} \hat{\mathbf{R}}_{\mathrm{s}}) dA. \tag{2.38}$$

Equation (2.37) ensures conservation of the total mass of the mixture, while the right side of Eq. (2.38) gives rise to surface effects such as 'capillary' pressure differences between various phases.

Equations (2.34) and (2.35) together with constraints (2.20), (2.37) and (2.38) are the most general averaged equations of multi-phase flow (with no heat transfer), which can be derived without reference to the particular properties of the system (other than the general continuum assumptions).

The basic dynamic variables of the averaged theory can be taken to be the three components of the mass-averaged velocities $\bar{\mathbf{u}}_\alpha$ and the volume fractions ϕ_α (or, alternatively, the averaged densities $\langle \rho_\alpha \rangle$). Provided that all the other variables and terms that appear in Eqs. (2.34) and (2.35) can be related to these basic variables using definitions (2.16) through (2.18), constraints (2.20), (2.37) and (2.38) and constitutive relations, one thus has a closed set of four unknown variables and four independent equations for each phase α.

2.3.2 Constitutive relations

Equations (2.34) and (2.35) are, in principle, exact equations for the averaged quantities. So far, they do not contain much information about the dynamics of the particular system to be described. That information must be provided by a set of system dependent constitutive relations which specify the material properties of each phase, the interactions between different phases and the (pseudo)turbulent stresses of each phase in the presence of other phases - and which finally render the set of equations in a closed form where solution is feasible.

At this point we do not attempt to elaborate in detail the possible strategies for attaining the constitutive relations in specific cases, but simply state the basic principles that may be followed in inferring such relations. The unknown terms that appear in the averaged equations (2.34) and (2.35), such as the transfer integrals and stress terms that still contain microscopic quantities, should be replaced by new terms which [Dre83]

- depend only on the averaged dynamic quantities (and their derivatives),
- have the same physical content, tensorial form and dimension as the original terms,
- have the same symmetry properties as the original terms (isotropy, frame indifference *etc.*),
- include the effects of all the physical processes or mechanisms that are considered to be important in the system to be described.

Typically, constitutive relations are given in a form where these new terms include free parameters which are supposed to be determined experimentally. For more detailed discussion on the constitutive relations and constitutive principles, see *e.g.* Refs. [DAL90, Dre83, DL79, Dre76, Hwa89, HS89, HS91, BS78, Buy92a, Buy92b].

In some cases constitutive laws can readily be derived from the microscopic properties of the mixture, or from the properties of the pure phase. If *e.g.* the pure phase α is incompressible *i.e.* $\rho_\alpha =$ constant, that implies the constitutive relation $\tilde{\rho}_\alpha$=constant. Similarly, the equation of state $p_\alpha = C\rho_\alpha$, where C=constant for the pure phase, implies $\tilde{p}_\alpha = C\tilde{\rho}_\alpha$. In most cases, however, the constitutive relations must be extracted from experiments, derived analytically under suitable simplifying assumptions, or postulated.

Including a given physical mechanism in the model by imposing proper constitutive relations is not, however, always very straightforward even in the case that adequate experimental and theoretical information is available. Especially making specific assumptions concerning one of the unknown quantities may induce constraints on other terms. For example, the transfer integrals Γ_α and $\mathbf{M}_\alpha$ contain the effect of exchange of mass and momentum between the phases. According to Eq. (2.29), the quantity Γ_α gives the rate of mass transfer per unit volume through the phase boundary A_α into phase α from the other phases. In a reactive mixture, where phase α is changed into phase γ, the mass transfer term Γ_α might be given in terms of the experimental rate of the chemical reaction $\alpha \rightarrow \gamma$ as correlated *e.g.* to the volume fractions ϕ_α and ϕ_γ, temperature of the mixture T *etc.* Similarly, the quantity $\mathbf{M}_\alpha$ gives the rate of momentum transfer per unit volume into phase α through the phase boundary A_α. The second integral on the right side of Eq. (2.30) contains the transfer of momentum carried by the mass exchanged between phases. It is obvious that this part of the momentum transfer integral $\mathbf{M}_\alpha$ must be consistently correlated with the mass transfer integral Γ_α. Similarly, the first integral on the right side of Eq. (2.30) contains the change of momentum of phase α due to stresses imposed on the phase boundary by the other phases. Physically, this term contains forces such as buoyancy which may be correlated to average pressures and gradients of volume fractions, and viscous drag which might be correlated to volume fractions and average velocity differences. For instance in a liquid-particle suspension, the average stress inside solid particles depends on the hydrodynamic forces acting on the surface of the particles. The choice of *e.g.* drag force correlation between fluid and particles should therefore influence the choice of the stress correlation for the particulate phase. While this particular problem can be solved exactly for idealized cases [DAL90], there seems to be no algorithm available for accomplishing this in a general case.

Perhaps the most intricate term which is to be correlated to the averaged quantities through constitutive relations is, however, the tensor $\tau_{\delta\alpha}$ given by Eq. (2.36). It contains the momentum transfer inside phase α, which arises from the genuine turbulence of phase α and from the velocity fluctuations that arise due to presence of other phases, and that are also present in the case that the microscopic flow is laminar. Moreover, the truly turbulent fluctuations of phase α may be substantially modulated by the other phases. Bearing in mind the intricacies that are encountered in modeling turbulence in single phase flows, it is evident that inferring realistic constitutive relations for tensor $\tau_{\delta\alpha}$ remains as a considerable challenge. It may, however, be attempted *e.g.* for fluid-particle suspensions by generalizing the corresponding models for single phase flows, such as turbulence energy dissipation models, large-eddy simulations or direct numerical simulations. A review on the topic is given by Crowe, Troutt and Chung in Ref. [CTC96].

It should be emphasized that no general set of equations exists that, as such, would be valid and readily solvable for an arbitrary multi-phase flow, or even for an arbitrary two-phase flow. Instead, for each particular system, the flow equations should be derived separately starting from the general (but unclosed) set of equations given in section (2.3) and utilizing all the specific assumptions and approximations that are plausible for that system.

Next two particular cases are discussed that are most relevant to this thesis, namely liquid-particle suspension and flow in the porous medium.

Liquid-particle suspension

Consider a binary system of solid particles suspended in a Newtonian liquid. The continuous fluid phase is denoted by subscript f and the dispersed particle phase by subscript s. It is assumed that both phases are incompressible, that the suspension is non-reactive *i.e.* there is no mass transfer between the two phases and that surface tension between solid and liquid is negligible. Both the densities $\tilde{\rho}_{\mathrm{f}}$ and $\tilde{\rho}_{\mathrm{s}}$ are thus constants, and

$$\begin{aligned} \Gamma_{\mathrm{f}} = \Gamma_{\mathrm{f}} &= 0 && (2.39) \\ \mathbf{M}_{\mathrm{f}} + \mathbf{M}_{\mathrm{s}} &= 0. && (2.40) \end{aligned}$$

The mutual momentum transfer integral can now be written as

$$\begin{aligned} \mathbf{M} \equiv \mathbf{M}_{\mathrm{f}} = -\mathbf{M}_{\mathrm{s}} &= \frac{1}{V} \int_{A_{\mathrm{f}}} (-p_{\mathrm{f}} \mathbb{1} + \tau_{\mathrm{f}}) \cdot \hat{\mathbf{n}}_{\mathrm{f}} \, dA \\ &= -\frac{1}{V} \int_{A} (-p_{\mathrm{f}} \mathbb{1} + \tau_{\mathrm{f}}) \cdot \hat{\mathbf{n}} \, dA, && (2.41) \end{aligned}$$

where $A = A_{\mathrm{f}} = A_{\mathrm{s}}$ and $\hat{\mathbf{n}} = \hat{\mathbf{n}}_{\mathrm{s}} = -\hat{\mathbf{n}}_{\mathrm{f}}$. Introducing the fluid pressure fluctuation by $\delta p_{\mathrm{f}} = p_{\mathrm{f}} - \tilde{p}_{\mathrm{f}}$, the momentum transfer integral can be written in a form

$$\mathbf{M} = \tilde{p}_{\mathrm{f}} \, (\frac{1}{V} \int_{A} \hat{\mathbf{n}} \, dA) + \mathbf{W}, \tag{2.42}$$

where

$$\mathbf{W} = -\frac{1}{V}\int_A (-\delta p_\mathrm{f}\mathbb{1} + \tau_\mathrm{f})\cdot\hat{\mathbf{n}}\,dA. \tag{2.43}$$

Next, the characteristic function of the dispersed phase $\theta_\mathrm{s}(\mathbf{r})$ is defined such that it has the value 1 if $\mathbf{r}$ is in the dispersed phase and 0 otherwise. Denoting $\phi \equiv \phi_\mathrm{f}$, whereby $\phi_\mathrm{s} = \langle\theta_\mathrm{s}\rangle = 1-\phi$, and applying Eq. (2.24) with $q_\alpha = \theta_\mathrm{s}(\mathbf{r})$, it is easy to see that

$$\frac{1}{V}\int_A \hat{\mathbf{n}}\,dA = \nabla\phi. \tag{2.44}$$

From Eq. (2.42) one thus gets

$$\mathbf{M} = \tilde{p}_\mathrm{f}\,\nabla\phi + \mathbf{W}. \tag{2.45}$$

The averaged flow equations can now be written as

$$\begin{aligned} \frac{\partial}{\partial t}\phi + \nabla\cdot(\phi\bar{\mathbf{u}}_\mathrm{f}) &= 0 && (2.46)\\ \frac{\partial}{\partial t}(1-\phi) + \nabla\cdot((1-\phi)\bar{\mathbf{u}}_\mathrm{s}) &= 0 && (2.47) \end{aligned}$$

$$\begin{aligned} \tilde{\rho}_\mathrm{f}[\frac{\partial}{\partial t}(\phi\bar{\mathbf{u}}_\mathrm{f}) + \nabla\cdot(\phi\bar{\mathbf{u}}_\mathrm{f}\bar{\mathbf{u}}_\mathrm{f})] &= -\phi\nabla\tilde{p}_\mathrm{f} + \nabla\cdot\langle\tau_\mathrm{f}\rangle + \phi\tilde{\mathbf{F}}_\mathrm{f}\\ &\quad +\mathbf{W} + \nabla\cdot\tau_{\delta\mathrm{f}} && (2.48)\\ \tilde{\rho}_\mathrm{s}[\frac{\partial}{\partial t}((1-\phi)\bar{\mathbf{u}}_\mathrm{s}) + \nabla\cdot((1-\phi)\bar{\mathbf{u}}_\mathrm{s}\bar{\mathbf{u}}_\mathrm{s})] &= +\nabla\cdot\langle\sigma_\mathrm{s}\rangle + (1-\phi)\tilde{\mathbf{F}}_\mathrm{s}\\ &\quad -\mathbf{W} - \tilde{p}_\mathrm{f}\,\nabla\phi + \nabla\cdot\tau_{\delta\mathrm{s}}, && (2.49) \end{aligned}$$

where $\langle\tau_\mathrm{f}\rangle$ is the averaged viscous stress tensor of the fluid, and $\langle\sigma_\mathrm{s}\rangle$ is the averaged total stress tensor of the dispersed phase. The first term on the right side of Eq. (2.45) is called buoyancy. Despite of its name, this term is not the buoyancy acting on immersed bodies as given by Archimedes' principle. In fact, Archimedes' buoyancy is proportional to the pressure gradient and is included in the first term on the right side of Eq. (2.48).

In the Eqs. (2.46)-(2.49) one has eight equations for the eight unknowns that can be taken to be the volume fraction of the fluid ϕ, fluid pressure $\tilde{p}_\mathrm{f}$ and the three components of both the velocities $\bar{\mathbf{u}}_\mathrm{f}$ and $\bar{\mathbf{u}}_\mathrm{s}$. It remains to specify the constitutive relations for the viscous stress tensor of the fluid $\langle\tau_\mathrm{f}\rangle$, the total stress tensor of the particulate phase $\langle\sigma_\mathrm{s}\rangle$, the momentum transfer integral $\mathbf{W}$, and the turbulent stresses $\tau_{\delta\mathrm{s}}$ and $\tau_{\delta\mathrm{f}}$.

The constitutive relation for the viscous stress tensor of the fluid $\langle\tau_{\mathrm{f}}\rangle$ can be derived simply by performing the volume averaging of the microscopic tensor $\tau_{\mathrm{f}} = \mu_{\mathrm{f}}((\nabla\mathbf{u}_{\mathrm{f}}) + (\nabla\mathbf{u}_{\mathrm{f}})^{\mathrm{T}})$ and using Eq. (2.24). The averaged surface velocity $\bar{\mathbf{U}}_{\mathrm{surf}}$ is defined by

$$\frac{1}{V}\int_{A_{\mathrm{f}}} \mathbf{u}_{\mathrm{f}}\hat{\mathbf{n}}_{\mathrm{f}}\, dA = \bar{\mathbf{U}}_{\mathrm{surf}}\frac{1}{V}\int_{A_{\mathrm{f}}} \hat{\mathbf{n}}_{\mathrm{f}}\, dA = -\bar{\mathbf{U}}_{\mathrm{surf}}\nabla\phi, \tag{2.50}$$

and postulate that $\bar{\mathbf{U}}_{\mathrm{surf}} = b\bar{\mathbf{u}}_{\mathrm{s}} - (1-b)\bar{\mathbf{u}}_{\mathrm{f}}$, where $b = b(\phi)$ is a free parameter (the 'mobility' of the dispersed phase) and acquires values between 0 and 1. It is then easy to see that the viscous stress tensor of the fluid can be given as

$$\langle\tau_{\mathrm{f}}\rangle = \phi\mu_{\mathrm{f}}\left((\nabla\bar{\mathbf{u}}_{\mathrm{f}}) + (\nabla\bar{\mathbf{u}}_{\mathrm{f}})^{\mathrm{T}}\right) - b\mu_{\mathrm{f}}((\nabla\phi)(\bar{\mathbf{u}}_{\mathrm{s}} - \bar{\mathbf{u}}_{\mathrm{f}}) + (\bar{\mathbf{u}}_{\mathrm{s}} - \bar{\mathbf{u}}_{\mathrm{f}})(\nabla\phi)), \tag{2.51}$$

which is identical to the result that Ishii stated without a proof[Ish75].

Flow in porous medium

Most porous materials of practical interest consist either of particles packed in a more or less disordered manner or of a consolidated irregular porous structure. Examples of such materials are numerous: sand, soil, fractured rock, ceramics, sponge, paper *etc.* Many important processes found in geophysics or in various industrial applications involve flow of fluid through a porous medium. In some cases, such as in slow transport of ground water through an aquifer, the porous material can be considered rigid so that the structure of the solid matrix is not significantly deformed during the process. The basic equation for such a flow is given by the famous Darcy's law, which was originally inferred from purely empirical results for a stationary creeping flow of Newtonian liquid through a homogeneous column of sand [Bea72]. With processes such as removal of water from a sponge by squeezing it, the porous structure appears soft and may thus be extensively deformed by external forces and by hydrodynamic forces exerted on the solid matrix by the fluid flow.

In this section, Darcy's experimental formula is utilized in the context of the multiphase flow theory and derive the governing equations for time dependent creeping flow of Newtonian liquid through a soft porous medium. Formally, the system of the highly deformable solid matrix and the liquid flowing through the interstities of the matrix is treated as a binary mixture of two fluids. It is assumed again that both phases are incompressible, that there is no mass transfer between the two phases and that surface tension between the solid material and the liquid is negligible. The situation is thus reminiscent to the liquid-particle suspension discussed in Section (2.3.2), and Eqs. (2.46)-(2.49) and (2.51) are valid for the present system. A few simplifications as compared to the liquid-particle suspension can, however, be made in this case. By assuming creeping flow the inertial terms that appear on the left side of Eqs. (2.48) and (2.49) can be neglected. Furthermore, the pseudoturbulent stress term $\nabla \cdot \tau_{\delta \mathrm{s}}$ vanishes in the solid phase and is expected to be very small also in the fluid phase in this flow regime. According to Darcy's early experiments and innumerable later experiments, the dominant interaction mechanism in a flow through porous medium is viscous drag $\mathbf{D}$. The results of these experiments, as summarized by the Darcy's law, indicate that the momentum transfer integral $\mathbf{W}$ should be written in a form

$$\mathbf{W} = \mathbf{D} = -\frac{\mu_{\mathrm{f}}}{k}(\bar{\mathbf{u}}_{\mathrm{f}} - \bar{\mathbf{u}}_{\mathrm{s}}). \tag{2.52}$$

Here, $k = k(\phi)$ is the permeability of the porous material, which remains to be determined.

Notice that permeability is, in general, a tensor of second rank and the momentum transfer vector may point to a direction that is not aligned with the velocity difference between the phases. However, in this monograph only isotropic materials will be considered for which the permeability is fully described by one scalar value k, and thus Eq. (2.52) applies.

Several experimental correlations for k have been reported in literature for different types of porous media (see *e.g.* ref. [Bea72]). Perhaps the most common formula which can be derived analytically for simplified capillary models of porous materials and which at least qualitatively grasps the correct behaviour for many materials, is the Kozeny-Carman relation

$$k = \frac{1}{cS_0^2}\frac{\phi}{(1-\phi)^2}. \tag{2.53}$$

Here, S_0 is the specific pore surface area and c is the dimensionless Kozeny constant which acquires values between 2 and 10, in practice. (Notice that due to the conventions used here, Eq. (2.53) differs from its more usual form where ϕ^3 instead of ϕ appears in the numerator, see Eq. (2.67) below.) The Kozeny-Carman relation does not predict well the permeability of fibrous porous materials with high porosity. There are several analytic results derived especially for fibrous porous materials that can be used for relatively high porosities. These results include,*e.g.*, the correlations derived by Happel [Hap59], by Kuwabara [Kuw59], and by Jackson and James [JJ86]:

$$\frac{k}{a^2} = \tfrac{1}{8\phi_\mathrm{s}(1-\phi_\mathrm{s})^2}\left(-\ln\phi_\mathrm{s} + \tfrac{\phi_\mathrm{s}^2-1}{\phi_\mathrm{s}^2+1}\right) \quad \text{(Happel)} \tag{2.54}$$

$$\frac{k}{a^2} = \tfrac{1}{8\phi_\mathrm{s}(1-\phi_\mathrm{s})^2}\left(-\ln\phi_\mathrm{s} - \tfrac{3}{2} + 2\phi_\mathrm{s}\right) \quad \text{(Kuwabara)} \tag{2.55}$$

$$\frac{k}{a^2} = \tfrac{3}{20\phi_\mathrm{s}(1-\phi_\mathrm{s})^2}\left(-\ln\phi_\mathrm{s} - 0.931\right) \quad \text{(Jackson and James)} \tag{2.56}$$

where $\phi_\mathrm{s} = 1 - \phi$ is the volume fraction of fibres, and a is the characteristic length scale of the permeability. All these results were derived for smooth uniradius cylinders, and a is the radius of cylinders. Eqs. (2.54) and (2.55) were derived for flow perpendicular to a rigid array of randomly placed parallel cylinders, while Eq. (2.56) is a weighted average of the permeabilities for flow parallel and perpendicular to an array of cylinders.

Ghaddar considered random porous media made of uniradius parallel cylinders and simulated flow perpendicular to the cylinders[Gha95]. He used solid volume fractions in the range 0.05–0.58 and found that the dependence on the volume fraction of the simulated permeability is described quite accurately by a simple exponential formula

$$\frac{k}{a^2} = 4.684\exp(-12.736\phi_\mathrm{s}). \tag{2.57}$$

Koponen et al simulated flow through fibrous porous material with the lattice-Boltzmann numerical method [KKH$^+$98]. They found the following interpolation formula for the simulated permeability

$$\frac{k}{a^2} = 5.55\left((1-\phi_\mathrm{s})^2(\exp(10.1\phi_\mathrm{s})-1)\right)^{-1} \tag{2.58}$$

The functional forms of the permeabilities given by Eqs. (2.54)–(2.56) and (2.58) are show in Fig. 2.4. Also shown in the figure are numerical results by Ghaddar[Gha95].

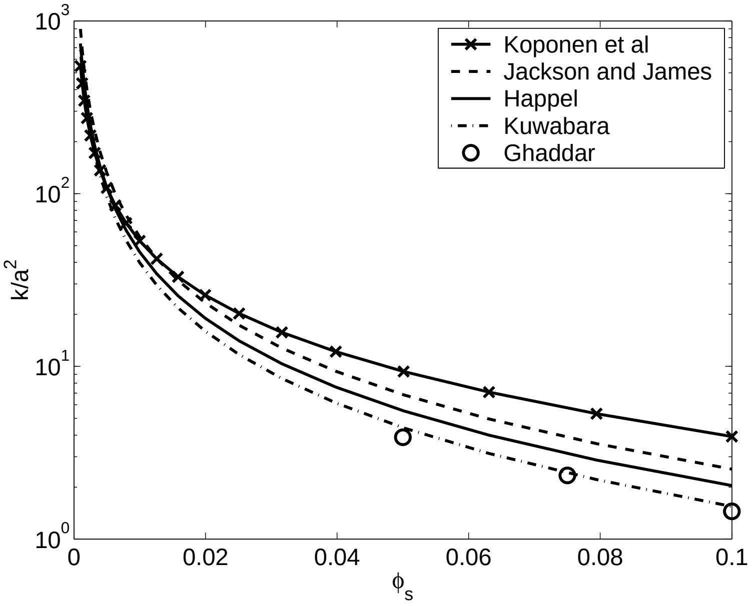

Figure 2.4: The permeabilities given by Eqs. (2.54)–(2.56) and (2.58) as functions of solid volume fraction ϕ_s. The open circles are the results corresponding to the lowest three solid volume fractions used in Ref. [Gha95].

If the porosity ϕ is not too close to unity, the viscous shear stress term $\nabla \cdot \langle \tau_\mathrm{f} \rangle$ is small compared to the viscous drag term and can be neglected. Taking gravitation to be the only body force, the equations for a flow of liquid in a deformable porous medium can thus be written in a form

$$\begin{aligned} \frac{\partial}{\partial t}\phi + \nabla\cdot(\phi\bar{\mathbf{u}}_{\mathrm{f}}) &= 0 && (2.59)\\ \frac{\partial}{\partial t}(1-\phi) + \nabla\cdot((1-\phi)\bar{\mathbf{u}}_{\mathrm{s}}) &= 0 && (2.60)\end{aligned}$$

$$\begin{aligned} \phi\nabla\tilde{p}_{\mathrm{f}} &= -\frac{\mu_{\mathrm{f}}}{k}(\bar{\mathbf{u}}_{\mathrm{f}}-\bar{\mathbf{u}}_{\mathrm{s}}) + \phi\tilde{\rho}_{\mathrm{f}}\mathbf{g} && (2.61)\\ -\nabla\cdot\langle\sigma_{\mathrm{s}}\rangle &= +\frac{\mu_{\mathrm{f}}}{k}(\bar{\mathbf{u}}_{\mathrm{f}}-\bar{\mathbf{u}}_{\mathrm{s}}) - \tilde{p}_{\mathrm{f}}\,\nabla\phi + (1-\phi)\tilde{\rho}_{\mathrm{s}}\mathbf{g}. && (2.62)\end{aligned}$$

Adding Eqs. (2.59) and (2.60) and Eqs. (2.61) and (2.62) one arrives at the mixture equations

$$\begin{aligned} \nabla\cdot\langle\mathbf{q}\rangle &= 0 && (2.63)\\ \nabla\cdot\langle\mathbf{T}\rangle &= -\langle\rho\rangle\mathbf{g}, && (2.64)\end{aligned}$$

where $\langle\mathbf{q}\rangle = \phi\bar{\mathbf{u}}_{\mathrm{f}} + (1-\phi)\bar{\mathbf{u}}_{\mathrm{s}}$ is the volume flux, $\langle\mathbf{T}\rangle = -\phi\tilde{p}_{\mathrm{f}}\mathbb{1} + \langle\sigma_{\mathrm{s}}\rangle$ is the total stress, and $\langle\rho\rangle = \phi\tilde{\rho}_{\mathrm{f}} + (1-\phi)\tilde{\rho}_{\mathrm{s}}$ is the density of the mixture.

For linearly elastic materials, the stress tensor $\langle\sigma_{\mathrm{s}}\rangle$ is readily given as a function of local strain by Hooke's law. For viscoelastic materials instead, $\langle\sigma_{\mathrm{s}}\rangle$ may depend both on the strain and on the rate of strain (*i.e.* on $\bar{\mathbf{u}}_{\mathrm{s}}$). The fact that the solid phase is actually not a fluid in an ordinary sense indicates that a finite stress implies finite strain on the solid matrix. It follows that the velocity of the solid phase can be non-zero only in a transient state. In a stationary state (and in the case of rigid porous material) one has $\bar{\mathbf{u}}_{\mathrm{s}} = \text{constant}$. The porosity ϕ is then independent of time, and in the frame of reference attached to the porous material (*i.e.* $\bar{\mathbf{u}}_{\mathrm{s}} = 0$) the flow equations are reduced to

$$\begin{aligned} \nabla\cdot\mathbf{q}_{\mathrm{f}} &= 0 && (2.65)\\ \mathbf{q}_{\mathrm{f}} &= -\frac{\bar{k}}{\mu_{\mathrm{f}}}(\nabla\tilde{p}_{\mathrm{f}} - \tilde{\rho}_{\mathrm{f}}\mathbf{g}), && (2.66)\end{aligned}$$

and one of equations (2.62) or (2.64). Here $\mathbf{q}_{\mathrm{f}} = \phi\bar{\mathbf{u}}_{\mathrm{f}}$ is the volume flux of the fluid (the 'seepage' velocity), and

$$\bar{k} = \frac{1}{cS_0^2}\frac{\phi^3}{(1-\phi)^2}. \qquad (2.67)$$

Eq. (2.66) is the Darcy's formula in its conventional form.

There are cases where the viscous shear stress term $\nabla \cdot \langle \tau_\mathrm{f} \rangle$ is of comparable magnitude with the viscous drag term and must be retained in the formulation. One example is the flow in a channel partly filled with porous medium surrounded by an annulus of pure liquid. It is evident that the shear field of pure liquid in the annulus penetrates the porous plug for some depth, and in some cases the flow field in this transitional region may be essential in analyzing the interactions, *e.g.* the lift force, between the phases. To solve the profile of average liquid velocity in this transitional region, the shear stresses inside the annulus and inside the plug must be matched at the plug surface. The viscous shear stress is given by Eq. (2.51). In the current case $\bar{\mathbf{u}}_\mathrm{s} =$ constant, thereby the averaged surface velocity of the fluid $\bar{\mathbf{U}}_\mathrm{surf}$ defined by Eq. (2.50) equals $\bar{\mathbf{u}}_\mathrm{s}$, and the mobility parameter b is unity. Hence, the averaged viscous shear stress tensor of the fluid can be written as

$$\langle \tau_\mathrm{f} \rangle = \phi \mu_\mathrm{f} \left((\nabla \bar{\mathbf{u}}_\mathrm{f}) + (\nabla \bar{\mathbf{u}}_\mathrm{f})^\mathrm{T} \right) - \mu_\mathrm{f}((\nabla \phi)\bar{\mathbf{u}}_\mathrm{s} + \bar{\mathbf{u}}_\mathrm{s}(\nabla \phi)). \tag{2.68}$$

There are also cases where one has to consider the momentum transfer between the phases in the direction perpendicular to the main flow, *i.e.* the hydrodynamic lift force. This force quite often plays an important role in flows near solid walls. It may have a remarkable effect on the flow properties of liquid-particle suspensions, and it is most likely responsible for a lubrication layer in the flow of wood-fibre suspension in straight pipes. In these cases, Eq. (2.52) is replaced with

$$\mathbf{W} = -\frac{\mu_\mathrm{f}}{k}(\bar{\mathbf{u}}_\mathrm{f} - \bar{\mathbf{u}}_\mathrm{s}) + \mathbf{L}. \tag{2.69}$$

where $\mathbf{L}$ is the volumetric lift force density acting on the fluid phase. This force points in the direction perpendicular to the velocity difference $\bar{\mathbf{u}}_\mathrm{f} - \bar{\mathbf{u}}_\mathrm{s}$. Notice that the lift force density $\mathbf{L}$ is solely due to the inertial effects in the flow, while the corresponding transverse component of the momentum transfer integral $\mathbf{M}$ includes the effect of buoyancy, as well (see Eq. (2.45)).

Now a generic set of equations is introduced that applies to the wide range of flows in porous medium with possible solid walls (exterior to porous medium) involved. To that end Eq. (2.69) is substituted for the interaction term $\mathbf{W}$ in Eqs. (2.48) and (2.47), and the inertial terms and the pseudoturbulent term of the solid phase are dropped. The resulting equations are

$$\begin{aligned} \phi \nabla \tilde{p}_\mathrm{f} &= \nabla \cdot \langle \tau_\mathrm{f} \rangle - \frac{\mu_\mathrm{f}}{k}(\bar{\mathbf{u}}_\mathrm{f} - \bar{\mathbf{u}}_\mathrm{s}) + \phi \tilde{\rho}_\mathrm{f} \mathbf{g} + \mathbf{L} + \nabla \cdot \tau_{\delta \mathrm{f}} && (2.70) \\ -\nabla \cdot \langle \sigma_\mathrm{s} \rangle &= +\frac{\mu_\mathrm{f}}{k}(\bar{\mathbf{u}}_\mathrm{f} - \bar{\mathbf{u}}_\mathrm{s}) - \tilde{p}_\mathrm{f} \, \nabla \phi + (1-\phi)\tilde{\rho}_\mathrm{s} \mathbf{g} - \mathbf{L}. && (2.71) \end{aligned}$$

together with the Eqs. (2.59) and (2.62) for the conservation of mass. Notice that the pseudoturbulent stress term of the fluid phase has been included in Eq. (2.70). It will be demonstrated in Sect. 3.4 that this term has a remarkable contribution to the hydrodynamic lift force acting on the solid particles near a moving wall. If one considers the first three terms of Eq. (2.70), they are quite similar to the famous equation that was derived by Brinkman [Bri47] to describe flow through a rigid bed of randomly deposited spherical particles. Brinkman extended the drag force on a sphere to include the effect of neighbouring spheres by combining the Stokes equation (Eq. (2.5) without time dependent and nonlinear terms and without external force) with Darcy's law:

$$\nabla p = \mu_{\mathrm{f}}' \nabla^2 u + \frac{\mu_{\mathrm{f}}}{K} u \tag{2.72}$$

where the viscosity μ_{f}' may differ μ_{f}. Notice that while Brinkman's derivation of Eq. (2.72) is a heuristic one, Eq. (2.70) was derived from basic single-phase flow equations by applying volume averaging.

To summarize, in this chapter the general multiphase flow equations were derived by volume averaging the microscopic flow equations of each phase. General principles of constitutive relations were discussed and the closure relations were reviewed for two cases that have importance within the scope of this monograph, namely liquid-particle suspension and flow in porous medium. These results will be utilized while studying the result of the direct numerical simulations in Chap. 3, and in deriving a multiphase model for the plug flow of wood fibre suspension in Chap. 6.

Chapter 3

Hydrodynamic interactions between fluid and solid particles

3.1 Introduction

In this chapter the hydrodynamic forces acting on stationary cylinders suspended in a shear flow of Newtonian fluid near a solid wall are studied. The numerical simulations described here were carried out in order to gain understanding on the dynamics of the lubrication layer found in the flow wood fibre suspensions in straight pipe.

The first goal of this study is to learn the basic features of hydrodynamic interactions between the fluid and a single stationary cylinder in a presence of a solid wall. This was achieved by numerically computing the drag coefficient and the lift coefficient of the cylinder for various flow conditions, and correlating the calculated coefficients with the relevant dimensionless parameters that characterize the flow. In order to gain qualitative understanding on the flow of fibre plug near a wall, a random rigid array of long cylinders suspended in a flow of a Newtonian fluid between two walls is considered.

3.2 Drag and lift forces acting on a single particle

Hydrodynamic forces acting on solid particles suspended in a flow of a Newtonian fluid have been studied for a long time. In middle 19's Stokes studied creeping flow of unbounded fluid past a rigid sphere and derived the famous formula for the drag force acting on the sphere [LL87],

$$F_{\mathrm{D}} = 6\pi\mu_{\mathrm{f}} a v. \tag{3.1}$$

Here F_{D} is the drag force, μ_{f} is the dynamic viscosity of the fluid, a is the radius of the sphere, and v is the velocity of the sphere. Since Stokes' zeroth order approximation Eq. (3.1) the concept of drag has been discussed by many authors and many higher order corrections to this formula have been reported [LL87, Lam75]. In the meantime, drag has also been measured in numerous experiments, and today one can find drag coefficients for various cases in standard handbooks [BT83]. From practical point of view, drag on submerged bodies is understood adequately.

The force acting on an immersed body in the direction that is orthogonal to the flow, the 'lift force' (or 'side force'), is not understood at such a comprehensive level. Especially, the lift force acting on a particle near a wall can have a remarkable effect on closed channel flows of suspensions, since the migration of particles away from the walls due to such a lift force can lead to a formation of a pure fluid layer next to the walls. This "lubrication layer" affects the flow properties of the suspension considerably, and contributes to the so-called drag reduction found in many suspension flows. A famous example of such a phenomenon is the flow of blood in small vessels [SS62]. Another example with industrial relevance is the pipe flow of paper pulp. It has also been reported that the lateral migration of particles may affect the experimental results from Couette-viscometry [SS62].

The effect of the lift force was already reported by Poiseuille, although the phenomenon was overlooked or misinterpreted at that time. It was the rigorous experiments deviced by Segre and Silberberg [SS62] for over a century after Poiseuille's work that undoubtedly demonstrated the existence of the lift force. Their experiments showed that spherical particles in laminar pipe flow migrate to a preferred radial position. This observation induced active theoretical study of the subject including both analytical considerations using perturbation theories, and direct numerical simulations (see Refs. [CM71, Lea80, Feu89, FHJ94] for a comprehensive review of experimental and theoretical work on the subject).

Notice that fluid dynamics text books, usually, cite only the two most famous results, namely the Saffman force and the Magnus force. These forces can be explained with the pressure difference due to different flow velocities on the opposite sides of a particle. Saffman derived the lift force acting on a sphere suspended in an unbounded shear flow [Saf65]. The Saffman force scales with the slip velocity between the fluid and the particle and with the square root of the shear rate of the undisturbed flow field. The Magnus force is the lift force that acts on a rotating cylinder suspended in a flow, and it scales with the angular velocity of the cylinder and the slip velocity [Whi94]. Notice however, that there are cases where the lift force appears much more complicated than the well-known Saffman force or Magnus force. Especially, the presence of solid walls modifies the lift force considerably[CM94].

Based on the reversibility argument one can show that a spherical particle suspended in a Stokes flow cannot experience any lift force [CM71]. The lift force observed experimentally thus arises due to inertial effects. In some cases one can estimate the magnitude of the lift force using an iterative procedure where the inertial terms are calculated at each iterative step using the next lower-order approximation of the flow field. In some specific occasions however (called 'effectively unbounded cases'), Stokes' solution can not be used as the zeroth order approximation throughout the flow domain. A famous example of such a case is the two-dimensional flow past a cylinder. Neglecting the inertia of the far field in such a flow leads in Whitehead's paradox, where the proper boundary conditions of the first order approximation can not be satisfied[PP57]. The reason for the discrepancy is that although Stokes' solution provides a good approximation to the flow velocity everywhere in the flow field, the velocity gradients used to calculate the inertial terms in the next order are seriously in error in the far field. One way to avoid Whitehead's paradox is to use the method of matched asymptotic expansions [PP57]. In this approach the flow in the viscous region near the particle is calculated using Stokes' equation while the flow in the inertial region far from the particle is calculated using Oseen's equation. The two solutions are matched in a narrow overlapping region. Using this technique Saffman [Saf65] derived an expression for the lift force acting on a sphere that moves and rotates in a linear shear field when the shear rate is high compared to the velocity difference between the sphere and undisturbed fluid. Later, McLaughlin [McL91] extended Saffman's result to allow weaker shear rates. Bretherton [Bre62] studied the lift force in a two-dimensional case and derived an expression for the lift force acting on a circular cylinder suspended in a simple shear flow $\mathbf{v} = (v_x + \gamma y)\hat{\mathbf{x}} + v_y\hat{\mathbf{y}}$ of unbounded fluid

$$\mathbf{F} = 4\pi\mu_{\mathrm{f}} a\gamma \left[\mathcal{R}\left(\frac{Hv_x + Kv_y}{\tau - \ln \mathrm{Re}_\gamma^{1/2}} \right) \hat{\mathbf{x}} + \mathcal{R}\left(\frac{Ev_x + Fv_y}{\tau - \ln \mathrm{Re}_\gamma^{1/2}} \right) \hat{\mathbf{y}} \right], \tag{3.2}$$

where $\mathcal{R}(z)$ is the real part of complex number z, and the complex constants are $E =$

$-2.11\,\mathrm{i}, F = -1 + 0.289\,\mathrm{i}, H = 1 + 0.289\,\mathrm{i}, K = -0.513\,\mathrm{i}$, and $\tau = 0.679 + 0.798\,\mathrm{i}$. The Reynolds number based on the shear rate is

$$\mathrm{Re}_\gamma = \frac{\rho_\mathrm{f} \gamma a^2}{\mu_\mathrm{f}}$$

where ρ_f is the density of the fluid and a is the radius of the cylinder. All these effectively unbounded theories predict a lift force that depends on viscosity and is linearly dependent on the velocity difference between the particle and undisturbed fluid flow [FHJ94].

Cox and Brenner[CB68] studied the lift force on a particle of arbitrary shape in a wall-bounded flow. As in most studies of wall-bounded flows, they assumed that the flow is effectively bounded, *i.e.*the wall lies within the viscous region of the particle, and that Stokes' equation alone is sufficient for calculating the lift force to the first order [CH77]. Effectively bounded theories predict lift force that does not depend on viscosity and is quadratically dependent on velocity [FHJ94]. Cox and Hsu [CH77] applied the theory developed by Cox and Brenner in two cases: a sphere sedimenting in a stagnant fluid and a sphere moving in a strong shear field. In the former case the particle was found to be always repelled away from the walls by a lift force

$$F_\mathrm{L} = a \mu_\mathrm{f} v_\mathrm{p} \mathrm{Re}_\mathrm{p} I = \rho_\mathrm{f} a^2 v_\mathrm{p}^2 I \tag{3.3}$$

where

$$I = \frac{18\pi}{32}. \tag{3.4}$$

and a is the radius of the sphere, v_p is the velocity difference between the sphere and undisturbed fluid flow, and Re_p is the corresponding Reynolds number:

$$\mathrm{Re}_\mathrm{p} = \frac{\rho_\mathrm{f} v_\mathrm{p} a}{\mu_\mathrm{f}}$$

According to that result, the lift force does not depend on the distance from the wall, thus the only equilibrium position of a particle sedimenting in a vertical cylindrical pipe would be at the axis of the pipe. In the latter case, they found that the lift force depends on the ratio of the shear rate γ to the slip velocity v_p [CH77, CM94]:

$$I = \frac{18\pi}{32} - \frac{66\pi}{64} \Lambda_G \left(\frac{l}{a} \right) + \frac{366\pi}{576} \Lambda_G^2 \tag{3.5}$$

where l/a is the dimensionless distance from the wall, and $\Lambda_G = \frac{\mathrm{Re}_\gamma}{\mathrm{Re}_\mathrm{p}} = \frac{\gamma a}{v_\mathrm{p}}$ the ratio of the

Reynolds numbers based on shear and slip:

$$\mathrm{Re}_\gamma = \frac{\rho_\mathrm{f}\gamma a^2}{\mu_\mathrm{f}}$$

With this result, it is possible that the lift force is repulsive near the wall, but becomes attractive at some distance from the wall. The equilibrium position of a particle moving in a cylindrical pipe with a shear flow may thus be at some radial distance from the axis of the pipe. This result is compatible with the experimental observations of Segre and Silberberg. Vasseur and Cox [VC77] studied a case where a spherical particle is sedimenting in a stagnant fluid bounded by a wall. They expressed I in a closed form as an complex integral that depends on the dimensionless distance from the wall $l^\star = \mathrm{Re}_\mathrm{p} l/a = \rho_\mathrm{f} v_\mathrm{p} a/\mu_\mathrm{f}$. In a case where $l^\star << 1$, *i.e.* particle is close to the wall, they found that

$$I = \frac{18\pi}{32}\left(1 - \frac{11}{32}(l^\star)^2 + \ldots\right) \tag{3.6}$$

For a large distance from the wall they found that

$$I = \frac{18\pi}{8}(l^\star)^{-2} + \frac{54\pi}{8}(2\pi)^{-2}K(\frac{1}{2})(l^\star)^{-5/2} + \ldots \tag{3.7}$$

where $K()$ is the complete elliptic integral of the first kind. Notice that the leading term of this expression, when substituted in Eq. (3.3), gives a lift force

$$F_\mathrm{L} = \rho_\mathrm{f} a^2 v_\mathrm{p}^2 \times \frac{3}{8}(l^\star)^{-2} = \frac{3{\mu_\mathrm{f}}^2}{8\rho_\mathrm{f}}, \tag{3.8}$$

that does not depend on sedimentation velocity v_p. To obtain the solution for the entire range of $l^\star$, a numerical integration of I must be undertaken. Vasseur and Cox gave the result as a plot, but it can be also found that I can be approximated with reasonable accuracy with an expression

$$I = \frac{18\pi}{32}\frac{1}{(l^*/l_0^*)^2 + 1}. \tag{3.9}$$

where $l_0^* \approx 2.6$ is the characteristic length scale of the lift force. For $l^* >> l_0^*$, *i.e.* case where the wall lies in the inertial region, the lift force depends on viscosity (l^* depends on viscosity). At the other limit $l^* << l_0^*$, Eq. (3.4) is obtained even though Cox and Hsu used completely different methods. At the distance $l_0^\star$ the lift force is half of this maximum value. Drew [Dre88] extended Saffmann's work by including the lift force induced by a wall in the inertial region, and found that such an effect cannot change the total lift force from attraction to repulsion. For most wall-bounded cases it was assumed that the distance between the sphere and the wall was large compared to the radius of the sphere and that the sphere can be treated as a point force or point force doublet acting on the fluid. Leighton and Acrivos [LA85] studied the case where the sphere was in contact with the wall, and they derived an expression for the lift force

$$F_{\mathrm{L}} = 9.22 a \mu_{\mathrm{f}} v_{\mathrm{p}} \mathrm{Re}_{\mathrm{p}} \tag{3.10}$$

where the slip velocity is $v_{\mathrm{p}} = \gamma a$ and the corresponding Reynolds number $\mathrm{Re}_{\mathrm{p}} = \rho_{\mathrm{f}} a v_{\mathrm{p}} / \mu_{\mathrm{f}}$. Cherukat and McLaughlin [CM94] studied the case where the distance from the wall and the radius of the sphere may be of comparable magnitude. They ended up with the result

$$F_{\mathrm{L}} = a \mu_{\mathrm{f}} v_{\mathrm{p}} \mathrm{Re}_{\mathrm{p}} I(l/a, \Lambda_G), \tag{3.11}$$

and the function I was given in the form of tables. For stagnant fluid, their result agrees with Eq. (3.4) for distances larger than $l/a > 6$. They also found that by setting $\Lambda_G = 1.0$ the lift approaches that given by Eq. (3.10) as $l/a \to 1$.

The analytical results discussed above are all based on perturbation methods and have quite a limited range of validity. The Reynolds numbers based on the slip velocity and on the shear rate were assumed small. Furthermore, in effectively bounded cases it was assumed that the Reynolds numbers are small compared to the dimensionless inverse distance from the wall [VC76]. This is a very restrictive condition when the particle is far away from the wall which, on the other hand, is a very common assumption in these theoretical approaches. The present author is not aware of any analytical work on wall-bounded flow past a particle in two-dimensional case.

3.3 Simulations: a single particle

The behaviour of hydrodynamic forces acting on a single particle suspended in a two-dimensional flow of Newtonian fluid near a rigid wall will now be studied. The forces are solved with direct numerical simulations in the flow regime where the Reynolds numbers defined by the cylinder radius and the slip velocity or the shear rate may be of the order of

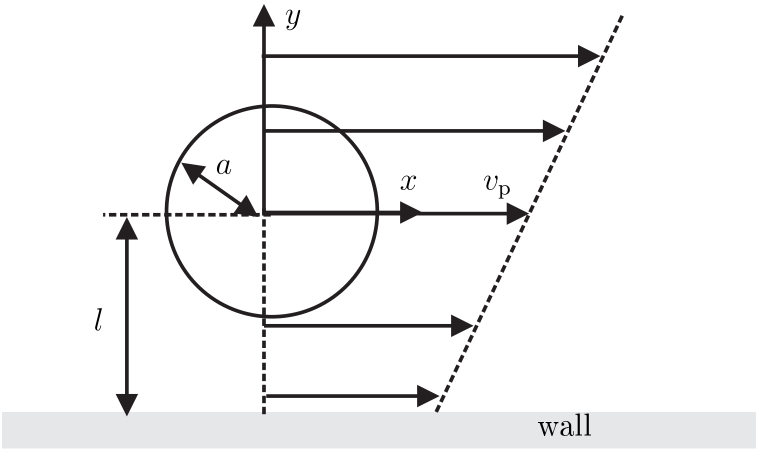

Figure 3.1: Infinitely long cylinder suspended in a semi-infinite plane Couette flow of a Newtonian incompressible fluid near a moving wall.

unity, and analytical solutions are not known. The primary purpose here is to gain qualitative understanding of the behaviour the relevant hydrodynamic forces rather than obtaining precise numerical results for a specified physical case. The approach is similar to that of Feng *et al.* [FHJ94] who studied the flow past a circular cylinder suspended in a Couette flow and in a plane Poiseuille flow between two parallel walls. In that work, lateral movement and the final equilibrium position of the particle were considered, whereas the present work addresses the hydrodynamic forces acting on the particle that is translating with a constant velocity parallel to the wall.

Let us consider a cylinder of infinite length and radius a suspended in a semi-infinite plane Couette flow of a Newtonian incompressible fluid near a moving, flat wall (see Fig. 3.1). The axis of the cylinder is parallel to the wall and perpendicular to the direction of flow. Hence, the flow may be treated as two-dimensional in a plane perpendicular to the axis of the cylinder. The cylinder is held at a fixed position. Undisturbed fluid velocity is given by

$$\mathbf{v}_\mathrm{f} = \left(v_\mathrm{p} + \gamma(y - l)\right)\hat{\mathbf{e}}_x \tag{3.12}$$

where v_p is the undisturbed fluid velocity at the centre of the cylinder, γ is the shear rate, and l is the distance between the axis of the cylinder and the wall. Here only positive values of v_p and γ are considered.

In what follows the longitudinal (drag) and lateral (lift) forces applied on the cylinder by the fluid per unit length of the cylinder are denoted by F_{D} and F_{L}, respectively. The cylinder radius a is chosen as the characteristic length scale, and the slip velocity v_{p} as the characteristic velocity scale of the problem. The drag and lift coefficients C_{D} and C_{L} of the cylinder are defined by

$$C_q = \frac{F_q}{2a \times \rho_{\mathrm{f}} v_{\mathrm{p}}^2/2}, \quad q = \mathrm{D}, \mathrm{L}, \tag{3.13}$$

where ρ_{f} is the density of the fluid. The other relevant nondimensional parameters of the problem can be chosen to be the inverse distance of the cylinder from the wall, and the two Reynolds numbers based on the slip velocity and on the shear rate. These parameters are defined by

$$\kappa = \frac{a}{l}; \qquad \mathrm{Re}_{\mathrm{p}} = \frac{v_{\mathrm{p}} a}{\nu_{\mathrm{f}}}; \qquad \mathrm{Re}_{\gamma} = \frac{\gamma a^2}{\nu_{\mathrm{f}}}. \tag{3.14}$$

Here ν_{f} is the kinematic viscosity.

The dimensionless shear rate is defined by the ratio of the two Reynolds numbers as

$$\Lambda_G \equiv \frac{\mathrm{Re}_{\gamma}}{\mathrm{Re}_{\mathrm{p}}} = \frac{\gamma a}{v_{\mathrm{p}}}. \tag{3.15}$$

Dimensional analysis results in the following relations between the coefficients:

$$C_q = C_q(\kappa, \mathrm{Re}_{\gamma}, \mathrm{Re}_{\mathrm{p}}), \quad q = \mathrm{D}, \mathrm{L}. \tag{3.16}$$

In this work the scaling laws, Eqs. (3.16), are studied using numerical simulations and utilizing previous analytical results when appropriate. The simulations were done in the rest frame of the particle using two commercial flow solvers (CFX [CFX94] and FLUENT [FLU98]) that are based on finite volume method. The length and the width of the simulation domain were $75a$ and $40a$, respectively. The cylinder was positioned near the lower wall approximately $25a$ downstream from the inlet. Both walls were made to move with constant (but different) velocities. The velocity field given by Eq. (3.12) was specified at the inlet and the flow was assumed to be fully developed at the outlet, *i.e.*dynamic quantities do not depend on x. No-slip condition was applied on all solid surfaces. The dimensionless inverse distance κ was varied from 0.111 to 0.84, the particle Reynolds number Re_{p} from 0.0 to 3.3, and the shear Reynolds number Re_{γ} from 0.0 to 0.25. The stationary flow field was found for all the 420 combinations of 14 values of Re_{p}, 6 values of Re_{γ}, and 5 values of κ. In each case the x and

y components (*i.e.*, the drag and lift forces, respectively) of the total force

$$\mathbf{F} = \oint_S \sigma \cdot \mathrm{d}\mathbf{S} \tag{3.17}$$

acting on the unit length of the cylinder were found. Here S is the surface per unit length of the cylinder and the total stress tensor of the fluid is given by

$$\sigma = -p\mathbf{1} + \mu_{\mathrm{f}} \left(\nabla\mathbf{v} + (\nabla\mathbf{v})^{\mathrm{T}} \right) \tag{3.18}$$

where p is the pressure, μ_{f} is the dynamic viscosity and $\mathbf{v}$ is the velocity of the fluid.

In Fig. 3.2 are shown all the calculated values of drag and lift coefficients as a function of the particle Reynolds number Re_{p} and for various values of the inverse distance κ and the shear Reynolds number Re_γ (values not indicated in the figure). Also shown is the Bretherton's analytical result (a cylinder in an infinite fluid) for the drag and lift coefficients and for a fixed value of Re_γ (see Eqs. (3.19) and (3.20) below). From Fig. 3.2 it is evident that the data scatter is quite large and that all the three dimensionless parameters $\mathrm{Re}_{\mathrm{p}}, \mathrm{Re}_\gamma$ and κ that appear in Eq. (3.16) indeed are essential in describing the behaviour of the drag and lift coefficients. The dependence on the particle Reynolds number of the drag coefficient, especially at small values of κ, is roughly of the form $1/\mathrm{Re}_{\mathrm{p}}$, which is in accordance with the Bretherton's result. The drag coefficient increases strongly with increasing κ, while its dependence on Re_γ is relatively weak in this region of parameter values. At small values of $1/\mathrm{Re}_{\mathrm{p}}$, the lift coefficient is positive corresponding to a repulsive lift force, and increases strongly with increasing κ. In a certain region of parameter values, the lift coefficient is negative corresponding to an attractive force towards the wall (see insert in Fig. 3.2 b). The dependence on Re_γ of the lift coefficient is always relatively strong.

The scaling law for the drag and lift coefficients given by the present numerical analysis is now studied. An appropriate analytic expressions is sought for that can be fitted to the computed data with a good confidence level. Here, former analytical results by Bretherton for unbounded flow are utilized [Bre62]. In the present case Bretherton's result can be written in an explicit form as

$$C_{\mathrm{D,B}} = \frac{4\pi}{\mathrm{Re}_{\mathrm{p}}} \frac{0.9096 - \frac{1}{2}\ln \mathrm{Re}_\gamma}{(0.679 - \frac{1}{2}\ln \mathrm{Re}_\gamma)^2 + 0.637}, \tag{3.19}$$

$$C_{\mathrm{L,B}} = -\frac{4\pi}{\mathrm{Re}_{\mathrm{p}}} \frac{1.684}{(0.679 - \frac{1}{2}\ln \mathrm{Re}_\gamma)^2 + 0.637}. \tag{3.20}$$

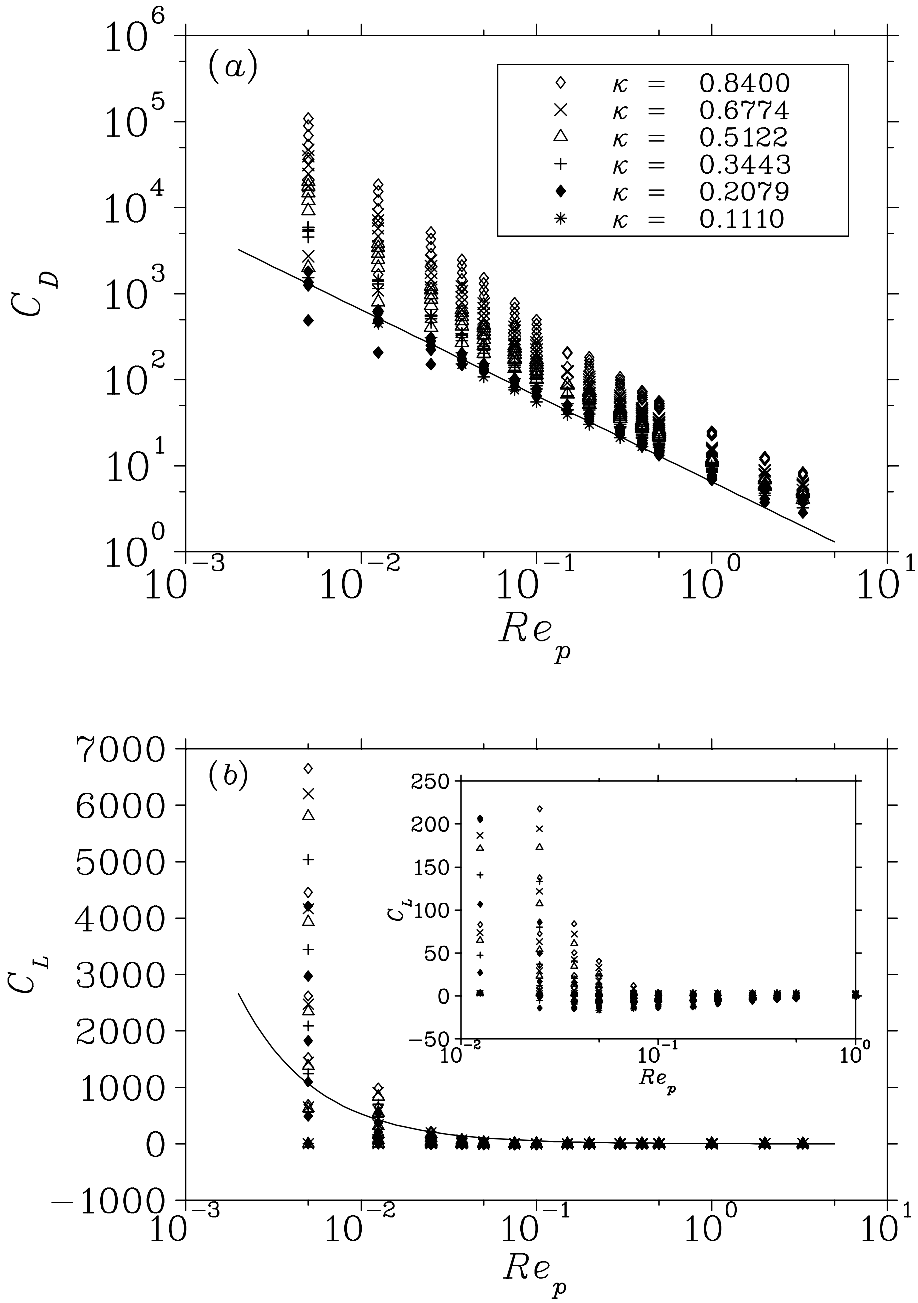

Figure 3.2: a) drag force coefficient C_{D} and b) lift force coefficient C_{L} vs slip Reynolds number $\mathrm{Re_p}$. Discrete points are the numerical results and the solid lines are the corresponding results derived by Bretherton, Eqs. (3.19) and (3.20), with $\mathrm{Re}_\gamma = 0.1$.

The behaviour of the coefficients $C_{q,\mathrm{B}}$, $q = \mathrm{D}, \mathrm{L}$ are also shown in Fig. 3.2 in the case that $\mathrm{Re}_\gamma = 0.1$. Notice that Bretherton's results are valid only for a limited range of the two Reynolds numbers. In particular, Bretherton's drag and lift coefficients both vanish as $\mathrm{Re}_\gamma \to 0$.

It appears convenient to seek for a correlation separately for results with $\mathrm{Re}_\gamma > 0$ (and $\Lambda_G > 0$), and for results where $\mathrm{Re}_\gamma = \Lambda_G = 0$. The latter case corresponds to a particle sedimenting in a quiescent fluid where no analytical results for two-dimensional flow seem to be available. For finite values of Re_γ relatively good data collapse is achieved by simply scaling the numerical data by the corresponding Bretherton's result. The ratio $C_q/|C_{q,\mathrm{B}}|$ depends primarily on Λ_G and κ, and only weakly on Re_γ. That residual dependence is well approximated by a simple power law $\propto \mathrm{Re}_\gamma^{\epsilon_q}$, where $\epsilon_\mathrm{D} \approx -0.15$ and $\epsilon_\mathrm{L} \approx 0.30$. For the results with $\mathrm{Re}_\gamma \neq 0$ the scaled force coefficients P_D and P_L are thus defined by

$$\frac{C_q}{|C_{q,\mathrm{B}}|} = P_q(\Lambda_G, \kappa)\mathrm{Re}_\gamma^{\epsilon_q}, \quad q = \mathrm{D}, \mathrm{L}. \tag{3.21}$$

According to the proposed scaling law given by Eq. (3.21), the scaled drag and lift coefficients P_D and P_L depend on only two variables instead of the three variables that appear in the original force coefficients, Eqs. (3.16). The calculated values of P_D and P_L for various values of Λ_G ($\neq 0$) and κ are shown in Fig. 3.3. It is evident from Fig. 3.3 that the calculated scaled coefficients P_D and P_L indeed collapse on a set of smooth curves as a function of the dimensionless shear rate Λ_G, each curve corresponding to a distinct value of the inverse distance κ. The factorization given in Eqs. (3.21) thus seems justified. For the results where κ is small and Λ_G is large, the data scatter is, however, quite large especially for P_D. In this region the cylinder is far away from the nearest wall, the slip velocity is small and the shear is strong. In this condition the calculated drag force is very small and the drag coefficient is computed as a ratio of two small numbers and may thus involve large absolute errors due to numerical fluctuations. The finite total width of the channel, that was ignored in the dimensional analysis above, may also affect the numerical results in this region.

For values of $\Lambda_G > 0.1$ the numerical results can be fitted using the following functional forms

$$\begin{aligned} P_\mathrm{D}(\Lambda_G, \kappa) \quad &= [a_{01}\kappa/(1-\kappa) + a_{02} + a_{03}\kappa] \\ &+[a_{11}\kappa/(1-\kappa) + a_{12}\kappa + a_{13}\kappa^2]\Lambda_G. \end{aligned} \tag{3.22}$$

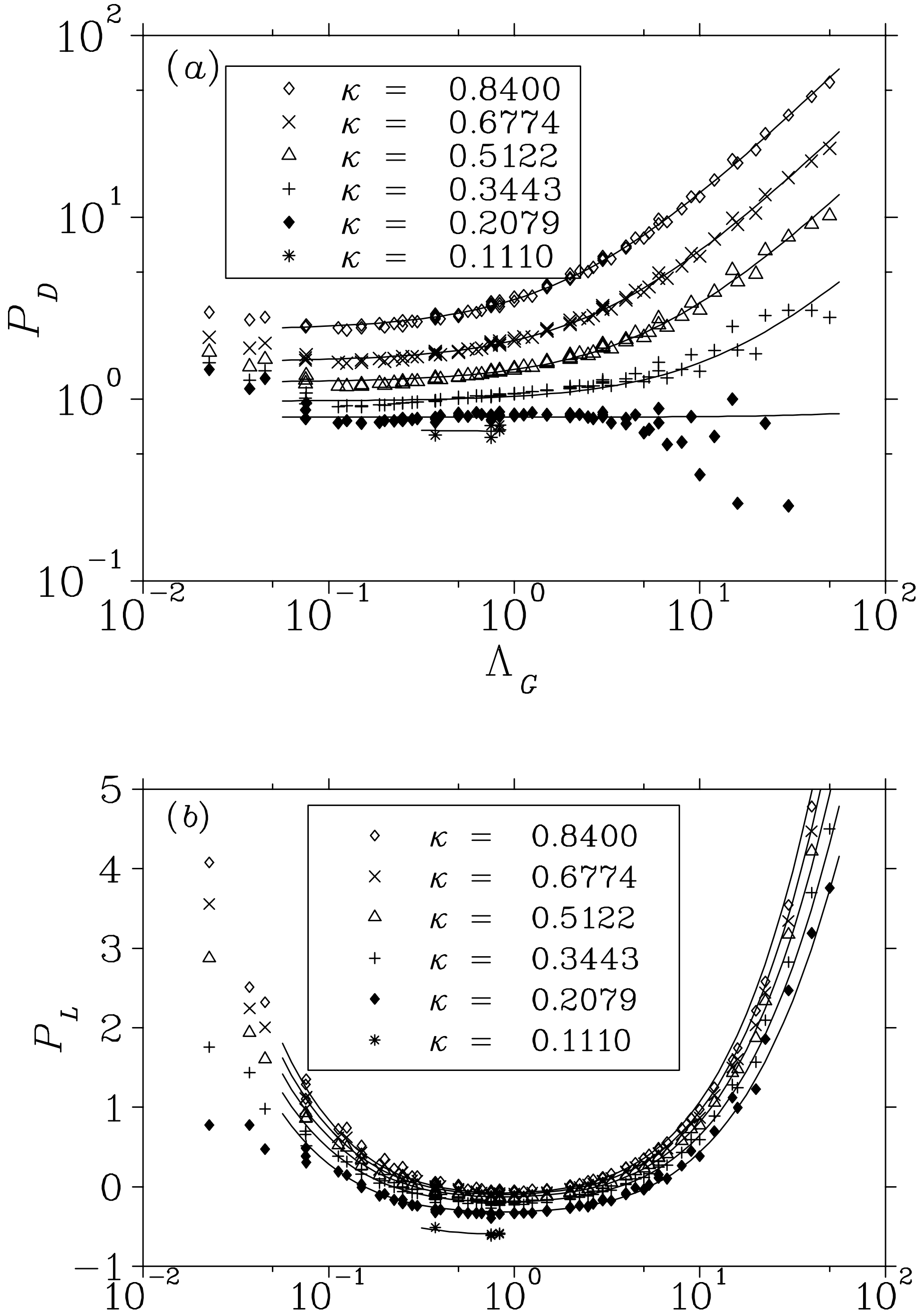

Figure 3.3: Scaled a) drag force P_{D} and b) lift force P_{L} vs dimensionless shear rate Λ_G for various values of inverse dimensionless distance κ. Discrete points are the numerical results and the solid lines are the corresponding fitted functions given by Eqs. (3.22) and (3.23).

$$P_{\mathrm{L}}(\Lambda_G, \kappa) = b_0 + \frac{b_1}{b_2 + \kappa} \tag{3.23}$$

$$-(1+\kappa)(1+\lg^2 \Lambda_G)[b_3 \lg \Lambda_G + b_4 \lg^2 \Lambda_G]. \tag{3.24}$$

The values of the unknown coefficients that appear in Eqs. (3.21), (3.22) and (3.23) were found by using a standard least-squares fitting method, and are given in Table 3.1. The fitted functions, also shown in Fig. 3.3, reproduce the numerical results quite accurately in both cases, except for small values of Λ_G where the Bretherton's result used in data scaling becomes inappropriate.

It is noticed that the functional forms of P_{D} and P_{L} given by Eqs. (3.22) and (3.23) have no physical justification other than giving a good fit to the numerical data in a quite broad range of parameter values. They do, however, exhibit the following natural limiting behaviour: for large distances ($\kappa \rightarrow 0$), the scaled drag force approaches a constant value $a_{02} \approx 0.55$ (see Eq. (3.22) and Table 3.1) for all values of the dimensionless shear rate. The fitted ratio $C_{\mathrm{D}}/|C_{\mathrm{D,B}}|$, as given by Eq. (3.21) is then close to unity for all values of Re_γ used in the present calculation (excluding the limit $\mathrm{Re}_\gamma \rightarrow 0$, which is discussed below). In this limit, the fitted functions thus reproduce Bretherton's analytical result for drag quite closely. The ratio $C_{\mathrm{L}}/|C_{\mathrm{L,B}}|$ is also of the order of unity in the region where Bretherton's result is assumed to be valid, namely when Re_γ and Re_{p} are both small and Λ_G is close to one. The deviation from the Bretherton's result of the present results is, however, larger for the lift than for the drag. A plausible reason for this is that the presence of walls has a stronger relative influence on lift force than on drag force. For all finite values of Re_γ the fitted values of the two forces, as given by Eq. (3.13), both vanish when $\mathrm{Re}_{\mathrm{p}} \rightarrow 0$ ($\Lambda_G \rightarrow \infty$). Furthermore, for finite values of Re_{p} the drag force diverges as $\kappa \rightarrow 1$, *i.e.*, as the width of the gap between the cylinder and the wall approaches zero. This reflects the divergence of the shear rate in the narrow gap as the cylinder is brought into contact with the wall. Irrespective of the value of κ, the lift force is repulsive when the shear rate Λ_G is low enough or high enough, but is attractive at a region around $\Lambda_G = 1$. Increasing κ increases lift force thus making it more repulsive.

Next, the results where $\mathrm{Re}_\gamma = \Lambda_G = 0$ are studied, *i.e.*, the case corresponding to a cylinder sedimenting near a wall in a quiescent fluid. The calculated values of the drag and lift coefficient for this case are shown in Figs. 3.4 a) and b), respectively. Also shown in Fig. 3.4 a) is the standard experimental drag coefficient for a long cylinder in an infinite fluid and in the absence of shear (notice, that the particle Reynold's number is defined here in terms of the radius of the particle).

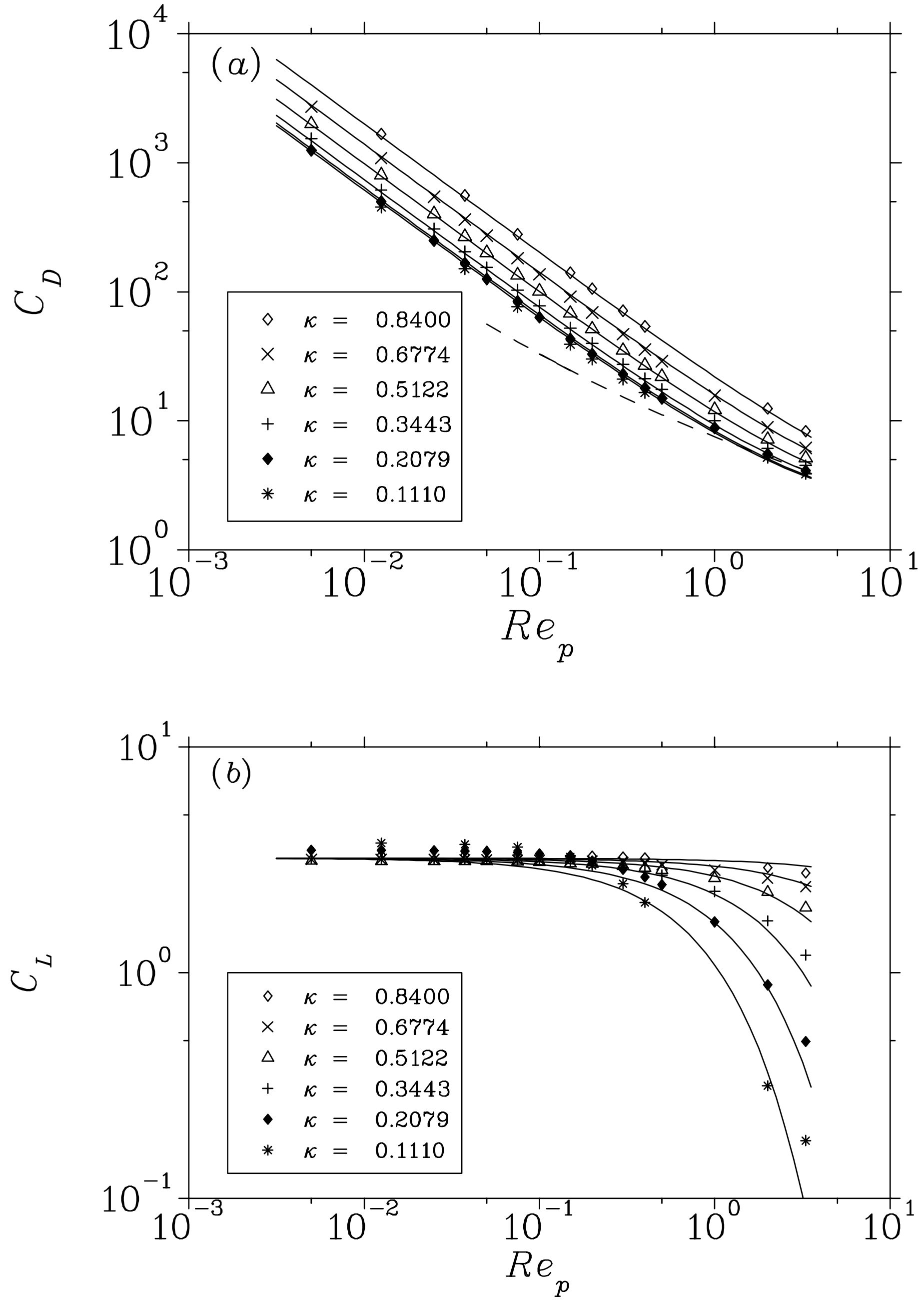

Figure 3.4: Drag force coefficient $C_{\rm D}$ (a) and lift force coefficient $C_{\rm L}$ (b) vs slip Reynolds number $\rm Re_p$ for vanishing shear rate, *i.e.* $\rm Re_\gamma = 0$. Discrete points are the numerical results and the solid lines are the fits given by (3.27) and (3.26). Dashed line gives the experimental values for the drag force with $\kappa = 0$ and $\rm Re_\gamma = 0$ (data reproduced from Fig. 7.16 a) of Ref. [Whi94]).

When the distance from the wall is small (κ is close to unity), the calculated value of the drag coefficient is roughly of an order of magnitude larger than the experimental drag coefficient, but approaches the experimental value as the distance from the wall increases. With the largest distances used in the calculation, the qualitative behaviour of the drag coefficient is similar to the experimental result. The maximum deviation between the computed value and the experimental value is then less than a factor of two. This deviation remains even in the case of vanishing shear and arises most probably due to the closed channel used in the calculation since the effect of walls decreases very slowly in this two-dimensional flow. (This phenomenon is related to Whitehead's paradox.)

The lift coefficient for a sedimenting cylinder is always positive indicating repulsive lift force. At high values of $\mathrm{Re_p}$ the lift coefficient depends strongly on the distance from the wall increasing with κ. At small values of $\mathrm{Re_p}$, C_L becomes nearly independent on the distance from the wall. This result, which may seem somewhat surprising is, in fact, in accordance with former analytical results for a sphere sedimenting near a flat wall [CM94].

The behaviour of the calculated drag and lift coefficients at $\mathrm{Re}_\gamma = 0$ can be quite accurately fitted using the following simple functions.

$$\begin{aligned} C_\mathrm{D}(\mathrm{Re_p}, \kappa) &= \frac{1}{\mathrm{Re_p}}\Big[A(\kappa) + B\,\mathrm{Re_p^{\mathit{n}}}\Big] && (3.25) \\ \log\, C_\mathrm{L}(\mathrm{Re_p}, \kappa) &= a_0\Big[1 - \mathrm{Re_p}(-\log\kappa)^m\Big], && (3.26) \end{aligned}$$

where

$$\begin{aligned} A(\kappa) &= 6.1 + 22.2\,\kappa^{2.7} \\ B &= 1.9 && (3.27) \\ n &= 1.0 \\ m &= 1.7 \\ a_0 &= 0.50\,. \end{aligned}$$

These functions are also shown in Figs. 3.4 a) and b). The limiting behaviour of the fitted drag coefficient as $\kappa \to 0$ is close to the experimental result for a cylinder in an infinite fluid. Notice that for values of $\mathrm{Re_p}$ between 0.05 and 100, the experimental result for the drag coefficient can be very accurately fitted with an equation of the form (3.25) with constant values

Table 3.1: Fitted coefficients of drag and lift forces (see Eqs. (3.22) and (3.23))

$a_{11} = 0.140$	$a_{12} = -0.38$	$a_{13} = 1.01$
$b_0 = -0.0050$	$b_1 = 0.067$	$b_2 = -0.001$
$b_3 = -0.031$	$b_4 = -0.279$	

$A \approx 3.0$, $B \approx 3.0$ and $n \approx 0.8$. For small values of $\mathrm{Re_p}$ the fitted lift coefficient approaches a constant value of approximately 3.5. This is to be compared with the corresponding value achieved by Cherukat and McLaughlin for a sphere in a three-dimensional flow, namely $C_\mathrm{L} \sim 1.1$ (defined in a usual manner using the cross-sectional area of the sphere) [CM94].

The primary variables that characterize drag and lift forces on the particle are the slip velocity, the shear rate and the distance from the wall (made dimensionless in a usual manner using the radius of the particle and the kinematic viscosity of the fluid). Both forces vanish with vanishing slip velocity and are strongly modified by the vicinity of the wall. As the distance from the moving wall approaches zero, the drag force diverges while the lift force approaches a constant positive (repulsive) value. The drag force depends only weakly on shear while the lift force is very sensitive to the shear rate. Depending on the flow parameters, the lift force may be either repulsion from the wall, or attraction towards the wall. That feature is of particular interest concerning the dynamics of the particle-free wall layer in the channel flow of liquid-particle suspensions.

3.4 Simulations: a matrix of stationary cylinders

In order to gain qualitative understanding on the flow of fibre plug near a wall a random rigid array of cylinders suspended in a flow of a Newtonian fluid between two walls is considered. The system consists of two parts, namely a suspension layer of width w and a fluid layer of width λ (see Fig. 3.5). The upper wall adjacent to the pure fluid layer moves with velocity v_w in the direction of z-axis, and the lower wall adjacent to the suspension is stationary. The set-up thus resembles the flow of a fibre plug in a direction of negative z-axis viewed in the rest frame of the plug and considering only the boundary layer near the wall.

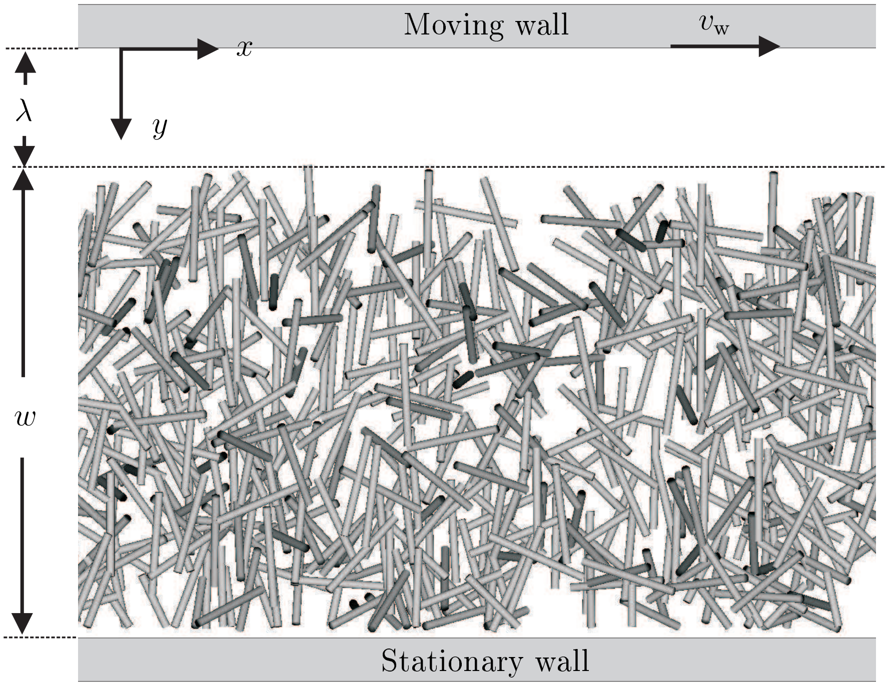

Figure 3.5: Random rigid particle matrix made of cylinders suspended in a shear flow of a Newtonian fluid.

Two approaches are used: Analytic solution in terms of averaged flow quantities and direct numerical simulations with the lattice-Boltzmann method. In the lattice-Boltzmann method, viscous flow of a fluid is modeled by solving a special version of the Boltzmann equation that has been discretized in space, time and momentum [RSM92, QdL92]. In the continuum limit the governing continuity and Navier-Stokes equations are recovered from this discretized equation. In practice, motion of fictitious fluid particles is simulated, and special particle-particle collision models are applied in a way that automatically generates viscous flow behaviour. The lattice-Boltzmann method appears to be particularly useful for complex fluids and for solving flow in complex and irregular geometries such as the present one [Lad94, FR95].

The simulations were carried out separately in a two-dimensional case where the cylinders are parallel and the flow is perpendicular to the cylinders, and in a three-dimensional case with random orientation of the cylinders.

3.4.1 Analytic solution of the averaged flow velocity

The detailed microscopic flow field in a random system shown in Fig. 3.5 is complicated. It would be quite difficult to analytically solve forces acting on individual particles. Instead, a multiphase flow approach in terms of averaged quantities, *e.g.* the average drag force acting on the cylinders at a given distance from the moving wall, will be considered. The analytic results will then be compared with the numerical results achieved by first solving the microscopic flow for an ensemble of macroscopically identical systems using the lattice-Boltzmann method, and then computing the appropriate averaged quantities.

Now the average fluid velocity is derived by considering the suspension as a system of two interacting continua, namely the fluid phase and the solid phase. The governing equation for the average fluid velocity is derived by applying volume averaging to the microscopic equations for the fluid flow through the particle matrix. To that end, the equations for a flow of liquid in a porous medium that were derived in Sect. 2.3.2 are applied to the current case. The conservation of mass is described by Eqs. (2.59) and (2.60), and the conservation of momentum of the solid phase is given by Eq. (2.62). Here the fluid flow is a shear flow driven by the moving wall, thereby one has to retain the viscous shear stress of the fluid phase, Eq. (2.68), in the formulation and use Eq. (2.70) for the conservation of momentum of the fluid phase. In the present case gravity is neglected.

Here a stationary flow is assumed, hence all the partial derivatives with respect to time vanish. Furthermore, a fully developed flow is considered, *i.e.* the averaged quantities of the suspension do not depend on the position in the x-direction (notice that this applies also to the hydrodynamic pressure, since the flow is *not* driven by a pressure gradient). Thus the average fluid velocity is parallel to the walls everywhere, *i.e.* $\bar{\mathbf{u}}_{\mathrm{f}} = u_{\mathrm{f}}(y)\hat{\mathbf{e}}_x$.

The solid matrix is stationary, $\bar{\mathbf{u}}_\mathrm{s} = 0$. Thus, the averaged equation for the conservation of mass of the solid phase, Eq. (2.60), is satisfied trivially. Notice that the equation for the conservation of momentum of the solid phase, Eq. (2.70), is not needed for the solution. This equation can be used to calculate the mechanical stress $\langle \sigma_\mathrm{s} \rangle$ of the solid phase after the solution for the fluid flow field has been found.

With the assumptions discussed above, the equation for the conservation of the longitudinal momentum of the fluid phase can be written in the form

$$\phi \mu_\mathrm{f} \frac{\mathrm{d}^2 u_\mathrm{f}}{\mathrm{d}y^2} + \mu_\mathrm{f} \frac{\mathrm{d}\phi}{\mathrm{d}y} \frac{\mathrm{d}u_\mathrm{f}}{\mathrm{d}y} - D_\mathrm{s} = 0, \tag{3.28}$$

where μ_f is the dynamic viscosity of the fluid, y is the distance to the moving wall, ϕ is the porosity of the suspension, and $D_\mathrm{s} = W_{s,x}$ is the volumetric density of the hydrodynamic drag force acting on the solid matrix. Inside the fluid layer this force vanishes, and inside the suspension layer it is given according to Darcy's law:

$$D_\mathrm{s} = \begin{cases} 0, & 0 \leq y < \lambda \\ \frac{\mu_\mathrm{f}}{k} u_\mathrm{f}, & 0 \leq y \geq \lambda \end{cases} \tag{3.29}$$

where k is the permeability of the solid matrix.

The average drag force per unit length of a cylinder, F_D, can be calculated by multiplying the force density D_s by the average cross-sectional area occupied by a single cylinder, and the results is

$$F_\mathrm{D} = \frac{\pi \mu_\mathrm{f} a^2}{(1-\phi)k} u_\mathrm{f}, \tag{3.30}$$

where a is the radius of the cylinder, and u_f is the average fluid velocity at the same transverse position as the cylinder.

Let us assume that the porosity is constant $\phi = \phi_0$ inside the suspension layer ($y \geq \lambda$). Equation (3.28) then reduces to the form

$$\frac{\mathrm{d}^2 u_\mathrm{f}}{\mathrm{d}y^2} = 0, \quad 0 \leq y < \lambda \tag{3.31}$$

$$\frac{\mathrm{d}^2 u_\mathrm{f}}{\mathrm{d}y^2} - \frac{1}{\phi_0 k} u_\mathrm{f} = 0, \quad \lambda \leq y \leq \lambda + w. \tag{3.32}$$

The no-slip boundary condition is applied at both walls, *i.e.* $u_\mathrm{f}(0) = v_w$ and $u_\mathrm{f}(\lambda + w) = 0$.

The porosity has a discontinuous jump at the boundary $y = \lambda$, and the general solutions to Eqs. (3.31) and (3.32) have to be matched at the boundary so that the fluid velocity and the total shear stress are continuous. Notice that inside the suspension layer both phases contribute to the total shear stress, and details of this process depend on the microscopic flow field. It is expected, however, that the solid shear stress is relatively small due to low solid concentration. Thus an approximation is made by imposing the continuity of the fluid shear stress at the boundary $y = \lambda$:

$$\lim_{y \to \lambda_-} \langle \tau_{\mathrm{f}} \rangle = \lim_{y \to \lambda_+} \langle \tau_{\mathrm{f}} \rangle, \tag{3.33}$$

where the fluid shear stress tensor $\langle \tau_{\mathrm{f}} \rangle$ is given by Eq. (2.68). In the current case this condition simplifies to the form

$$\left(\frac{\mathrm{d}u_{\mathrm{f}}}{\mathrm{d}y} \right)_- = \left(\frac{\mathrm{d}u_{\mathrm{f}}}{\mathrm{d}y} \right)_+ , \tag{3.34}$$

where $(\mathrm{d}/\mathrm{d}y)_-$ and $(\mathrm{d}/\mathrm{d}y)_-$ denote the one-sided derivatives from positive and negative side, respectively. Equations (3.31) and (3.32) are solved with the boundary conditions and the matching conditions discussed above, and the solution for the fluid velocity (in the x-direction) is found as

$$\begin{aligned} u_{\mathrm{f}}(y) &= -\frac{y}{\lambda} v_w + \left(1 + \frac{y}{\lambda} \right) u_0, \quad 0 \le y < \lambda \\ u_{\mathrm{f}}(y) &= \frac{\exp(\alpha(y-\lambda)) - \exp(\alpha\{2w - (y-\lambda)\})}{1 - \exp(2w\alpha)} u_0, \quad \lambda \le y \le \lambda + w, \end{aligned} \tag{3.35}$$

where $\alpha = (\phi_0 k)^{-1/2}$, and the velocity at the plug surface is given by

$$u_0 \equiv u_{\mathrm{f}}|_{y=\lambda} = v_w \left(1 - \phi_0 \alpha \lambda \frac{1 + \exp(2\alpha w)}{1 - \exp(2\alpha w)} \right)^{-1} \tag{3.36}$$

This result will be compared with the numerical results in the next two sections.

3.4.2 Lattice-Boltzmann solution: unidirectional cylinders

The hydrodynamic interactions in a flow perpendicular to a rigid matrix of parallel cylinders were studied by solving the fluid flow between the suspended particles in a number of systems similar to that shown in Fig. 3.6 using the lattice-Boltzmann (LB) method [QdL92, RSM92,

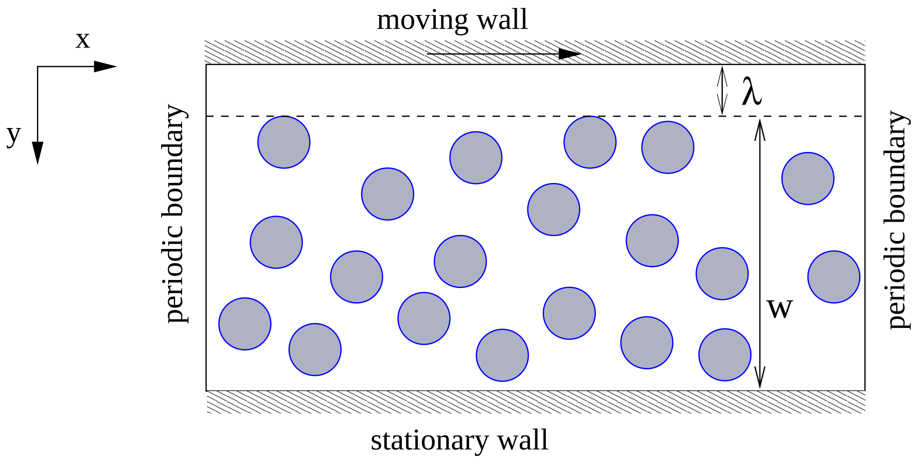

Figure 3.6: Random rigid particle matrix made of parallel cylinders suspended in a shear flow of a Newtonian fluid between parallel walls.

Sko93]. For each macroscopic configuration, *i.e.* wall velocity v_w, bulk porosity ϕ_0 and fluid gap width λ fixed, an ensemble of $80-100$ random systems was used. The simulations were done here using a particular version of the method, namely the 9-link lattice-Bhatnagar-Gross-Krook (LBGK) model [Sko93].

The simulations were done using cylinders of radius $a = 11.5$ (in lattice units). Notice however that due to the discreteness of the model the hydrodynamic radius a_h of the obstacles differs slightly from that value of a. The proper value of a_h was defined by solving the fluid flow through an infinite (periodic) array of cylinders arranged in a square lattice. The simulated permeability at the porosity $\phi = 0.95$ was found to be $k = 540$ (in lattice units). The analytical solution of the permeability is known and can be given in terms of the actual radius of the cylinders [JJ86]:

$$\frac{k}{a_h^2} = \frac{1}{8\phi_\mathrm{s}}\left(-\ln(\phi_\mathrm{s}) - 1.476 + 2\phi_\mathrm{s} - 1.774\phi_\mathrm{s}^2 + O(\phi_\mathrm{s}^3)\right), \tag{3.37}$$

where $\phi_\mathrm{s} \equiv 1-\phi$ is the volume fraction of the solid phase. Substituting the simulated values $\phi = 0.95$ and $k = 540$ in Eq. (3.37), and solving for the hydrodynamic radius leads to a value $a_h = 11.56$. This indicates that the discretization used here was dense enough and the obstacles appear nearly as smooth cylinders.

Since the grid used by the present method is regular, the discretization of the gap between the particle and the wall will be rough when particles are placed very close to the wall. The

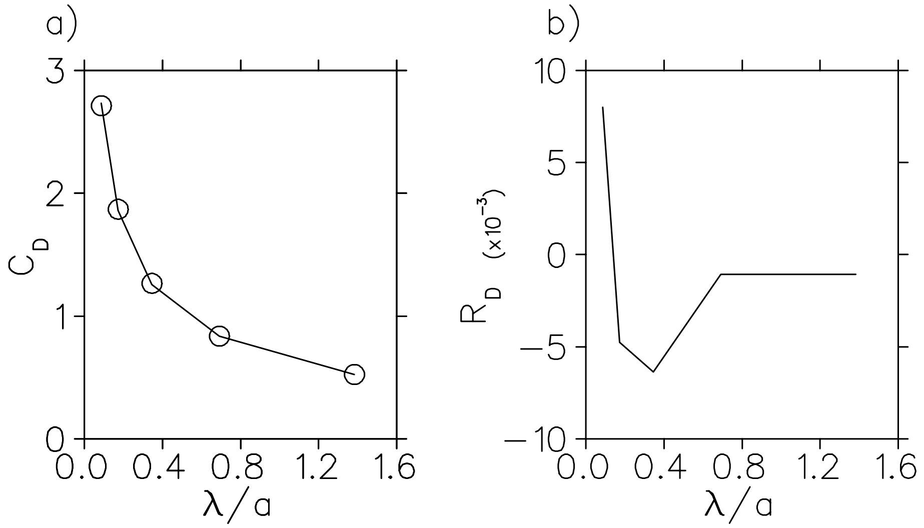

Figure 3.7: a) The drag force coefficient C_{D} for a cylinder near a moving wall as a function of of dimensionless gap length λ/a as given by the FV -simulation (solid line) and the LB -simulation (open markers). b) The relative difference R_{D} between the drag forces given by the two methods as a function of dimensionless gap length λ/a.

accuracy of our LB simulations were checked in this respect by computing the lift and drag forces acting on a single particle that was placed close to a moving wall, and compared the results with those given by a standard finite volume methods with greatly densified grid in the gap region. The size of the calculation area was $L_y \times L_x = 98 \times 140$ lattice spacings. Periodic boundary conditions were applied in the x-direction. The upper wall was made to move with velocity $V_w = 0.05$ (expressed in lattice units) using the method presented in Ref. [Lad94]. The gap between the particle and the moving wall was 1, 2, 4, 8 and 16 lattice spacings. The lower wall was stationary.

The drag force coefficients C_{D} given by the FV -method and the LB -method are shown in Fig. 3.7 a) as a function of the dimensionless gap distance λ/a. As shown by Fig. 3.7 a), the calculated drag force increases rapidly with decreasing gap width. The relative difference $R_{\mathrm{D}} = (F_{\mathrm{D,FV}} - F_{\mathrm{D,LB}})/F_{\mathrm{D,FV}}$, where $F_{\mathrm{D,FV}}$ and $F_{\mathrm{D,LB}}$ are the drag forces given by FV and LB methods, respectively, is given in Fig. 3.7 b). The difference between the two results is very small everywhere. Remarkably, R_{D} is less than 1% even in the case where the gap width is only one lattice spacing.

The lift force coefficients C_{L} given by the two methods are shown in Fig. 3.8 a.) The lift force is seen to be repulsive (positive) at all distances in this case and it increases rapidly

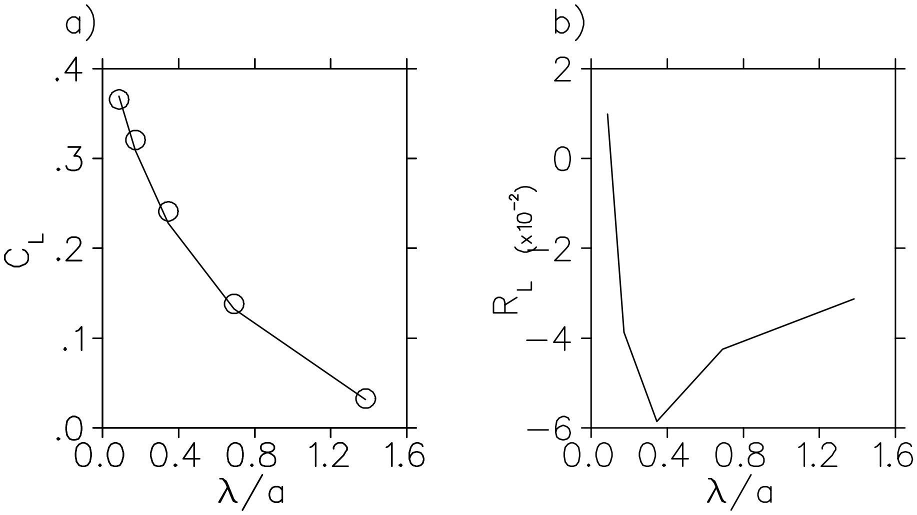

Figure 3.8: a) The lift force coefficient C_{L} for a cylinder near a moving wall as a function of dimensionless gap length λ/a given by the FV simulations (solid line) and LB simulations (open markers). Positive values indicate repulsive force. b) The relative difference R_{L} between the lift forces given by the FV and LB method as a function of dimensionless gap length λ/a.

with decreasing gap width. As can be seen in Fig. 3.8 b), the relative deviation of the two methods is now higher than in the case of the drag force. However, even in the worst case it remains below 6%. The absolute value of the deviation is of the same order of magnitude in both cases. Based on these results it is concluded that the results given by the lattice-Boltzmann approach for the drag and lift forces acting on particles moving close to a wall are in accordance with the results given by the conventional finite volume method used here.

The actual simulations of hydrodynamic forces acting on the random rigid array of suspended particles were done in lattices of 300–330 × 780 lattice spacings depending on the gap width λ (see Fig. (3.6)). Two arbitrary values for the porosity were chosen to study the effect on the hydrodynamic forces of the porosity. The simulations were done at bulk porosities $\phi_0 = 0.88$ and $\phi_0 = 0.94$ (corresponding to systems of 60 and 30 particles, respectively). With $\phi_0 = 0.94$ two different wall velocities v_w were used, namely $v_w = 0.025$ and $v_w = 0.05$ (in lattice units). Periodic boundary conditions were applied in the x-direction. The system was let to saturate for 20000 time steps. This resulted in the maximum relative error of approximately 1% for both the lift and the drag forces.

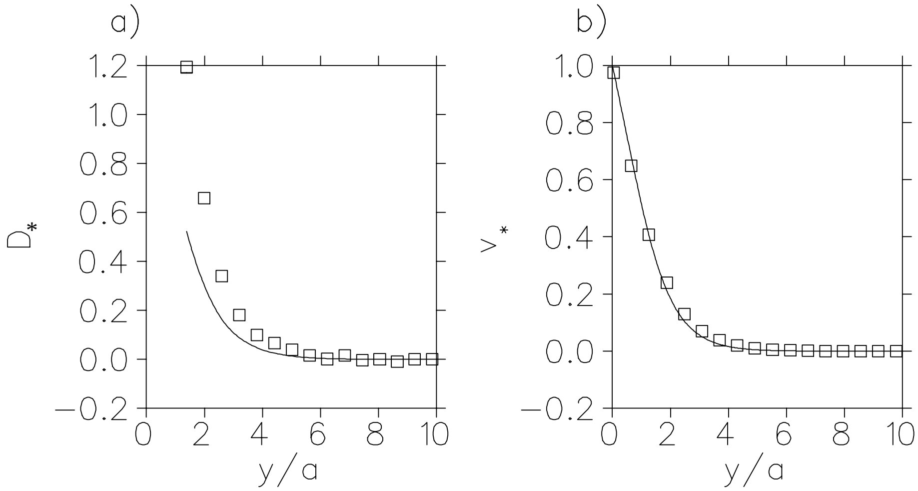

Figure 3.9: a) The dimensionless drag force D_* acting on a cylinder near a moving wall vs. dimensionless distance y/a for porosity $\phi_0 = 0.88$ and gap width $\lambda = 4$. The numerical and analytical results (see Eq. (3.30)) are given by open symbols and solid line, respectively. b) The dimensionless velocity v_* vs. dimensionless distance y/a. The porosity is $\phi_0 = 0.90$ and the gap width is $\lambda = 4$. The numerical and analytical results (see Eq. (3.35)) are given by open symbols and solid line, respectively.

Next the dimensionless averaged drag force acting on a cylinder defined by

$$D_* = \frac{F_{\mathrm{D}}}{4\pi\mu_{\mathrm{f}}v_{\mathrm{w}}} \tag{3.38}$$

is considered. Combining this equation with Eq. (3.30) one gets the dimensionless drag force as given by Darcy's law

$$D_* = \frac{v_*}{4(1-\phi)K}, \tag{3.39}$$

where $v_* = u_{\mathrm{f}}/v_{\mathrm{w}}$ is the dimensionless flow velocity and $K = k/a^2$ is the dimensionless permeability. The dimensionless drag force D_* as a function of the dimensionless distance y/a from the moving wall is shown in Figs. 3.9 a) and 3.10 a) for porosities $\phi_0 = 0.88$ and $\phi_0 = 0.94$, respectively. The gap width is $\lambda = 4$ in both cases shown. The dimensionless velocity v_* as a function of the dimensionless distance is shown in Figs. 3.9 b) and 3.10 b). The dimensionless permeabilities for the given porous media are calculated using the correlation derived by Kuwabara, Eq. (2.55), and they are $K = 1.57$ and $K = 3.38$ for porosities $\phi = 0.88$ and $\phi = 0.94$, respectively.

The deviation of the results given by Darcy's law from the numerical results is quite large

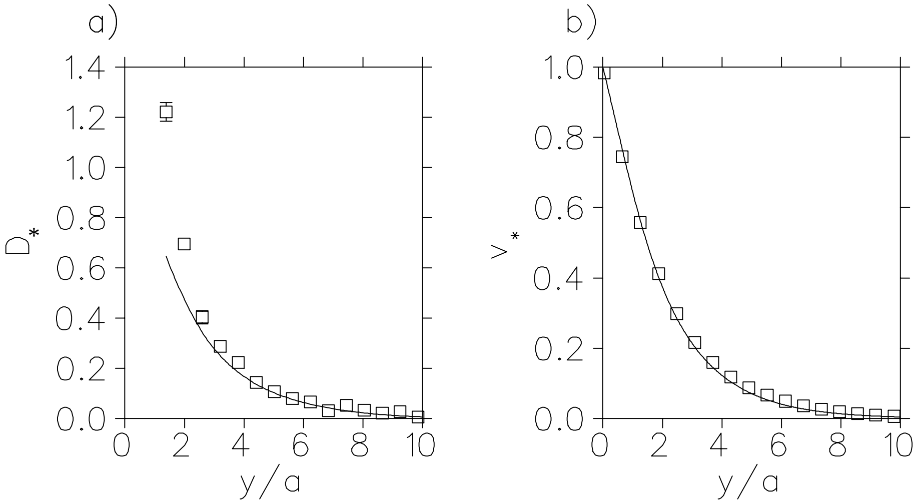

Figure 3.10: Same as Fig. 3.9 but for higher porosity $\phi_0 = 0.94$

especially for the lower value of porosity. For the outermost particles the relative difference between the two results is approximately 50% for both porosities. The reason for this deviation can be found by considering the single particle results shown in Fig. 3.2 a). Keeping the local flow conditions (Reynolds numbers) unchanged and decreasing the distance between the particle and the wall (increasing κ) increases the drag force. Below, it will be found out that the same is true also for the average drag force acting on an array of particles. This increase of drag force should thus reflect itself as a deviation from the usual Darcy's law near the walls.

The calculated average lift force F_L per particle as a function of the dimensionless distance y/a from the moving wall for a fixed gap width $\lambda/a = 0.35$, is shown in Figs. 3.11 a) and b) for the bulk porosities $\phi_0 = 0.94$ and $\phi_0 = 0.88$, respectively. The wall velocity is $v_\mathrm{w} = 0.05$ in the both cases shown.

The lift force F_L appears to be strongly repulsive close to the wall, but changes into weak attraction at $y/a \approx 2 - 3$. Still further away from the wall the lift force decays rapidly as the fluid velocity approaches zero. In this region the lift force may even oscillate between attraction and repulsion. The attractive region becomes narrower and moves closer to the wall as the porosity is lowered, which correlates with the steepening of the velocity profile with decreasing porosity (see Figs. 3.9 b)) and 3.10 b)). The absolute statistical errors in the simulated drag and lift force are of the same magnitude, but since the values of the lift force are an order of magnitude smaller than the values of the drag force, the relative errors are

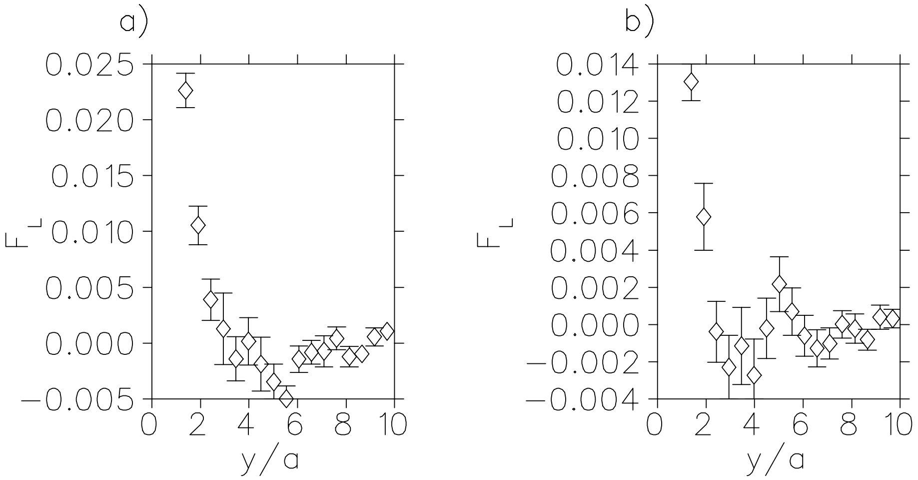

Figure 3.11: The numerical results for lift force F_L (in lattice units) vs. dimensionless distance y/a for fluid gap width $\lambda = 4$ and wall velocity $v_\mathrm{w} = 0.05$, for porosity $\phi_0 = 0.94$ (a) and $\phi_0 = 0.88$ (b).

much higher for the lift force.

Further calculations with increasing gap width show that the behaviour of the lift force F_L remains similar to that shown in Fig. 3.11 b) irrespective of the gap width, except that the repulsive peak is truncated as the gap width increases. This phenomenon also explains the decrease of the integrated lift force with increasing gap width and the negative values achieved at relatively wide gap widths.

In what follows, the total drag and lift forces acting on the particle matrix are studied. The total drag force acting on the cylinders, as given by Darcy's law, can be calculated by integrating Eq. (3.29) over the system,

$$\Sigma F_\mathrm{D} = L_x \int_0^{\lambda+w} D \, \mathrm{d}y = \frac{L_x \mu_\mathrm{f}}{k} \int_\lambda^{\lambda+w} u_\mathrm{f} \, \mathrm{d}y, \tag{3.40}$$

where L_x is the size of the system in the x-direction. The total drag and lift forces are given in Fig. 3.12 a) and b) as a functions of the dimensionless fluid gap width λ/a. As shown in Fig. 3.12 a), the drag force is highest when the gap width is small (Fig. 3.12 a), and it decreases monotonically with increasing gap width. This behaviour is due to the decreasing average velocity difference between the particles and the fluid as the gap width is increased. The corresponding results obtained using Darcy's law deviate from the numerical results especially at small gap widths. As expected, the deviation decreases with increasing gap

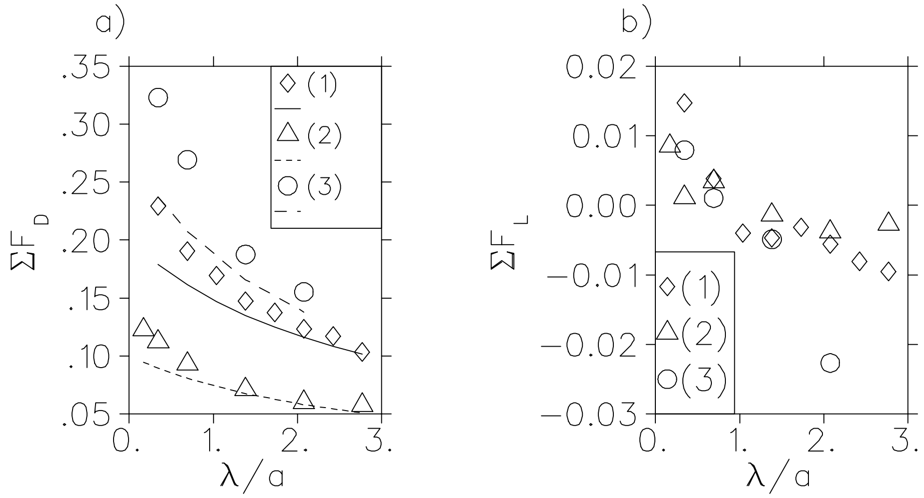

Figure 3.12: a) Total drag force ΣF_{D} and b) total lift force ΣF_{L} acting on the particle matrix as a function of the dimensionless fluid gap width λ/a. The forces are shown in lattice units. Open markers are the simulation results and the lines are given by Eq. (3.40). Set (1) is for $\phi_0 = 0.94, v_{\mathrm{w}} = 0.05$, set (2) is for $\phi_0 = 0.94, v_{\mathrm{w}} = 0.025$, and set (3) is for $\phi_0 = 0.88, v_{\mathrm{w}} = 0.05$.

width as the effect of the walls gradually decays.

According to the results shown in Fig. 3.12 b), the total lift force is repulsive (positive) when the gap width λ is much smaller than the particle radius a and becomes attractive as λ increases. Consequently, the total lift force is close to zero when λ is of the order of the particle radius a. An analogous condition might be prevalent in the plug flow regime of dense fibre suspension in the presence of a drag reducing lubrication layer. Notice, however, that in the fibre suspension there are many different length scales that affect hydrodynamic forces. The relevant size scale corresponding to the radius a used in these simulations may be, *e.g.*, the average floc size or the surface roughness of the fibre plug rather than the fibre radius.

For the porosities used in this study, the ratio of the Reynolds numbers Λ_G is always near unity, and the corresponding single-particle lift force is attractive (see Fig. 3.2 b)) even close to the wall, where the lift force on the array is strongly repulsive. This is true irrespective of whether the shear rate used in applying the single-particle result is calculated as the local shear rate of the computed velocity field inside the particle array or as the global shear rate of the linear velocity profile between the wall velocity and the slip velocity. Thus the simulated averaged lift force on the particle array can not be reproduced by using the single-particle result. This is most likely due to complex many-particle interactions that affect the local flow field and the hydrodynamic stress on particle surfaces.

3.4.3 Lattice-Boltzmann solution: random orientation of cylinders

The study is extended towards more realistic systems by considering the hydrodynamic interactions in a flow perpendicular to a rigid matrix of randomly oriented cylinders. The fluid flow between the cylinders in a number of systems similar to that shown in Fig. 3.5 is solved using the lattice-Boltzmann method. The simulations were carried out using the 19-link lattice-Bhatnagar-Gross-Krook model [RSM92].

The simulations were carried out at the bulk porosity $\phi_0 = 0.95$ and with the wall velocity $v_w = 0.0821$ (lattice units). Notice that the bulk porosities used in Chap. 3.4.2 were 0.88 and 0.94. The small change in porosity from a value 0.94 to a value 0.95 is due to a difference in the generation of simulation geometry that was discovered only afterwards. Three different gap widths were used, namely $\lambda = 1$, $\lambda = 4$, and $\lambda = 8$ (lattice units). For each fluid gap width an ensemble of $13 - 18$ random systems was simulated. Periodic boundary conditions were applied in the x and z-directions. The simulated flow field was saturated at least 15000 time steps.

The simulations were done in lattices of $800 \times (102–109) \times 780$ lattice spacings depending on the gap with. The cylinders used in the simulations had the radius of 3.5 and the length of 70 lattice spacings. They were placed in random positions with random orientations by allowing overlapping with each other. The random positions for the centres of fibres were chosen inside the suspensions layer $y > \lambda$, and the fibre segments that fell out of the suspension layer were cropped.

The averaged volumetric drag force density $D_{s,x}$ acting on the cylinder matrix is shown in Figs. 3.13– 3.15 a) as a function of the dimensionless distance y/a from the moving wall. The simulation results are shown as open markers, while the curves are given by Eq. (3.29). The dimensionless flow velocity $v_* = v/v_w$ is shown in Figs. 3.13– 3.15 b) as a function of the dimensionless distance from the moving wall. The simulation results are shown as open markers, while the curves are given by Eq. (3.28). The permeability correlations used here were Eq. (2.55), Eq. (2.56), and Eq. (2.58) for curves (1), (2), and (3), respectively.

It is immediately evident from the velocity graphs, that the permeability correlation Eq.

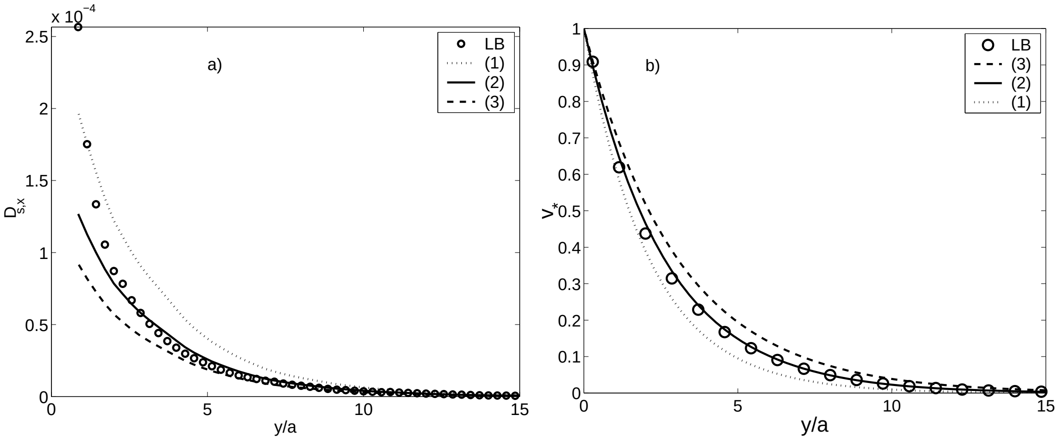

Figure 3.13: Results for a) the averaged drag force density acting on the solid matrix, $D_{s,x}$, and b) the dimensionless velocity v_* (right) vs. the dimensionless distance y/a for the fluid gap with $\lambda = 1$. Open symbols are the numerical results, and curves are given by Eq. (3.29) for the drag force and by Eq. (3.28) for the velocity. Permeability correlations used here are Eq. (2.55) for curves (1), Eq. (2.56) for curves (2), and Eq. (2.58) for curves (3). The forces are shown in lattice units.

(2.56) reproduces the simulated velocity profile with high accuracy. Equation (2.55) underestimates the permeability (overestimates flow resistance) thereby predicting too steep velocity profile, while Eq. (2.58) does the opposite. The same deviations can be seen in the graphs for the local drag force, as well. For the best permeability correlation used in this study, Eq. (2.56), the relative difference between the simulated and analytical drag force densities at the surface of the cylinder matrix, $y = \lambda$ is approximately 50%, 40%, and 20% for the gap widths $\lambda = 1$, 4, and 8, respectively. The reason for this deviation is most likely the same wall effect that was discussed in the case of unidirectional cylinders already.

In order to gain some qualitative understanding of this behaviour of local lift force, the average volumetric lift force density acting on the solid matrix was calculated from the simulation results. The lift force may be calculated explicitly from the particle distributions of the LB method during simulations or inferred afterwards from the simulated flow field. To that end two quantities are considered, namely the momentum transfer integral $\mathbf{M}_\mathrm{s}$ defined by Eq. (2.41,) and the lift force density $\mathbf{L}_\mathrm{s} = -\mathbf{L}$ where L is defined by Eqs. (2.45) and (2.69). Combining Eqs. (2.45), (2.69) and (2.70), one gets the following expressions for lift

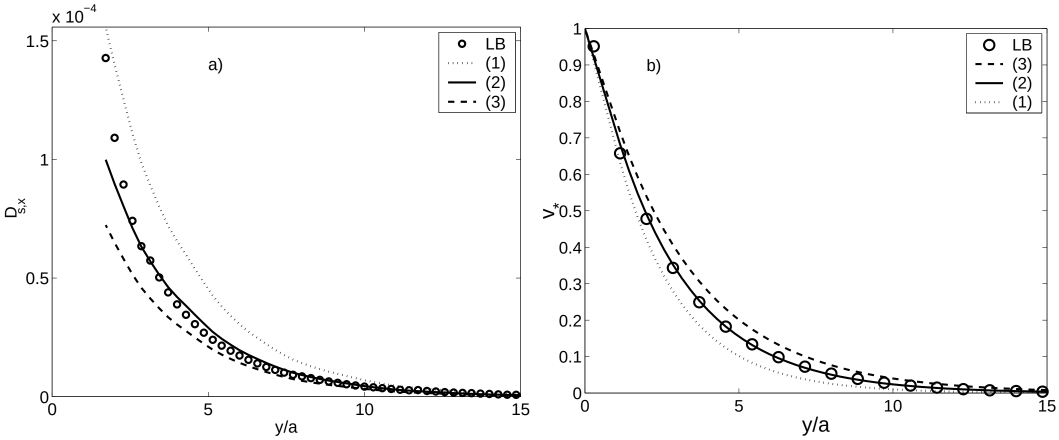

Figure 3.14: Same as Fig. 3.13 but for gap width $\lambda = 4$.

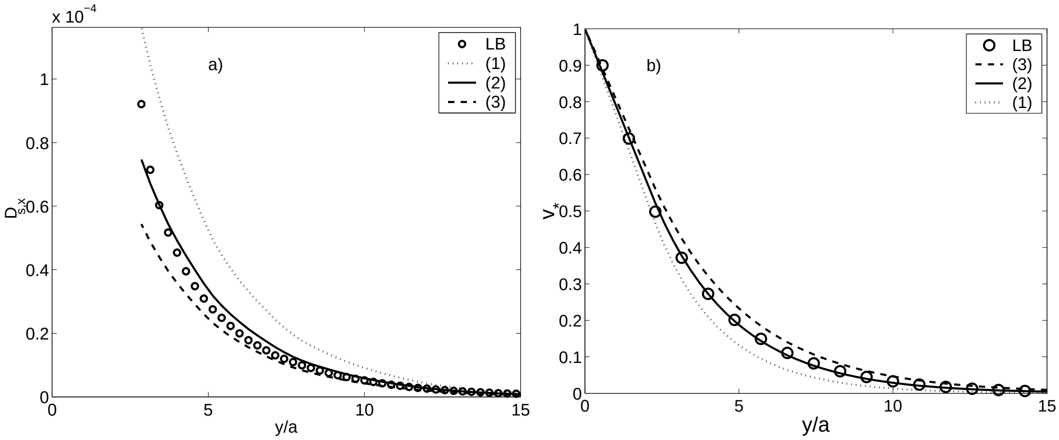

Figure 3.15: Same as Fig. 3.13 but for gap width $\lambda = 8$.

force density acting on the solid matrix

$$L_{\mathrm{s}} = -\phi \tfrac{\mathrm{d}\tilde{p}_{\mathrm{f}}}{\mathrm{d}y} + \tfrac{\mathrm{d}\tau_{\delta yy}}{\mathrm{d}y} \tag{3.41}$$

$$M_{\mathrm{s},y} = -\tilde{p}_{\mathrm{f}} \tfrac{\mathrm{d}\phi}{\mathrm{d}y} + L_{\mathrm{s}} = -\tfrac{\mathrm{d}}{\mathrm{d}y}(\phi \tilde{p}_{\mathrm{f}}) + \tfrac{\mathrm{d}\tau_{\delta yy}}{\mathrm{d}y}, \tag{3.42}$$

where the pseudoturbulent stress is defined in terms of velocity fluctuations as

$$\tau_{\delta yy} = -\langle \rho_{\mathrm{f}} \left(\delta u_{\mathrm{f},y}\right)^2 \rangle. \tag{3.43}$$

Notice that the lift force density L_{s} arises solely due to inertial effects in the fluid flow, while

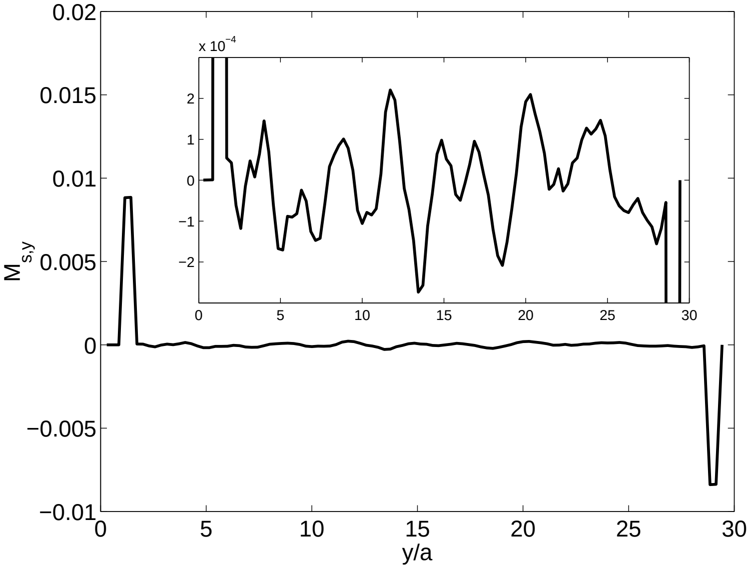

Figure 3.16: The average volumetric lift force density $M_{\mathrm{s},y}$ vs. dimensionless distance y/a for gap width $\lambda = 4$. In the insert the vertical axis is magnified to reveal the fluctuations. The force density is given in lattice units.

$M_{\mathrm{s},y}$ includes the effect of hydrostatic buoyancy as well (see Eq. (2.45)). The calculated averaged lift force density $M_{s,y}$ is shown as a function of the dimensionless distance y/a from the moving wall in Fig. 3.16 for gap with $\lambda = 4$. There is a strong positive (negative) lift force density at the surface of the cylinder matrix near the moving (stationary) wall that repels the cylinders away from the wall. Between these two peaks, the average volumetric lift force density fluctuates with zero mean value. One cannot find the same kind of behaviour of the lift force as in the case of unidirectional cylinders. Besides, it may appear odd at the first sight that there is a strong lift force at the matrix surface next to the stationary wall. The explanation for this behaviour can be found by looking Eq. (3.42), where the interesting term is the one containing the derivative of the local porosity, *i.e.*the buoyancy term. This pressure driven term contributes to the total hydrodynamic force in the regions of local porosity changes even in a case of constant average pressure. The local average porosity and its derivative were calculated, and the results were plotted as a function of the dimensionless distance from the moving wall y/a for gap width $\lambda = 4$. The results are shown in Fig. 3.17. Comparing the graphs in Figs. 3.16 and 3.17, one may immediately conclude that the dominant part of the lift force shown in Fig. 3.16 is due to step in the porosity at the surfaces of the cylinder matrix, and the porosity fluctuations inside the matrix. The fluctuations in the porosity are due to limited number of systems used in ensemble averaging, and could be made arbitrary small by increasing the number of simulated systems. The steps in porosity at the surfaces of the solid matrix, and the corresponding peaks at the lift force, will, however, stay intact irrespective of the size of the ensemble used in averaging.

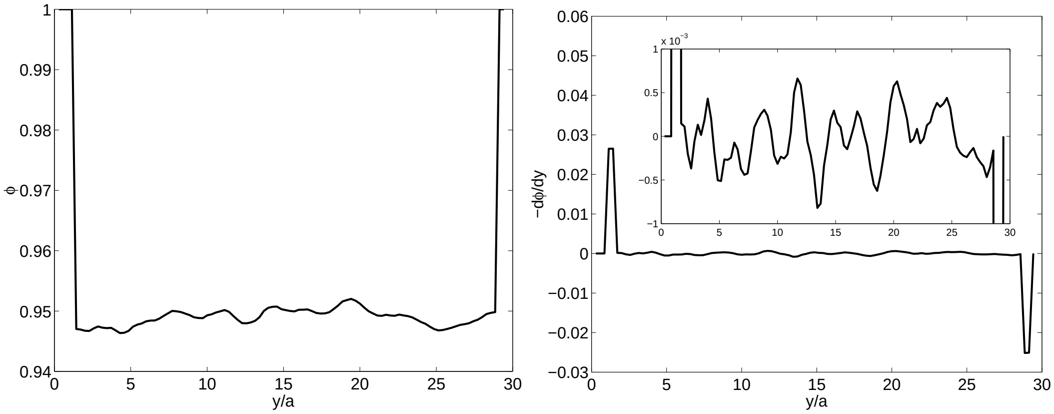

Figure 3.17: The porosity ϕ (left) and the derivative of the porosity $\mathrm{d}\phi/\mathrm{d}y$ as a function of the dimensionless distance y/a for gap width $\lambda = 4$.

The average volumetric lift force density was calculated from the simulated particle distributions of the LB method by subtracting the effect of the average pressure. Thus the gradients in the local porosity do not contribute to the result, and one may expect the calculated lift force to equal L_s. The calculated forces are shown in Figs. 3.18-3.20 as open symbols. The lift force density L_s defined by Eq. (3.41) was also calculated. The results are shown in Figs. 3.18-3.20 as a solid line. The relative difference between the lift force calculated at the link level with the effect of the average pressure subtracted, and the lift force calculated using Eq. (3.41) is of the order 10% at most in the repulsive region near the moving wall.

The results shown in Figs. 3.18- 3.20 now reveal similar behaviour of lift force for the random array of cylinders as was earlier found for the case of unidirectional cylinders (see Fig. 3.11). There is a strong repulsive (positive) force near the moving wall, and the force approaches zero near the stationary wall. Interestingly, the repulsive lift force is in maximum not at the surface of the cylinder matrix, but inside the matrix at a small distance (a few lattice spacings) from the surface. After the maximum, the repulsion decays with increasing distance from the moving wall within a distance $\Delta y/a \approx 5 - 10$. This distance is larger than the corresponding distance of $\Delta y/a \approx 2 - 3$ in the case of unidirectional cylinders. It should

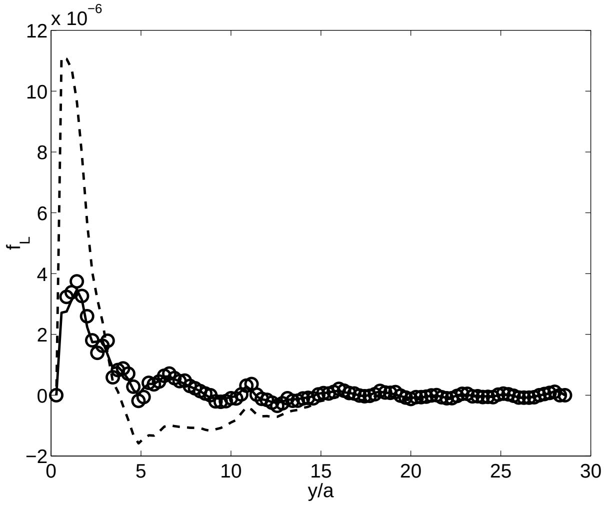

Figure 3.18: The volumetric inertial lift force density L_s vs. dimensionless distance y/a for gap width $\lambda = 1$. Open markers are calculated directly from the particle distributions of the LB method, the solid line is given by Eq. (3.41), and the dashed line by Eq. (3.41) with the pseudoturbulent term omitted. The force density is given in lattice units.

also be noticed that in the current case one cannot find any region of notable attractive (negative) lift force next to the repulsive region, but the lift force approaches zero more or less monotonically as the distance from the moving wall increases. On the other hand, there seems to be a narrow region of attraction at the surface of the solid matrix in the case of the gap with $\lambda = 8$. The origin of this possible attraction is not known. As for the unidirectional cylinders, the major effect of increasing the width of the fluid gap is to truncate the repulsive peak as the gap widens.

In order to study the effect of the pseudoturbulent term, the lift force density was calculated from Eq. (3.41) by omitting the pseudoturbulent stress. The results are shown in Figs. 3.18-3.20 as dashed lines. Clearly, there is a large difference between the lift forces calculated with and without the pseudoturbulent term. At the maximum of the repulsive lift force, the difference is more than 100%. One may thus conclude that the pseudoturbulent velocity fluctuations contribute substantially to lift force.

The total drag and lift force acting on the cylinders were also calculated by integrating the corresponding force densities in the y-direction from the moving wall to the stationary wall:

$$P_D \quad = \int_0^{\lambda+w} D_{s,x}\,\mathrm{d}y \tag{3.44}$$

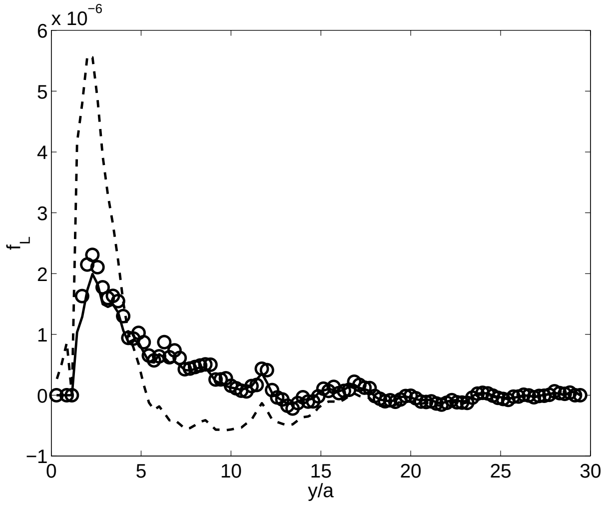

Figure 3.19: Same as Fig. 3.18 but for gap width $\lambda = 4$.

$$P_L \quad = \int_0^{\lambda+w} L_s \,\mathrm{d}y. \tag{3.45}$$

The integrated total drag and lift forces are shown in Fig. 3.21 as a function of the dimensionless gap width λ/a. The qualitative behaviour of these forces is quite similar to the case of parallel cylinders (see Fig. 3.12). Both the total forces decrease monotonically as the gap with increases. Notice however, that for the parameters used in the current study, the integrated lift force remains nonnegative. Further simulations would be required to check whether the total lift force will become attractive as the gap width is increased beyond $\lambda = 8$.

3.5 Summary

It was found that hydrodynamic lift force, *i.e.* force perpendicular to the main flow direction, *do* exist in the flows of liquid-particle suspensions. This force arises due to inertial effects, and is thereby complicated and rather poorly known even for a case where a single particle is suspended in the flow.

In the case where there is a single cylinder suspended in a flow near a solid wall, it was found that the nondimensional hydrodynamic drag and lift forces mainly depend on two nondimensional parameters, namely the dimensionless distance from the wall, and the ratio of the slip

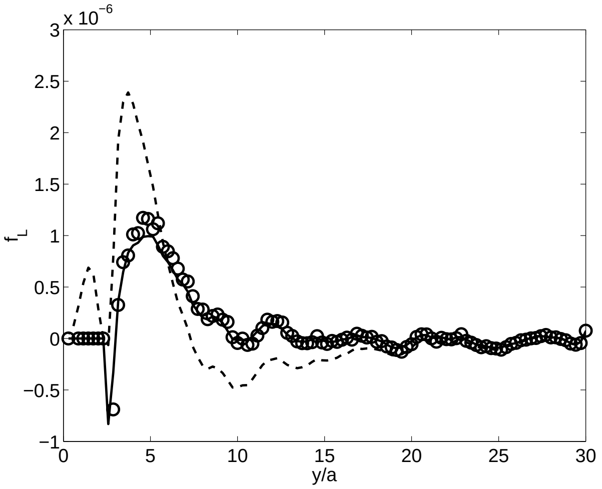

Figure 3.20: Same as Fig. 3.18 but for gap width $\lambda = 8$.

Reynolds number to the shear Reynolds number. It was also found an analytic expression of these parameters that reproduce the simulation results with reasonable accuracy.

It was found that the hydrodynamic force acting on a rigid matrix of long cylinders is qualitatively similar both for a matrix of unidirectional cylinders and for a matrix of cylinders with random orientation. The drag force is largest near a moving wall and approaches zero monotonically with increasing distance from the wall. Close to the moving wall the simulated drag force deviates considerably from the drag force predicted by Darcy's law. To account for for this difference, the single particle results were referred to. These results involve an increase in the drag force as the distance from the moving wall is decreased and the other local flow conditions are kept constant. The total drag force acting on the cylinder matrix is highest when the gap width is small, and decreases monotonically with increasing gap width.

Numerical simulations indicate strongly repulsive lift force near the moving wall, and the maximum value of repulsion decreases as the gap width is increased. This strong repulsion decays within a distance that is $2-3$ times the cylinder radius and $5-10$ times the cylinder radius for unidirectional and random orientations of the cylinders, respectively. At that distance, the lift force acting on unidirectional cylinders changes to weak attraction, which decays rapidly with increasing distance as the fluid velocity approaches zero. For randomly oriented cylinders no region of significant attraction was found. The total lift force acting on the cylinders is strongly repulsive when the gap width is small, and decreases monotonically with increasing gap width. For unidirectional cylinders, the total lift force changes into

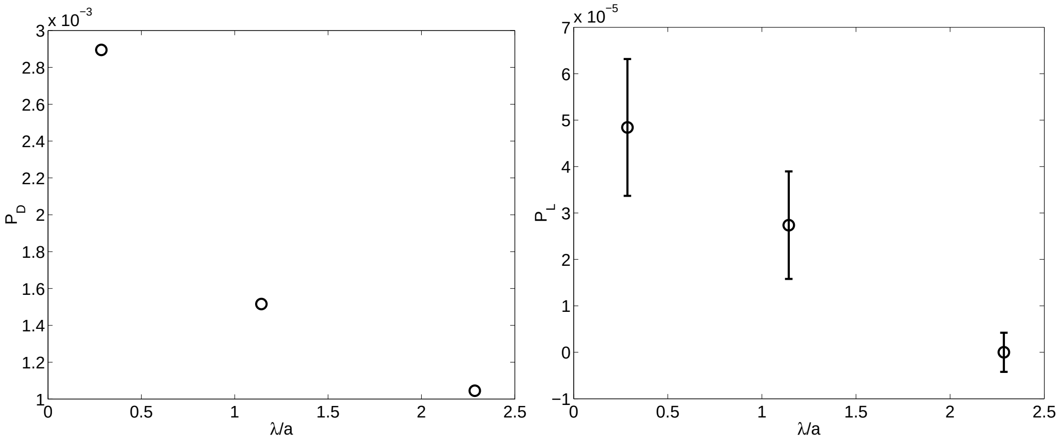

Figure 3.21: The total drag force (left) and lift force (right) acting on the cylinder matrix as functions of the dimensionless fluid gap width λ/a.

attraction at the distance that is of the order of the cylinder radius. For randomly oriented cylinders, the total lift remained repulsive in all the simulations, and was close to zero for the largest gap width used that was 2.3 times the cylinder radius.

The inertial lift force most likely accounts for a lubrication layer that is commonly believed to be responsible for much of the peculiar flow behaviour of wood fibre suspensions. Real wood fibre suspensions are, however, much more complex than the model systems used in this study. The particular results quoted in this chapter may thus not be very helpful in quantitative analysis of the flow of real suspensions. The result do, however, give some physical insight of the relevant phenomena in such flows, and this insight is utilized in interpreting experimental results and in modeling the flow behaviour of wood fibre suspensions in next chapters.

Chapter 4

Flow behaviour of wood fibre suspensions in a straight pipe

In this chapter a summary of the well known qualitative features of fibre suspension flow in a straight pipe is given. Efforts on modeling the flow of wood fibre suspension in straight pipes and on design equations and methods for determining friction loss are reviewed. This chapter is closed by studying the formation of fibre flocs and coherent fibre networks in various flow regimes. The most relevant stochastic approaches to calculate the average number of fibre contacts are shortly reviewed. Based on these results, the threshold consistency is estimated above which a coherent and percolating fibre network may form.

4.1 Qualitative analysis of friction loss

Figure 4.1 shows measured friction loss for unbleached suplhite pulp in a copper pipe of diameter 200 mm. According to Duffy [Duf97], the flow behaviour can be roughly divided in two main regimes: the plug flow regime that occurs at low flow rates and the drag reduction regime that occurs at high flow rates [LD76]. Within the plug flow regime the fibre phase moves as a continuous fibre network with solid like properties and with no shearing motion. In this regime, the loss is high compared to that of the carrier fluid (usually water) at the same flow rate. Furthermore, the dependence on flow rate of loss can be quite complicated. In some cases the loss may decrease with increasing flow rate. In the drag reduction regime, the fibre

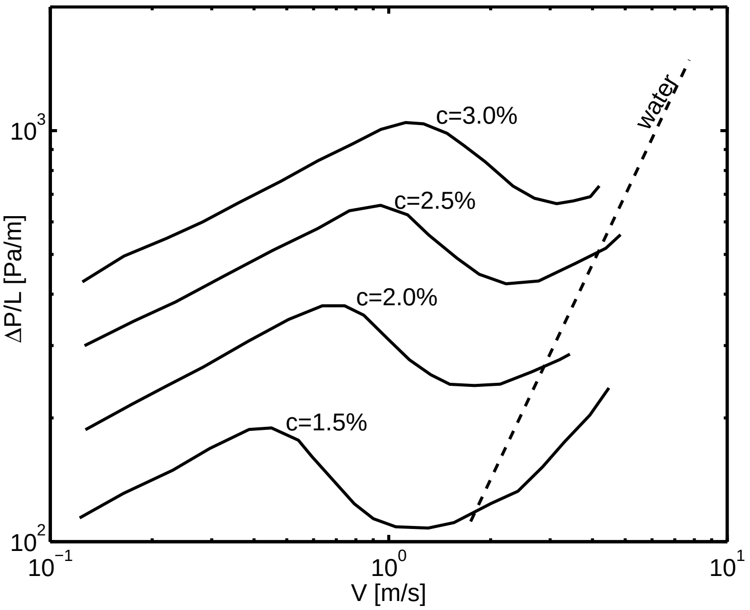

Figure 4.1: Friction loss vs. flow velocity for unbleached sulphite pulp in a $\phi = 200\,\text{mm}$ copper pipe. The data is reproduced from Fig. 5 of Ref. [Bh50].

network is partly or entirely broken into flocs that undergo turbulent and shearing motion. Characteristic to this region is that the frictional loss may be below that of a pure carrier fluid. These qualitatively different main regimes can be divided into several sub-regimes. If the pressure gradient applied to the pipe is below some threshold value that depends on fibre type and consistency, the fibre plug does not move at all and the motion of the carrier fluid is described as a flow through porous medium. Above the threshold pressure gradient, also the fibre plug is set into motion. The fibres are first in a direct contact with the wall inducing high shear stress (high loss). As the flow rate is increased, a plug flow behaviour is preserved, but a thin layer of pure water (a 'lubrication' layer) is created next to the wall. Characteristic to this flow regime is that the wall friction is approximately constant, and may even decrease with increasing flow velocity. As the flow rate increases further, turbulent flow appears near the walls and the fibre plug begins to break from its outer surface. Thus, in this mixed flow regime a turbulent fibre annulus surrounds a rigid fibre plug in the middle of the pipe. At some point, frictional loss falls below that of the carrier liquid and drag reduction regime is obtained. As the flow rate is still increased, the solid fibre core gradually vanishes indicating fully turbulent or 'fluidized' flow regime. Here, the loss typically approaches the pure fluid curve asymptotically as the flow rate is increased. This quite generally accepted view on the different flow domains was originally based on loss measurements, visual observations of the flow near the pipe wall and on velocity profile measurements made at turbulent region using a specific annular-purge impact probe [Duf97, LD76].

4.2 Design methods and flow models

For the practical design purposes the results of extensive loss studies have traditionally been published in a graphical form, see *e.g.* Ref. [Bh50]. These graphical correlations have been used, *e.g.*, to estimate the frictional losses for pipe diameters that were not included in the original measurement. Later, specific design equations have been developed for the regime before the maximum in the loss curve, see Ref. [Duf76] for a extensive review and evaluation of these equations. These equations are usually expressed in a generic form

$$\frac{\Delta P}{L} = K q^{\alpha} c^{\beta} D^{\gamma}, \tag{4.1}$$

where $\Delta P/L$ is the loss, q is the average flow velocity, c is the percentage consistency, D is the pipe diameter. In addition, the numerical coefficient K, and the dimensionless indices α, β, γ are constant for a given pulp.

Notice that Eq. (4.1) is flawed in a way that the dimension of the coefficient K depends on the values of the indices α, β, and γ. This deficiency is an inevitable result of the fact that the equation is just a numerical fit in the experimental data with little or no physical reasoning. The fundamental reason for this shortcoming is that Eq. (4.1) does not include all the relevant physical dimensional quantities.

As an example of dimensionally sound form of loss correlation, a plausible set of relevant physical quantities is included in the analysis . The loss depends on the viscosity μ_{f} and the density ρ_{f} of the carrier fluid, in general. The extra shear stress (mechanical friction) τ_{s} is also taken into account that acts on the fibres at the pipe wall, and the permeability of the fibre plug k. Solely based on dimensional analysis, one can write the following pressure loss correlation

$$\frac{\Delta P}{L} = \frac{\rho_{\mathrm{f}} q^2}{D} f\left(\frac{\rho_{\mathrm{f}} q D}{\mu_{\mathrm{f}}}, \frac{\tau_{\mathrm{s}}}{\rho_{\mathrm{f}} q^2}, \frac{k}{D^2}, c\right), \tag{4.2}$$

where the form of the function f is still unknown, and it may be inferred,*e.g.*, from a adequate set of experimental results. Notice that all the parameters of the function f are dimensionless, and the correct dimension result from the factor $\rho_\mathrm{f} q^2/D$. In a case where the function f can be written as a power law of its parameters, one can write the loss correlation in the form analogous to Eq. (4.1):

$$\frac{\Delta P}{L} = \frac{\rho_\mathrm{f} q^2}{D} \left(\frac{\rho_\mathrm{f} q D}{\mu_\mathrm{f}}\right)^{\alpha_1} \left(\frac{\tau_\mathrm{s}}{\rho_\mathrm{f} q^2}\right)^{\alpha_2} \left(\frac{k}{D^2}\right)^{\alpha_3} c^{\alpha_4}, \tag{4.3}$$

where α_1, α_2, α_3, and α_4 are dimensionless constants. Notice that in Eq. (4.3), the dependence on the flow rate of the loss is not isolated to any single power factor on the right side of the equation, but the loss scales with the flow rate q to the power $2 + \alpha_1 - 2\alpha_2$. Likewise, the loss scales with the diameter D to the power $-1 + \alpha_1 - 2\alpha_3$.

Notice that Eq. (4.3) can be applied to flow of water by setting to zero the exponents α_2–α_4 of the unrelevant quantities τ_s, k, and c. Blasius found that for water $\alpha_1 \approx -1/4$[Whi06]:

$$\frac{\Delta P}{L} \approx 0.1584 {\rho_\mathrm{f}}^{3/4} q^{7/4} \mu_\mathrm{f}^{1/4} D^{-5/4}. \tag{4.4}$$

In practical design tasks, the effect of drag reduction has traditionally been neglected, and at the flow rates above the onset of drag reduction (where the loss curve of pulp intersect that of water) the loss curve of water has been used as a conservative approach to be on the safe side. Despite this common reluctance to adopt the concept of drag reduction, Møller and Duffy have derived an empirical loss correlation in the transitional regime [KD78]. They assumed that the amount of the drag reduction scales with the area of the fluidized fibre annulus and derived the following correlation

$$\tau'_w = \frac{\tau_w^3}{(1-\Lambda)\tau_w^2 + \Lambda \tau_D^2} \tag{4.5}$$

where τ_w and τ'_w are the wall shear stresses for the pulp suspension and for water for a given flow rate, respectively, τ_D is the wall shear stress at the onset of the drag reduction, and Λ is the maximum fractional drag reduction. Equation (4.5) can be fit in the experimental data between the onset of drag reduction and the maximum level of drag reduction.

There are design procedures that have been developed to cover a wide range of flow velocities and consistencies. One of these procedures is documented in Ref. [TIS88], and is depicted in Fig. 4.2. In this procedure, the loss curve is partitioned into three regimes by distinct velocities q_1 and q_2. The velocity q_1 corresponds to the maximum in the loss curve, and q_2

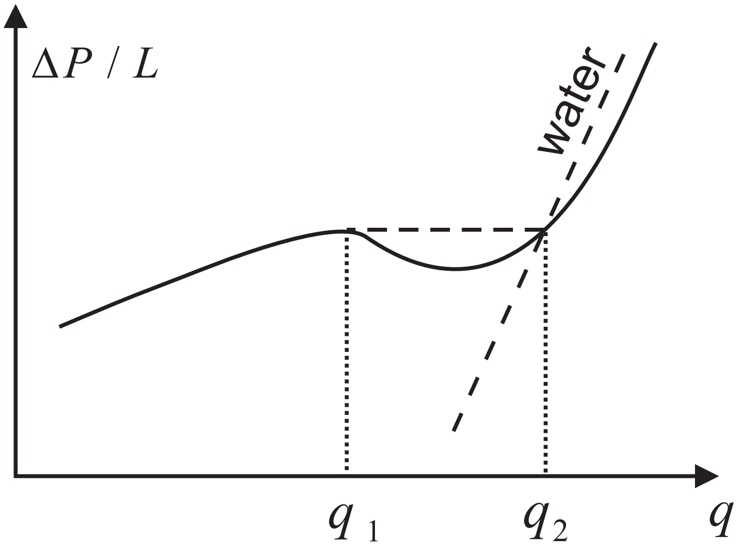

Figure 4.2: Schematic view of the design method proposed in Ref. [TIS88]

corresponds to the onset of the drag reductions. These velocities are calculated from the following correlations

$$q_i = K_i c^{\sigma_i}, i = 1, 2 \tag{4.6}$$

where K_i and σ_i are constants for a given pulp. Equation (4.1) is used to calculate the loss in the first regime $q < q_1$. The value of the loss at its maximum, *i.e.* the value given by Eq. (4.1) with $q = q_1$, is used for the middle regime $q_1 < q < q_2$. In the high velocity regime $q > q_2$, the loss is calculated from the standard correlation for water at the same flow conditions.

Even though the lubrication layer is known to be responsible for much of the peculiar flow behaviour of wood fibre suspensions, there are only a few attempts to calculate or model the thickness of the layer. In what follows, a very simple correlation between the thickness of the lubrication layer and the loss data is derived by considering the fibre plug as porous material. In that case, the plug moves with constant velocity and all the shearing takes place inside the lubrication layer. The flow velocity inside the lubrication layer is given by the Poiseuille parabolic profile, and the flow velocity inside the fibre plug is constant. Furthermore, the no-slip condition is applied on the plug surface, thus the velocity of the plug equals the velocity of the fluid at the surface. With these assumptions one can derive the following correlation for the width of the layer

$$h = R\left[1 - \left(1 - \frac{4\mu_{\mathrm{f}} q}{\tau_{\mathrm{w}} R}\right)^{1/4}\right], \tag{4.7}$$

where R is the pipe radius, τ_{w} is the wall shear stress, and q is the flow velocity. For very small values of h, the velocity profile inside the lubrication layer can be approximated by the linear Couette profile, and the correlation for the layer width simplifies into the form

$$h = \mu_{\mathrm{f}} \frac{q}{\tau_{\mathrm{w}}}, \tag{4.8}$$

which states the linear relationship between the shear stress τ_{w} and the shear rate q/h. Stenuf and Anumolu applied Eq. (4.8) on an extensive set of loss data for bleached softwood pulp at consistencies between 1% and 3.4%, and derived the following correlation for the thickness of the lubrication layer [SA72]

$$h = Kc^{-2.90} q^{1.36} (\alpha/\alpha_0)^{-0.26} (\sigma/\sigma_0)^{0.56}, \tag{4.9}$$

where K is a constant, α is the specific volume, and σ is the specific surface. The variables width subscript zero correspond to unbeaten pulp.

Møller et al. [MDT71] explained the formation of the lubrication layer in terms of elastic deformation of the fibre plug caused by hydrodynamic shear stress. In this “linear elastic solid” model, the local shear strain α of the fibre plug is a linear response to the local shear stress τ

$$\tau = G\alpha \tag{4.10}$$

where G is the shear modulus. The local shear stress varies linearly with radial distance r from the pipe axis:

$$\tau = \left(\frac{\Delta P}{L}\right) \frac{r}{2}. \tag{4.11}$$

The thickness h of the lubrication layer was found by integrating the local shear strain given by Eqs. (4.10) and (4.11) from the pipe axis to the pipe wall. Møller et. al. derived the following correlations

$$q = \left(\tfrac{\Delta P}{L}\right)^3 \tfrac{R^4}{48G^2\mu_{\mathrm{f}}} \tag{4.12}$$

$$h = \left(\tfrac{\Delta P}{L}\right)^2 \tfrac{R^3}{24G^2}. \tag{4.13}$$

Myréen modeled the flow of paper pulp as a non-Newtonian fibre core surrounded by an annulus of Newtonian fluid [Myr98a, Myr98b]. The fibre core was considered as pseudoplastic fluid, and the local shear stress $\tau(r)$ was written as a power law of local shear rate $\mathrm{d}u_\mathrm{f}/\mathrm{d}r$:

$$\tau(r) = K \left| \frac{\mathrm{d}u_\mathrm{f}}{\mathrm{d}r} \right|^n , \tag{4.14}$$

where K is a dimensional constant, and n is a dimensionless constant. In the viscous flow regime, that is in the low flow rate regime where the fibres are in contact with the pipe wall, Myréen ended up with the following loss correlation:

$$\frac{\Delta P}{L} = 2 \left(\frac{3n+1}{n} \right) K q^n R^{-n-1}. \tag{4.15}$$

Comparing the exponents of Eq. (4.15) with those of Eq. (4.1), one may find the following identities for the exponents: $\alpha = n$ and $\gamma = -n-1 = -\alpha-1$. As an example, the exponents for the original data of Brecht and Heller are $\alpha = 0.36$ and $\gamma = -1.33$ [TIS88], which meet this equality quite accurately.

In the plug flow regime where the lubrication layer surrounds the fibre core, Myréen expressed the flow velocity at the plug surface of the fluid as

$$u_\mathrm{f}|_{r=R-h} = sq, \tag{4.16}$$

where s is a dimensionless slip factor. Moreover, he wrote the thickness of the lubrication layer in the form

$$h = x h_\mathrm{max}, \tag{4.17}$$

where the factor x is in the range $0 < x < 1$. The maximum layer thickness h_max corresponds to the value of 30 of the non-dimensional wall-layer variable y^+, *i.e.*

$$h^+_\mathrm{max} = \frac{h_\mathrm{max}\rho_\mathrm{f}}{\mu_\mathrm{f}} \sqrt{\frac{\tau_w}{\rho_\mathrm{f}}} = 30. \tag{4.18}$$

With these definitions, the following loss correlation was derived

$$\frac{\Delta P}{L} = \frac{2}{R} \mu_\mathrm{f} q \frac{s}{h} = \frac{1}{2R} \times f \times \frac{1}{2} \rho_\mathrm{f} q^2, \tag{4.19}$$

where the friction factor f is given by

$$f = 0.0089\frac{s^2}{x}. \tag{4.20}$$

Skali Lami considered the plug flow regimes, and modelled the width of the lubrication layer with the linear elastic model given by Eq. (4.10) [Sl91]. In solving the velocity profile of the fluid phase, he considered the fluid pseudoturbulence created by irregular surface of the fibre plug. He wrote the presudoturbulent stress of the fluid phase in the form that is proportional to the square of the local velocity gradient,

$$\tau_{\delta xy} = -\langle \rho_\mathrm{f} \delta u_{\mathrm{f},x} \delta u_{\mathrm{f},y} \rangle = \mathcal{L}^2 \left(\frac{\mathrm{d}\, u_{\mathrm{f},y}}{\mathrm{d}\, y} \right)^2, \tag{4.21}$$

where the factor $\mathcal{L}$ determines the magnitude of pseudoturbulent stress. In his model, Skali Lami divided the flow into four domains according to the radial position. Next to the wall there is a viscous domain, *i.e.* $\mathcal{L} = 0$, with linear velocity profile. In the next domain that spans from the inner edge of the viscous domain to the outer edge of the fibre plug, the pseudoturbulence factor increases linearly with distance from zero to the maximum value of $\mathcal{L} = k\epsilon$, where k is a constant and ϵ is the surface roughness of the fibre plug. The next domain is the layer corresponding to the surface roughness of the fibre plug. In this domain the pseudoturbulence factor has a constant value $\mathcal{L} = k\epsilon$. Inside the core of the fibre plug the velocity profile is assumed to be constant and equal to the velocity of fibre plug. Based on these assumptions, Skali Lami derived the following correlation for the wall shear stress

$$\tau_w = A\tau_{w,\mathrm{water}} \left(\frac{\mathrm{R}e}{\mathrm{Sk}^{1.185}} \right)^{-1.35}, \tag{4.22}$$

where A is a nondimensional constant, $\tau_{w,\mathrm{water}}$ is the wall shear stress for water (at the same flow rate), $\mathrm{R}e = \rho_\mathrm{f} q D/\mu_\mathrm{f}$ is the pipe Reynolds number, and Sk is a constant that depends on consistency, in general. Even though Skali Lami derived the correlation given by Eq. (4.22) for the plug flow regime, he applied it successfully to the fully turbulent flow regime as well.

Hammarström considered wood fibre suspension as a single-component fluid with non-Newtonian viscosity, and modelled the effect of the lubrication layer with a slip velocity that is proportional to the wall shear stress [Ham04]. He wrote the slip model in the form

$$\tau_w = F u_{\text{slip}}, \tag{4.23}$$

where F is a constant and the slip velocity u_{slip} is the velocity at the surface of the fibre plug. The parameters of the model were found by a direct least-squares fit in experimental loss data for straight pipes. The modeled velocity profiles in straight pipes agreed with good accuracy with experimental velocity profiles. Hammarström implemented the model in a computational fluid dynamic solver as well, and applied it for flows in more complex geometries, *e.g.* a flow past an abrupt contraction.

The models reviewed above range from simple numerical fits in experimental loss data to more complex theoretical models that take into account some of the relevant physical properties of the flow process. Some of the models are not in a closed form ready for the solution, but can be used, *e.g.*, to estimate the thickness of the lubrication layer based on experimental loss data. The validity of the assumptions made in some of these models will be studied while discussing the experimental results in Chapter 5.

4.3 Fibre interactions, flocculation and coherent networks

The unique behaviour of wood fibre suspensions relates to the elongated shape of wood fibres. Due to the high aspect ratio and complicated surface structure of fibres, the non-uniformity of spatial fibre distribution, *i.e.* fibre flocculation, and the mobility of fibres in a suspension depend strongly on the consistency of the suspension. In this section the characterization of fibre flocculation regimes is discussed, and how these regimes are related to the aspect ratio of fibres and the consistency of the suspension. Next the nature of fibre contacts in fibre flocs and percolating fibre networks is discussed. This section is closed by reviewing some basic stochastic efforts to derive correlations between the suspension consistency and the average number of persistent contacts that each fibre may have with other fibres. These correlations will provide estimates for the minimum consistency at which coherent fibre networks can be formed.

4.3.1 Effect of consistency and fibre aspect ratio on the fibre flocculation

Let us consider a fibre that moves and rotates freely in a very dilute fibre suspension. One may associate two volumes to such a fibre, namely the spherical volume swept by the fibre as it rotates, and the average system volume available to the fibre (the volume of the system divided by the number of fibres). The spherical volume covered by the fibre has a maximum diameter equal to the length of the fibre. In a very dilute case this spherical volume is much larger than the average volume available to the fibre, and the fibre can move relatively freely without colliding with other fibres. Mason proposed that the interactions between fibres become important as a critical consistency is exceeded [Mas54]. He calculated this consistency from a condition that there is exactly one fibre in a spherical volume that has diameter equal to the length of a single fibre. The corresponding solid volume fraction is

$$\phi_{\mathrm{s,crit}} = \frac{3}{2}A^{-2}, \tag{4.24}$$

where $A = L/d$ is the aspect ratio of fibres, and L is the length and d the diameter of fibres. For a typical value of the aspect ratio $A = 70$ for pine fibres, Eq. (4.24) predicts $\phi_{\mathrm{s,crit}} = 0.03\%$.

Kerekes and Schell extended the analysis and defined a new parameter N called ”crowding factor” that is the number of fibres in a spherical volume that has diameter equal to the length of a single fibre [KS92]. They studied the degree of flocculation in a flow of decaying turbulence, and based on the value of the crowding factor, they partitioned the flocculation of suspensions into three regimes. Soszynski and Kerekes had found the same regimes in an experiment they deviced with nylon fibres, but they did not provide any numerical criteria for the regimes[SK88].

In a dilute regime the crowding factor $N < 1$, *i.e.* below the critical limit given by Eq. (4.24), fibres are free to move and they collide only occasionally due to translational motion. In this regime the fibre distribution is relatively uniform as was reported by Soszynski and Kerekes[SK88].

The rate of collisions increases with the crowding factor, and in a semiconcentrated regime $1 < N < 60$ collisions take place also due to rotational motion of fibres. In this regime the fibre non-uniformity increases with increasing consistency, and in the local areas of high concentration, fibres may form small networks called flocs. The mechanical strength of these flocs is very low, and they are easily torn apart by the hydrodynamic forces created by the flow of suspending liquid. The flocculation reaches a dynamic equilibrium where flocs are in a state of continuous dispersion and formation. Soszynski and Kerekes rediluted the suspension in their experiment and found that flocs disappeared and the uniformity increased as the consistency decreased, and the suspension returned to the uniform state if rediluted below the critical limit $N = 1$.

As the crowding factor is increased further, the number of persistent contacts between fibres increases, and in a concentrated regime $N > 60$ the mobility of fibres decreases significantly. Fibres form local coherent networks that have sufficient strength to tolerate the hydrodynamic forces created by a moderate flow of suspending liquid, and intensive agitation of the suspension is needed to disperse the coherent flocs. Moreover, Soszynski and Kerekes found in their experiment that the coherent flocs do not disperse even in the case where the suspension is rediluted below the critical limit $N = 1$. Notice that there is no unique crowding number associated with the formation of coherent flocs, but the limit depends on the fibre type, and was found to be in the range $60 < N < 130$.

Obviously further increase in the consistency will increase the number of coherent flocs, and for high enough consistency these coherent flocs will come into contact with each other and form a network percolating through the system.

So far the formation of fibre networks in a flow of decaying turbulence, which is the case in many paper making processes, has been discussed. The other way of forming fibre networks is by sedimenting, either due to gravity in quiescent fluid or in a uniform flow through a filtrating device, *e.g.* a wire in a hand-sheet mould. Here the sedimentation by gravity will be shortly discussed, as it is used to infer one parameter that is often used to characterize fibre suspensions, namely sediment consistency. The average density of saturated wood fibres is higher than that of water, thus free fibres will fall down in quiescent fluid under the influence of the gravitational field. As the fibres fall down, the average consistency of the sedimenting layer will increases and eventually it will enter the semi-concentrated regime. The fibres will form flocs that will come into contact with each other as the consistency continues to increase. The fibres will eventually settle down at the bottom of the container, where they will form a network percolating between the walls of container. The average consistency of this network is called sediment consistency. Notice however, that the consistency of the sedimenting suspension will not reach a well-defined stationary value. On the contrary, the consistency continues to increase slowly for a very long period of time, and in practice a stationary value is recorded after a certain time, *e.g.* 18 hours, of sedimentation.

In many cases the experimental sediment consistency corresponds approximately to the crowding factor value $N = 60$. Yet there is a salient difference in the properties of the fibre networks created in decaying turbulence or in sedimenting suspensions. As was discussed above, in the concentrated regime the flocs created by decaying turbulence are coherent, *i.e.* they can withstand moderate stresses and strong agitation of suspension is needed to disintegrate the flocs. The network in the sediment has, by contrast, quite low mechanical strength, and relatively small amount of stirring is enough to break the network and to make the fibres whirl. This difference in network strengths relates to the difference in the contacts between fibres. The nature of these contacts will be discussed next.

4.3.2 Mechanisms of fibre contacts

Three types of cohesion forces between fibres have been suggested, namely colloidal, surface tension, and mechanical[SK88]. The mechanical interaction can be further divided to hooking of fibres and/or fibrilles, interlocking by elastic bending of fibres, and drawing and twisting of fibres into threads. Depending on the pulping process, the shape of a fibre can become tangled and distorted. Some processes, *e.g.* beating, roughens the fibre wall uncovering the fibrillated wall structure. The resulting variety of fibre shapes and surface structure allows various forms of mechanical interlocking and electro-mechanical coupling.

It has been proposed that the mechanical interlocking is the main mechanism for the formation coherent flocs and coherent percolating networks [Mas54]. Soszynski and Kerekes examined the elastic interlocking of fibres in an experiment where the other types of cohesion were eliminated by using relatively straight and smooth nylon fibres [SK88]. The ranges of fibre dimensions, apparent densities, and flexibility were carefully chosen to closely match those of wood fibres. The fibres flowed in an inclined cylinder that rotated to produce moderately unsteady flow. In an initial state the consistency of the suspension was in the dilute regime, thus no flocs were visible and the fibre distribution was uniform. This state corresponds to the dilute crowding factor regime $N < 1$. The consistency was increased, and at some well-defined concentration the suspension shifted from the state of uniform dispersion to a cloudy state where the clouds were temporary noncoherent flocs. Redilution of the suspension broke these weak flocs and the suspension resumed the uniform state. This regime corresponds to the semi-concentrated crowding factor regime $1 < N < 60$. The consistency was increased further, and at some well-defined threshold consistency the suspension changed from the cloudy state to a grainy state. In this state the fibres formed persistent flocs that remained identifiable through the unsteady flow. Moreover, these coherent flocs remained intact even though the suspension was rediluted to the point where the average consistency was at the initial level. This regime corresponds to the concentrated crowding factor regime $N > 60$.

Soszynski and Kerekes demonstrated the nature of the mechanical cohesion between the fibres by picking up a few coherent flocs out of the cylinder and applying heat on them to relax the elastic stresses. These heat-treated flocs were brought back into the rotating cylinder where they dispersed immediately due to hydrodynamic stresses applied by the unsteady flow. This indicates that the formation of the coherent flocs was by interlocking by elastic bending. The experiment reviewed above was carried out with nylon fibres. However, the fibre properties were closely matched with those of wood fibres, thus there is a strong possibility that same kind of elastic bending is responsible for the formation of coherent fibre networks in wood-fibre suspensions as well.

Soszynski and Kerekes found that coherent flocs are created only if the consistency of suspension exceeds a well-defined threshold value that depend largely on the fibre aspect ratio [SK88]. This supports the results reported by Thalén and Wahren that certain mechanical properties of paper pulp can be measured only if the fibre content of the pulp is high enough [TD64]. Thalén and Wahren measured the shear modulus G in an elasto-viscometer for a number of paper pulps. They found that the shear modulus and the ultimate shear strength can be measured only above a certain limiting consistency. The values of this limiting consistency they detected were only slightly higher than the sediment consistency c_s. They reported their result in the form

$$\begin{aligned} G &= G' \left(\tfrac{c-c_\mathrm{s}}{0.1\%}\right)^{k_G} && (4.25)\\ \tau_\mathrm{u} &= \tau' \left(\tfrac{c-c_\mathrm{s}}{0.1\%}\right)^{k_\tau}, && (4.26) \end{aligned}$$

where G and G' (τ_u and τ') is the shear modulus (the ultimate shear strength) at the consistency c and $c = c_s + 0.1\%$, respectively, and k_G (k_τ) is a dimensionless constant. The limiting consistency measured by Thalén and Wahren [TD64], the sediment and threshold consistencies measured by Soszynski and Kerekes [SK88], and the consistency corresponding to he lower limit $N = 60$ of the concentrated regime coincide with moderate accuracy (see Fig. 4.3).

4.3.3 Stochastic analysis and threshold consistency

The crowding factor can be expressed in the form (see Eqs. (A.3) and (A.5))

$$N = \frac{\pi}{6}\frac{c_m L^2}{\omega} = \frac{2}{3}\phi_{\mathrm{s}} A^2, \tag{4.27}$$

where c_m is the consistency of the suspension, L is the length of a fibre, and ω is the fibre coarseness (mass per unit length). Real wood fibres come in variety of lengths even for a small sample of one species. Thus, the fibre length L in Eq. (A.3) is not uniquely defined. Kerekes and Schell recommended that the average fibre length be used when calculating the crowding factor. Huber *et al* extended the calculation of the crowding factor to the case of general fibre-length distribution [HRGP03].

The value of $N = 60$ for the crowding factor is used normally as the lower limit for the concentrated regime, *i.e.* it corresponds to the lowest consistency at which fibres form a coherent network. The corresponding volume fraction $\phi_{\mathrm{s}0}$ is calculated by setting $N = 60$ in Eq. (4.27), and the result is

$$\phi_{\mathrm{s}0} = \frac{90}{A^2}. \tag{4.28}$$

The quantity $\phi_{\mathrm{s}0}$ is quite often referred to as the sediment solid (volume) fraction. Due to vagueness of the definition for the sediment consistency that was discussed above, the quantity $\phi_{\mathrm{s}0}$ from now on will be called the threshold volume fraction.

Meyer and Wahren examined the correlation between the volumetric concentration of fibres, the average number of contacts per fibre, and the aspect ratio of fibres A [MD64]. They took into account the fibre length distribution and the fibre diameter distribution. In a case where all fibres are of the same length, they found the following correlation between the solid volume fraction ϕ_{s} and the average number of contacts per fibre n:

$$\phi_{\mathrm{s}} = \frac{16\pi A}{\left(2A/n + n/(n-1)\right)^3 (n-1)}. \tag{4.29}$$

They proposed that fibres may form a coherent network only if, on the average, every fibre is locked in position by contact with at least three other fibres and in such a way as to be

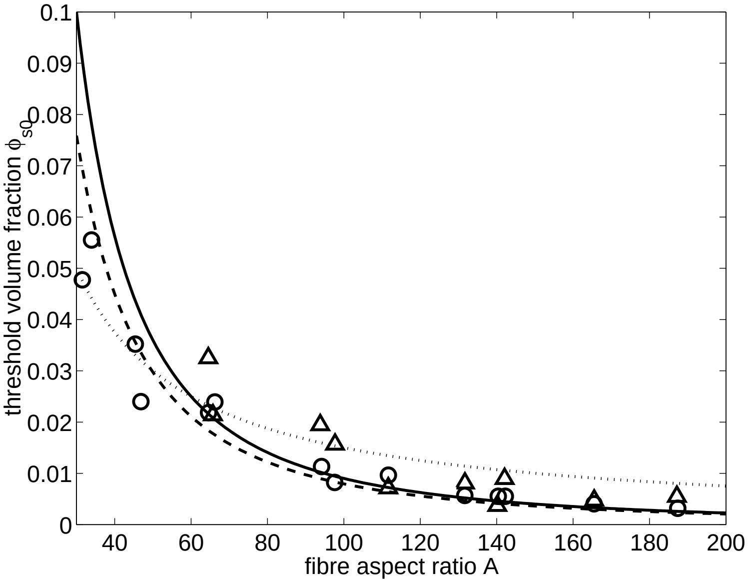

Figure 4.3: Sediment and threshold volume fraction as a function of fibre aspect ratio. Solid line is given by Eq. (4.28), dashed line by Eq. (4.30), and dotted line by Eq. (4.32). Open triangles and circles are the threshold and sediment volume fractions, respectively, as measured by Soszynski and Kerekes (this data is reproduced from Fig. 7 of Ref. [SK88]).

able to transmit forces. Thus one can calculate an estimate for the threshold consistency by setting $n = 3$ in Eq. (4.29):

$$\phi_{s0} = \frac{8\pi A}{\left(\frac{2A}{3} + \frac{3}{2}\right)^3} \tag{4.30}$$

Dodson considered fibres as circular cylinders, and with a simple geometrical analysis he found that the average number of contacts per fibre scales with the crowding factor as[Dod96]

$$n = \frac{3N}{A} = 2\phi_s A. \tag{4.31}$$

By setting $n = 3$ in Eq. (4.31) the threshold volume fraction is solved as

$$\phi_{s0} = \frac{3}{2A}. \tag{4.32}$$

In Fig. 4.3 is shown the threshold volume fraction ϕ_{s0} given by Eqs. (4.28), (4.30), and (4.32) as functions of fibre aspect ratio A. The scatter in this experimental data is due to weak dependence of the threshold and sediment consistencies on the fibre diameter (the diameter varied in the experiment form 19.8 μm to 44.2 μm). All the threshold and sediment volume fractions decrease with increasing aspect ratio. Equations (4.28) and (4.30) predict threshold volume fractions that are quite close to each other over a wide range of fibre aspect ratios. The difference is 25% at the aspect ratio $A = 30$ and decreases with increasing aspect ratio. Equation (4.32), on the other hand, gives a threshold volume fraction that is considerably lower for low aspect ratios and higher for high aspect ratios. The values predicted by Eq. (4.32) match quite well with the measured threshold values up to aspect ratio 100. The measured threshold volume fractions are in most cases higher than measured sediment volume fractions.

4.3.4 Fibre analysis and threshold consistency

Species	# fibres analyzed	L [mm]	d [μm]	A=L/d	ω [μg/m]	$\mathrm{MR_b}$
Pine	20000	2.04	27.7	71	147	3.5
Birch	45000	0.900	21.0	43	109	2.5

Table 4.1: Experimental results for the average fibre length L, the average fibre width d, and the coarseness of fibres ω. Also shown is the aspect ratio $A = L/d$ calculated from the physical dimensions, and the moisture ratio of bound water MR_b calculated from eq. (A.10).

In the experimental work of this thesis suspensions consisting of water and chemically released pine or birch fibres were studied. The physical dimensions of fibres were measured with a commercial fibre analyzer at Techinal Research Center of Finland[Haa]. In the analyzer fibres are aligned between two glass windows and imaged with a CCD camera. The fibre dimensions are calculated with image analysis. The results include, *e.g.* distributions for the fibre length and width, and the averages of these distributions. The total mass of dry fibres is measured before the analysis, thus the coarseness of fibres can be calculated too. The results for the average physical dimensions and coarseness are presented in Tab. 4.1. Also shown in the table is the aspect ratio $A = L/d$ calculated from the average physical dimension. Also shown in the table is the moisture ratio $\mathrm{MR_b}$ calculated using Eq. (A.10), the density of eater $\tilde{\rho}_\mathrm{w} = 1000\,\mathrm{kg/m^3}$, the density of cellulose $\tilde{\rho}_\mathrm{c} = 1500\,\mathrm{kg/m^3}$, and the cross-sectional area of fibres $A_0 = 1/4 \times \pi d^2$ (here round fibres are assumed).

The threshold consistency can be estimated by using the fibre properties presented in Table 4.1, the result presented in Sect. 4.3, and the correlations derived in App. A.2. The threshold solid volume fraction $\phi_{\mathrm{s}0}$, calculated using Eqs. (4.28), (4.30), and (4.32), are shown in the

	$\phi_{\mathrm{s}0}$	c_{m0} [kg/m^3]	c_0
Eq. (4.28)	0.018	4.3	0.43%
Eq. (4.30)	0.015	3.7	0.37%
Eq. (4.32)	0.021	5.1	0.50%

Table 4.2: The threshold values for solid volume fraction and consistency for pine fibres. The volume fraction $\phi_{\mathrm{s}0}$ is calculated from each of Eqs. (4.28), (4.30) and (4.32). For each value of $\phi_{\mathrm{s}0}$, the consistency c_{m0} is calculated from Eq. (4.33), and the percentage consistency c_0 from Eq. (4.34).

	$\phi_{\mathrm{s}0}$	c_{m0} [kg/m^3]	c_0
Eq. (4.28)	0.049	15.3	1.5%
Eq. (4.30)	0.039	12.4	1.2%
Eq. (4.32)	0.035	10.1	1.0%

Table 4.3: Same as Table 4.2 but for birch fibres.

second columns of Tables 4.2 and 4.3 for the pine and birch fibre suspensions, respectively. The corresponding values of the threshold consistency are calculated from Eq. (A.4), *i.e.*

$$c_{m0} = \frac{4\omega}{\pi d^2}\phi_{\mathrm{s}0}, \tag{4.33}$$

and the results are shown in the third columns of Tables 4.2 and 4.3. Finally, the values of the threshold percentage consistency are calculated from Eq. (A.20) by setting $c = c_0$ and $c_m = c_{m0}$,

$$c_0 = \left(\mathrm{MR_b} + r + (1-r)\frac{\pi d^2 c_{m0}}{4\omega}\right)^{-1}\frac{\pi d^2 c_{m0}}{4\omega}. \tag{4.34}$$

The results are shown in the third columns of Tables 4.2 and 4.3. Notice that in calculating threshold consistencies average values are used for all fibre properties and, *e.g.*, the coarseness is assumed to be same for all fibres of one species. In the modeling effort (see Chap. 6), the threshold values given by Eq. (4.32) will be used, as they are supported by the visual observations of the suspension state at various consistencies during the experiments. In addition, the threshold values predicted by Eq. (4.32) are in better agreement with experimental threshold values for $A < 100$ than those given by Eqs. (4.28) and (4.30), see Fig. 4.3.

Chapter 5

Experimental work

This chapter is started by describing the methods used in the experimental part of this work. Pulsed ultrasound Doppler method was used for measuring momentary velocity profiles, and a laser-optical method for measuring the thickness of the lubrication layer. These methods were applied to study the transient behaviour of the flow after a turbulence generator (sudden step), the approach to steady state flow, and the main features of fully developed flow. In particular, the various flow regimes are sought to be identified on the basis of direct measurements. The properties of the fibres used in the experiments were also measured. The results of the experiments are shortly reported after which each flow regime that was identified based on these results is studied in detail.

5.1 Measurement setup

The experiments were made in an laboratory-scale acrylic flow loop for birch and pine fibre suspensions. The flow was driven by a centrifugal pump, and the flow rate was measured using a magnetic flow meter. The flow loop was equipped with a differential pressure transducer for loss measurement. The velocity profile across the pipe was measured using pulsed ultrasound velocimetry. In a separate experiment, the thickness of the lubrication layer in the plug-flow regime was measured optically using a collimated laser beam guided inside the flow channel, and measuring the light scattered by fibres.

5.1.1 Ultrasound velocimetry

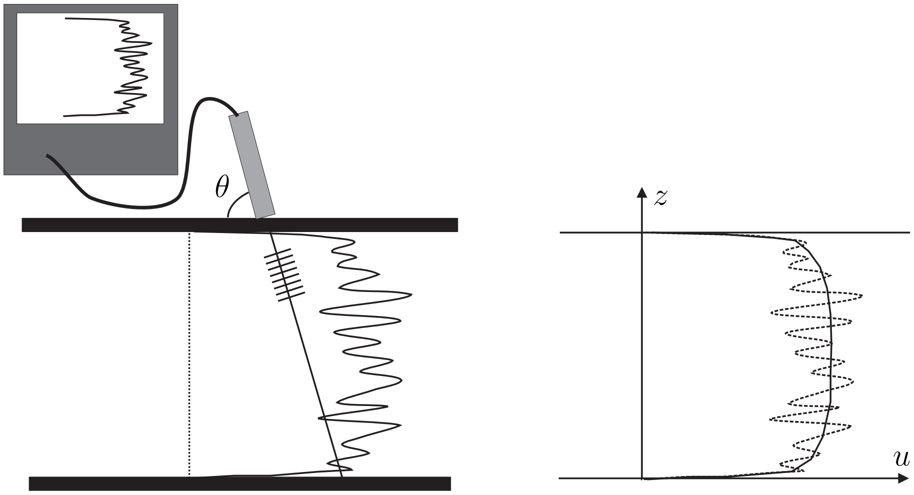

Figure 5.1: Left: The principle of the pulsed ultrasound Doppler velocimeter (PUDV). Right: One momentary velocity profile (dashed line) and the average of 3000 momentary velocity profiles (solid line).

The velocity profile across the pipe was measured using pulsed ultrasound velocimeter (PUDV) techniques, see Fig. 5.1. The measurement is based on using a transmitter to send short ultrasound pulses through the pipe wall and into the flow. Target particles (fibres) moving with the flow reflect the sound which is detected by the transmitter. The distance of the particle is found by the time-of-flight method using the known velocity of sound, and the velocity of the particle is calculated from the cross-correlation between the echoes from consequent pulses. Notice that the device thus measures the velocity component in the direction of the ultrasound beam. Within the present measurement, an ultrasound transmitter with the emitting frequency of 4 MHz was used. The angle between the axis of the probe (the direction of ultrasound beam) and the pipe wall was set to $\theta = 85°$. The duration of a single ultrasound pulse was selected as 4 wavelengths corresponding to a length 1.5 mm in water with the velocity of sound 1500 m/s. The repeating frequency of pulses was set to 15.6 kHz, thus the time delay between the emissions of two consequent pulses was 64.0 μs while a single pulse lasted only for 1.0 μs. The echo signal was sampled in 54 gates (windows) corresponding to 54 depth values with spacing 0.75 mm in the direction of ultrasound beam. A series of 32 pulse emissions was used to construct a single velocity profile $u_{\text{us}}(z_{\text{us}}, t)$, and 3000 profiles were collected during 20 seconds. Here u_{us} is the velocity component in the direction of the ultrasound beam and z_{us} is the distance along the beam axis from the front wall of the flow channel. Velocity profiles $u(z,t)$ were calculated, where $u = u_{\mathrm{us}}/\cos\theta$ is the velocity component in the direction of the pipe axis and $z = \sin\theta z_{\mathrm{us}}$ is the perpendicular distance from the front wall of the flow channel. The mean velocity profile $\bar{u}(z)$ was calculated as the average of these 3000 individual profiles

$$\bar{u}(z) =< u(z,t) >, \tag{5.1}$$

where $<>$ denotes average over 3000 separate velocity profiles, *i.e.* average over time. The fluctuating velocity component was determined as the deviation of each individual velocity value from the mean velocity at a given position across the pipe:

$$\delta u(z,t) = u(z,t) - \bar{u}(z). \tag{5.2}$$

In order to characterize the turbulent state of the flow the local intensity of the velocity fluctuations is calculated as the correlation

$$I_T(z) =< \delta u(z,t)\delta u(z,t) > . \tag{5.3}$$

The individual velocity profiles given by the PUDV method suffer, however, from a noise intrinsic to the measuring principle. This noise contributes to the intensity given by Eq. (5.3), and for weak fluctuations it dominates the intensity totally obscuring the actual fluctuations of the flow. It appears however that one can eliminate the noise from the results by using spatial velocity correlations. To that end, the time averaged spatial pair correlation function of the measured velocity fluctuations is defined as

$$g(z,z') =< \delta u(z,t)\delta u(z',t) > . \tag{5.4}$$

This pair correlation function is shown in Fig. 5.2 for pine fibre suspension at consistency $c = 1.0\%$ and flow rate $Q = 1.3\,\mathrm{l/s}$ at the distance $0.5\,\mathrm{m}$ downstream from a turbulence generator (see Fig. 5.8). Since the intrinsic noise is highly uncorrelated, it only affects the values of correlation function near main diagonal. As an example, the fluctuations at the distance $z_0 = 20\,\mathrm{mm}$ from the front wall, that is at the pipe axis, are considered. A cross-section of the correlation of Fig. 5.2 is taken along the line $z + z' = 2z_0 = 40\,\mathrm{mm}$, this cut is shown in Fig. 5.3 with open markers as a function of coordinate $\delta z = z - z_0$. The shape of

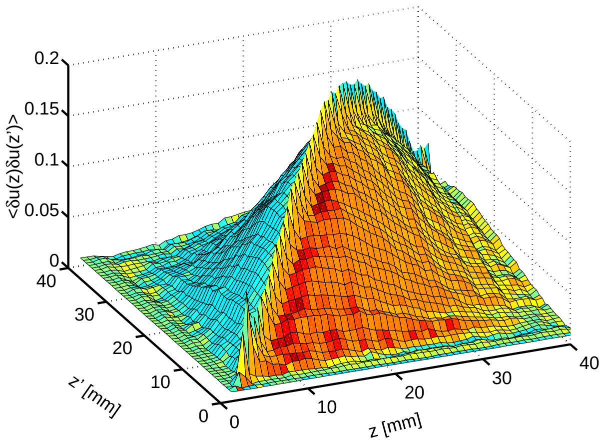

Figure 5.2: The spatial correlation function $< \delta u(z)\delta u(z') >$ of the fluctuating velocity component measured with the PUDV method for the pine fibre suspension at the consistency $c = 1.0\%$ and flow rate $Q = 1.3\,\mathrm{l/s}$ at the distance $0.5\,\mathrm{m}$ downstream from a sudden expansion with the area ratio 1:4. The intrinsic noise caused by PUDV-method is visible as a sharp ridge along the main diagonal.

the function $g(z_0 - \delta z, z_0 + \delta z)$ is almost Gaussian except for the center where there are a few points of large values due to the intrinsic noise. These points at the centre (in Fig. 5.3 the three points at the centre) are excluded and fit in the rest of the data a Gaussian function

$$f(\delta z) = I_0 \exp(-(\delta z/\lambda_{\delta u})^2) \tag{5.5}$$

The fitted Gaussian function is shown in Fig. 5.3 with solid line, and the fitted values of the Gaussian parameters are in this case $I_0 = 0.15$ and $\lambda_{\delta u} = 7\,\mathrm{mm}$. The parameter I_0 gives the corrected intensity for the velocity fluctuations at the point z_0, thus the local intensity of the velocity fluctuations is defined as

$$I_T(z_0) = I_0(z_0) \tag{5.6}$$

5.1.2 Laser-optical lubrication layer measurement

The thickness of the lubrication layer was measured optically using a collimated laser beam guided inside the acrylic flow channel (see Fig. 5.4). This method is quite analogous to that

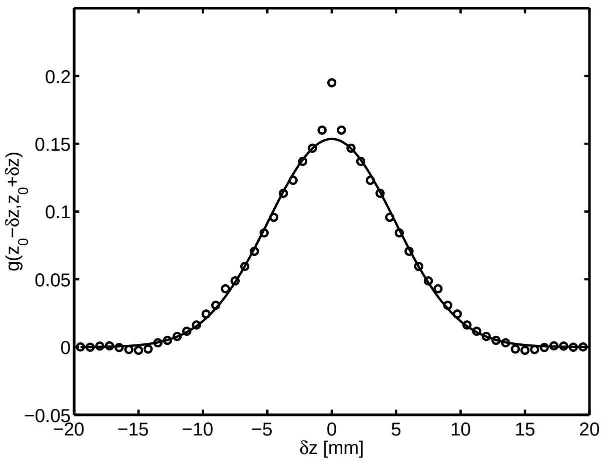

Figure 5.3: An example of the removal of the intrinsic noise. The cross-section of the original spatial correlation function in Fig. 5.2 along the line $z + z' = 20\,\mathrm{mm}$ is shown by the open markers, high values at the centre are due to intrinsic noise. The noise is removed by fitting a Gaussian function (solid line) to the original data excluding a few points at the centre. In this case the final value of the correlation at the center is 0.15.

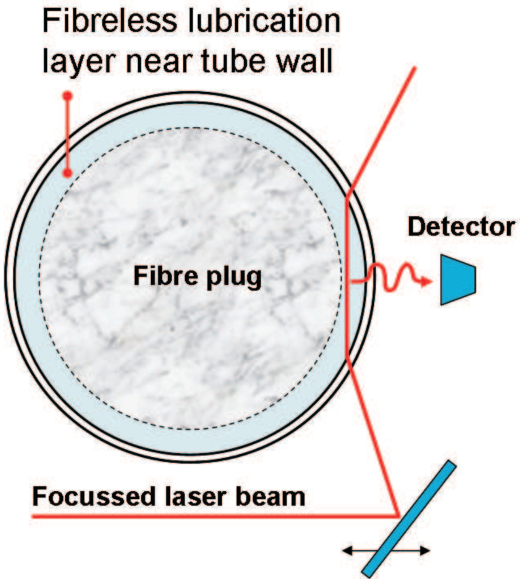

Figure 5.4: The principle of the laser-optical measurement of the lubrication layer thickness.

one used by Salmela[Sal97]. However, a few enhancement were included in the measurement setup used in the current study. First, the horizontal position of the vertical beam could be controlled so that the focal point remained at the horizontal pipe diameter. Second, the accuracy of the beam position as well as the diameter of the focal waist of the beam were approximately 10 μm, while in the setup used by Salmela the diameter of the focal waist was approximately 90 μm. The light scattered from fibres traversing the beam was detected by an optical sensor placed just outside the pipe wall, and having a narrow horizontal field of view through the pipe wall into the focal point of the beam.

The optical setup is shown in more detail in Fig. 5.5. The device was build as a separate optical table that has its own section of flow channel attached firmly to it. This section of flow channel is made of two semi-circular channels cut to separate acrylic prisms that are firmly bolted together to form a full circular flow channel. Only the front side prism was attached to the table while the rear prism stayed attached to the front part. This two-prism construction was chosen for two reasons. The first one is the possibility to drill the holes for the pressure taps starting from the inside of the channel wall while the prisms are detached. This way distortion of the channel wall next to the hole is reduced, which decreases velocity fluctuations near the holes and the error they generate in the loss measurement. The second advantage is the ability to replace the rear prism while keeping the front prism firmly attached to the table. This feature is utilized while calibrating the optical setup with a special device attached to a third prism that is used as a temporary rear prism during the calibration, see below.

The laser beam is generated with a 5 mW helium-neon laser (wave length $\lambda = 623\,\mathrm{nm}$), and guided via a mirror through an beam expander that increases the beam diameter from 1 mm to 10 mm. The expanded beam is collimated with a focussing lens ($f = 100\,\mathrm{mm}$) and guided by a mirror driven by a rotational stage into the flow channel. The positions of the mechanical stages were calculated using geometrical optics. At first the position of the lower linear stage and the rotation angle of the rotational stage were determined such that the central ray passed through the flow channel vertically at the desired distance from the wall. Next the position of the upper linear stage driving the collimating element was calculated from the condition that the point of focus is at the horizontal diameter of the flow channel.

The path of the laser beam is sensitive to various imperfections in the optical system. These imperfections include, *e.g.*, errors in the positions and alignment of both the optical elements (lenses, mirrors) and the mechanical stages driving those elements. In addition, various com-

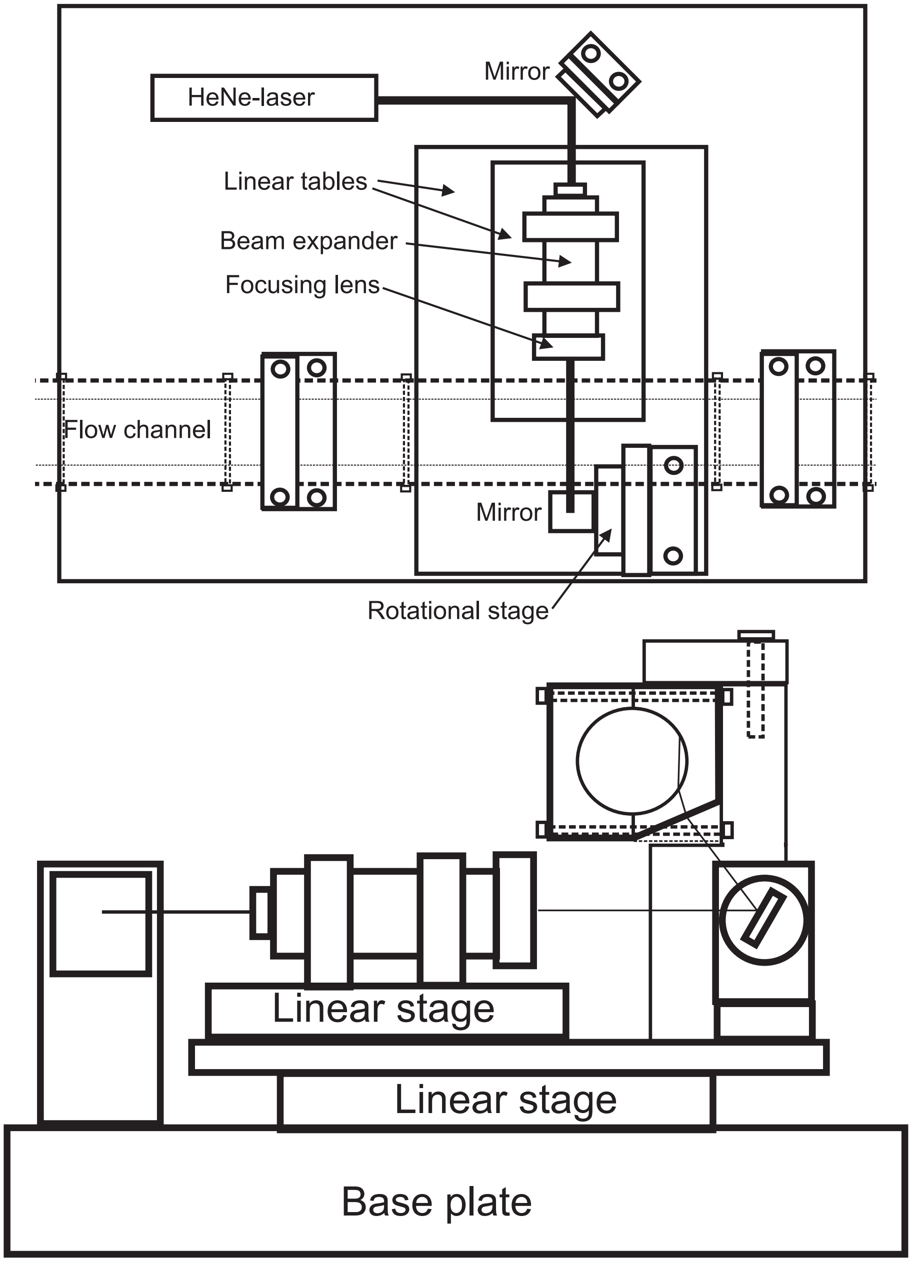

Figure 5.5: View of the laser-optical table from top (a) and side (b).

plications arise for very small values of the beam depth, since the angle of incidence of the laser beam entering the flow channel approaches that of total reflection as the depth of the beam goes to zero. Thus the positions calculated from geometrical optics can only be used as estimates for actual positions, and calibration of the optical setup is necessary.

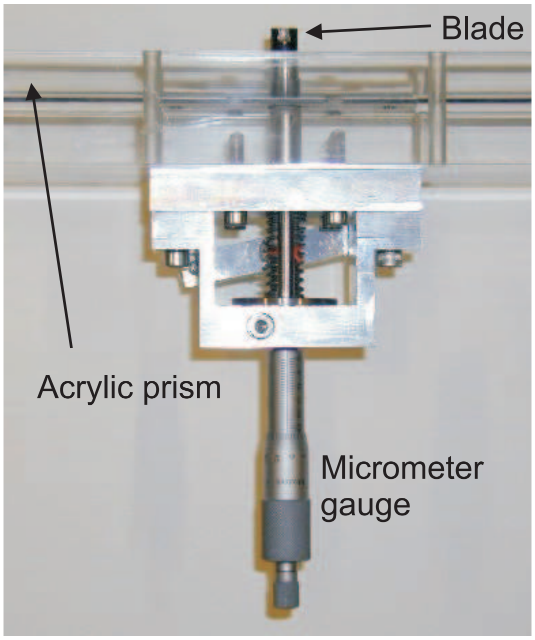

Figure 5.6: The device used for the calibration of the laser-optical setup.

A special calibration device was used to verify the exact depth of the laser beam as it is guided through the flow channel, see Fig. 5.6. A separate rear acrylic prism was used that had a hole in its side through which a rod with a light scattering blade at its tip was operated. The blade is driven along the horizontal diameter by the rod, which is attached to a manual micrometer gauge. During the calibration the flow channel was filled with clear water. For an initial value of distance from the pipe wall, the mechanical stages were driven to the positions given by the geometrical optics equations. The path of the laser beam was observed visually, and where necessary, tiny corrections to the positions of the mechanical stages were made to make the laser beam pass vertically through the flow channel. The beam was judged to pass the channel vertically when the bright spots visible at the points were the beam entered and left the flow channel were positioned symmetrically below and above the horizontal diameter. After the beam had a correct path, the edge of the calibration blade was driven close to the beam. As the blade was driven into the beam, the intensity of the light scattered by the blade increased from zero to some maximum value within a distance that was of the order of the beam width. The position of the half-value in this step was chosen to give the position of the beam. In the next phase the focal point of the laser beam was driven to the horizontal diameter of the pipe. In this process, the intensity of the light scattered from the blade was maximized by making small changes to the position of the linear stage driving the collimating element. After all necessary adjustments were made, the distance of the beam from the pipe wall was read from the micrometer gauge, and this value together with the positions of the mechanical stages were recorded. This procedure was repeated for distances $15 - 1270\,\mu$m from the wall with $10\,\mu$m steps.

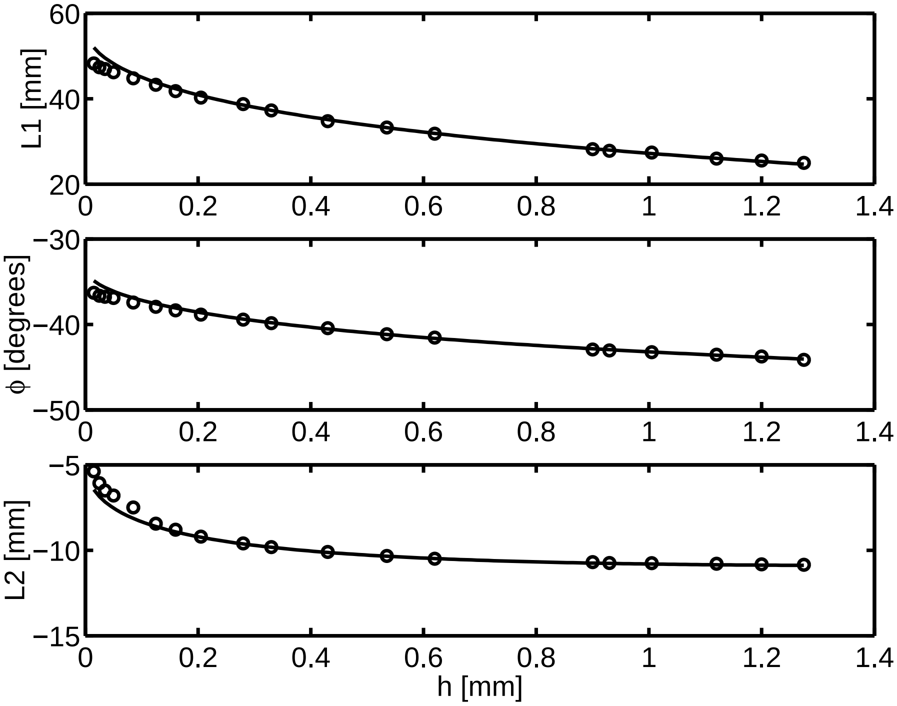

Figure 5.7: Calculated and calibrated positions vs. distance from the pipe wall for the base linear stage ($L1$), rotational stage (ϕ) and collimating stage ($L2$). Solid lines are calculated from geometrical optics, and the open markers are the calibrated positions.

The positions of the mechanical stages as functions of the beam distance from the wall are shown in Fig. 5.7. Solid lines are the positions calculated from geometrical optics, while the open markers are the values given by the calibration procedure. As can be seen, the values calculated from optical equations are quite accurate at the distances over 0.2 mm, but fail for shorter distances.

5.2 Measurements

The experimental work carried out in this study divides into three parts. First, pulsed ultrasound Doppler method was used to study the transient behaviour of the flow after a turbulence generator (sudden step), the approach to steady state flow, and the main features of fully developed flow. Secondly, the thickness of the lubrication layer was measured in a fully developed state with the laser-optical device. The properties of the fibres used in our experiments were also measured with a commercial fibre analyzer. Based on the measured properties, the threshold consistency is estimated above which a fibre plug may form.

5.2.1 Transient phenomena in developing flow

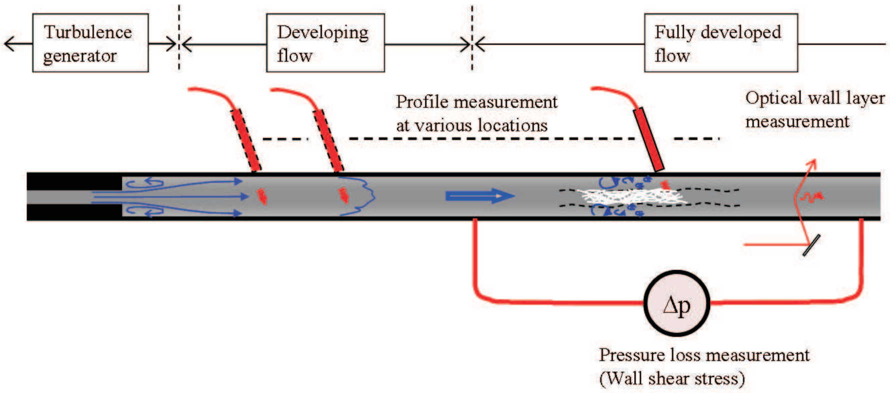

Figure 5.8: Schematic illustration of the experimental arrangement for fibre suspension flow in a straight pipe after a turbulence generator.

The PUDV -method was applied to study the flow in a straight pipe of diameter is $D = 40\,\mathrm{mm}$ and length $L = 3\,\mathrm{m}$ with a constriction block of inner diameter 20 mm and length 0.25 m placed inside the entrance part of the pipe, see Fig. 5.8. The resulting backward facing sudden step provided by the exit end of the constriction block generates a recirculation zone and a strong turbulent field in the downstream part of the pipe. The velocity and fluctuation profiles through the pipe diameter were measured at 18 fixed locations after the constriction block for different flow rates varied between 0.7 and 3.5 l/s. The first measuring point was located at distance 0.2 m and the last point at distance 2.6 m from the step. The measurement zone thus includes portion of the pipe, downstream of the recirculation zone, where the flow is already reattached to the pipe walls, takes place in a decaying turbulent field and approaches a fully developed condition towards the end of the pipe. In this experiment birch fibre suspension at consistency 1.0% was used.

Figures 5.9- 5.11 show the mean velocity and turbulent intensity profiles at various locations along the pipe for flow rates 0.7 l/s , 1.9 l/s and 3.5 l/s, respectively. The turbulent intensity is calculated from Eqs. (5.4)- (5.6). At all flow rates used, the turbulent intensity immediately after the sudden expansion is very high indicating that the suspension is in a fluidized state where the fibre phase is broken into small flocs that undergo turbulent motion. The turbulent intensity is highest in the middle of the pipe and decreases rapidly with distance x as the fluctuations of the fibre phase cease. At low flow rate (see Fig. 5.9), the fibre phase finally forms a continuous network that spans through the pipe, except of a thin fibre free lubrication layer that may be formed at the walls (but can not be observed with the PUDV techniques). The shape of the mean velocity profile undergoes only minor change along the pipe, being plug-like turbulent profile immediately after the recirculation zone and turning into a plug-like steady profile further downstream where the flow approaches fully developed condition. The developed profiles shown in Fig. 5.9 are typical to plug flow regime. At moderate flow rate (see Fig. 5.10) the behaviour is similar to that shown in Fig. 5.9. However, the overall turbulent intensity is higher and the high intensity region extends further downstream. In addition, the increased wall friction now prevents fibres from forming continuous network near the walls. Instead, a turbulent annulus remains near the walls and a continuous network is formed only at the core. This is seen as the turbulent intensity maxima near the walls and a slightly more rounded mean flow profile in the developed flow region. Here, the developed flow is typical to the mixed flow regime.

At the highest flow rate (see Fig. 5.11), the initial turbulent intensity is still higher and extends still further downstream. The turbulence induced by strong wall friction now prevents formation of continuous fibre network throughout the pipe. The suspension remains fully fluidized also in the developed flow and is thus in the turbulent flow regime. Although the mean velocity and turbulent intensity profiles in the developed flow region appear quite similar to those for ordinary turbulent flow of simple fluids, a closer examination of the mean velocity profile reveals marked differences to the conventional logarithmic law behaviour (see Sect. 6.1).

In this experiment a forward facing step was used to induce transient flow in decaying turbulence field and the resulting approach to fully developed flow. In practical applications, turbulent flow may be generated by other devices such as pumps, mixers and valves. One

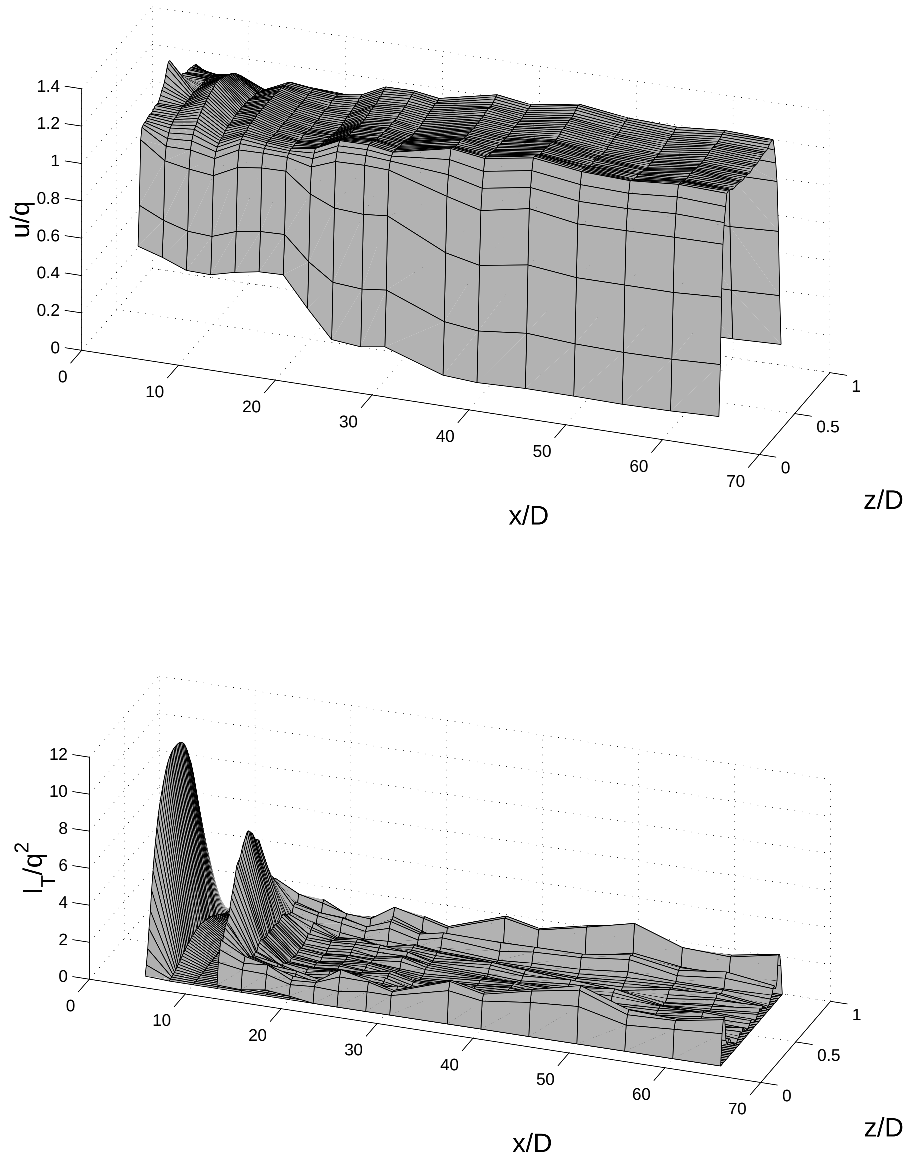

Figure 5.9: The measured mean velocity profile (top) and turbulent intensity profile (bottom) for birch fibre suspension at the consistency $c = 1.0\%$ (by weight) after the recirculation zone created by a sudden expansion with area ratio 1:4. Flow rate is $Q = 0.7\,\mathrm{l/s}$, and the corresponding Reynolds number calculated with the properties of water is $\mathrm{R}e_{\mathrm{w}} = 22000$. The insert in bottom figure shows the measured turbulent intensity multiplied by a factor 100 for clarity in the latter part of the pipe. Here, x is the downstream distance from the sudden expansion, z is the distance from the inner surface of the pipe wall along the horizontal pipe diameter, q is the average flow velocity, and D is the pipe diameter. The axis of the pipe is located at $z = 20\,\mathrm{mm}$.

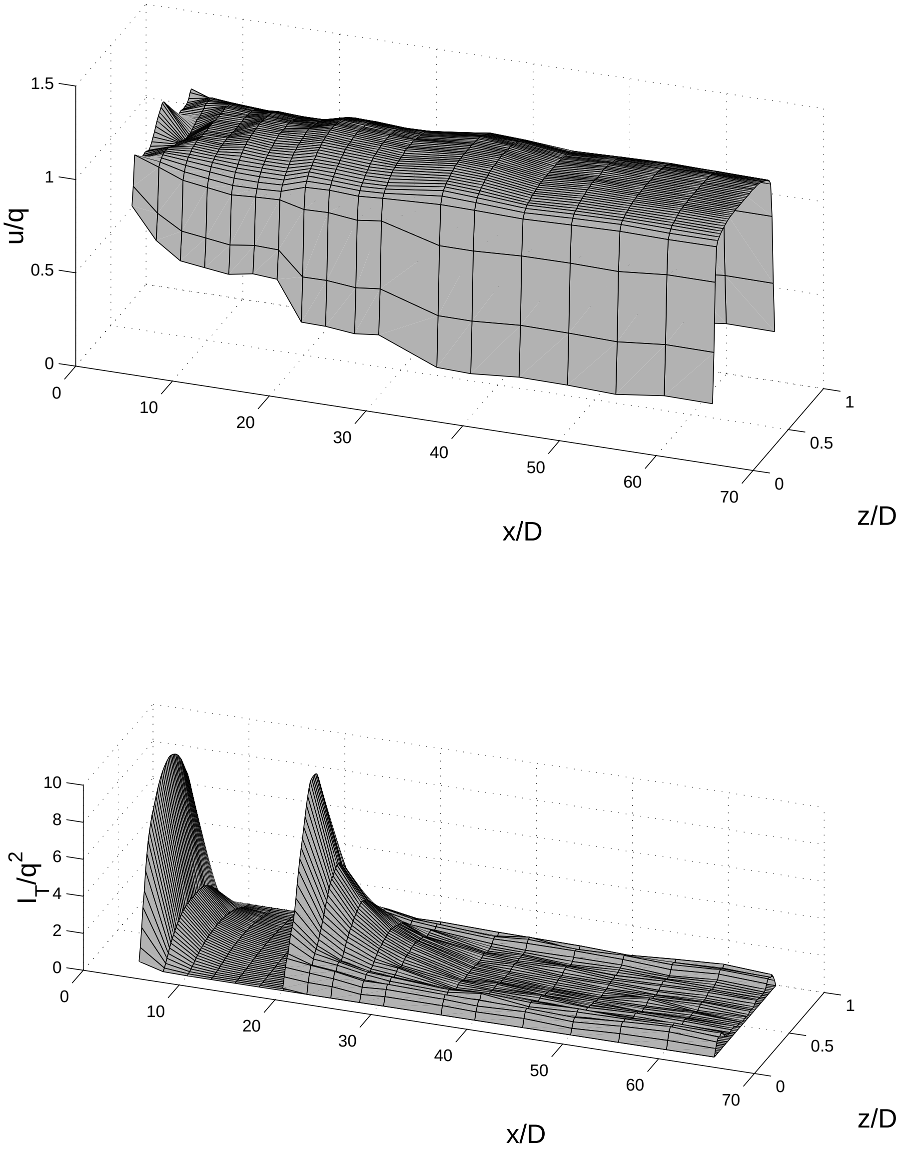

Figure 5.10: Same as Fig. 5.9 but for flow rate $Q = 1.9\,\mathrm{l/s}$, $\mathrm{R}e_\mathrm{w} = 60000$.

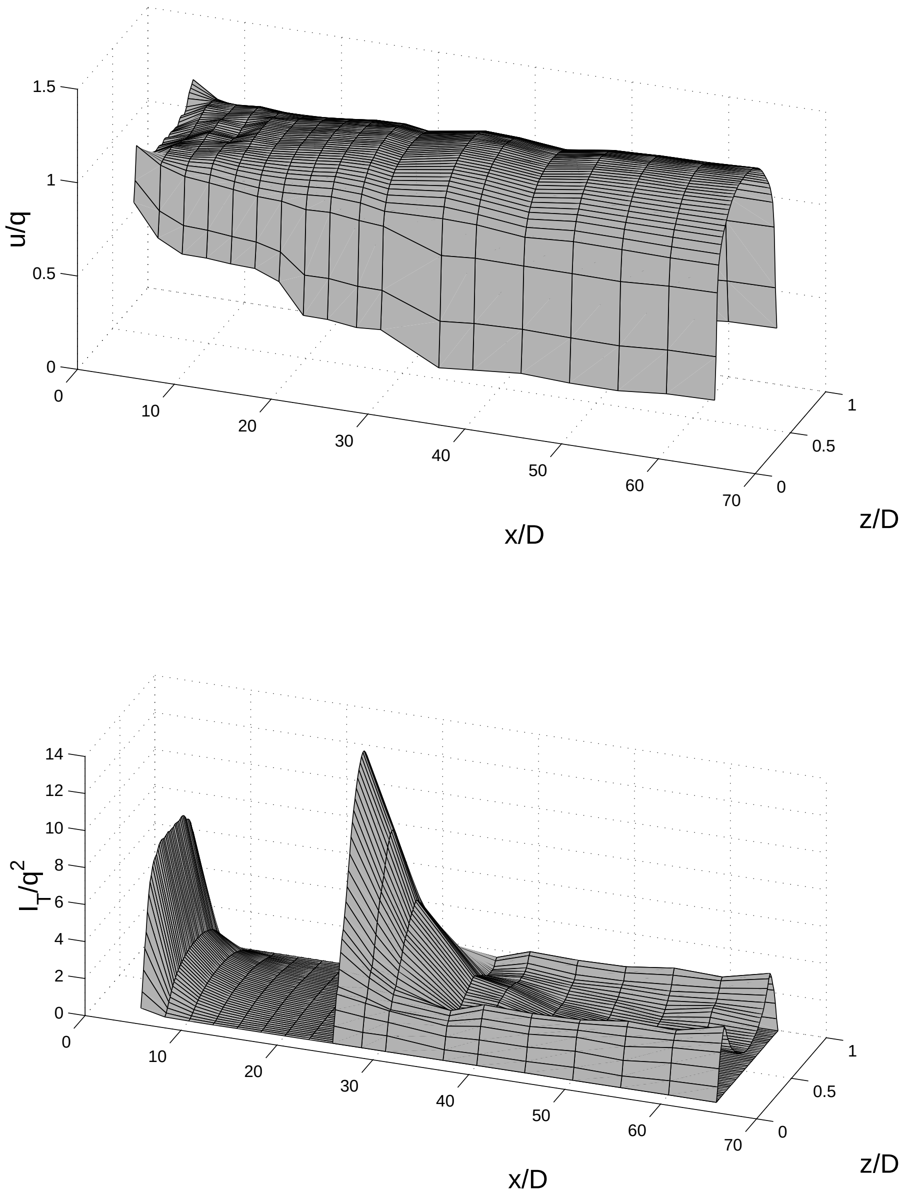

Figure 5.11: Same as Fig. 5.9 but for flow rate $Q = 3.5\,\mathrm{l/s}$, $\mathrm{R}e_\mathrm{w} = 110000$.

can, however, expect the qualitative features of the flow remain the same irrespective of the way in which the turbulence was generated.

5.2.2 Thickness of the lubrication layer

The thickness of the lubrication layer was measured in a fully developed flow with the laser-optical device described above. The straight pipe sections upstream and downstream of the measuring point were approximately 2.7 m and 0.5 m, respectively. For each flow rate, 10000 light intensity values were collected at a sampling rate adjusted according to the mean flow velocity such that the distance between consequent measuring points in the moving fibre plug was approximately 1 mm. Thus a length 10 m of the suspension flowing in the pipe was measured to give an adequate and statistically similar set of measurements for all flow rates. Notice that this method is applicable in the plug flow regimes, where the velocity of the fibre plug is very close to the measured mean velocity. The frictional loss in the pipe was measured simultaneously with the lubrication layer thickness.

Figure 5.12 shows an example of results obtained by the laser optical lubrication layer thickness measuring device discussed above. In the figure, shown is the mean intensity of scattered light as a function of the laser beam position inside the pipe of diameter 40 mm near the pipe wall. The measurement is for pine fibre suspension at consistency 0.5% and flow rates 0.14 l/s and 0.54 l/s, where the flow is well in the plug flow regime in both cases. The layer of pure water is indicated by a region next to the wall of nearly constant intensity. As the beam enters the fibre plug, the intensity starts to increase with the beam position more or less linearly. The thickness of the lubrication layer is defined as the crossing point of the two straight lines fitted to the data points in the constant intensity region and in the increasing intensity region as indicated in Fig. 5.12. In the flow condition shown, the thickness of the lubrication layer is thus estimated to be 0.037 mm at the flow rate 0.14 l/s and 0.38 mm at flow rate 0.54 l/s.

In Figs. 5.13 and 5.14 shown are the measured values of layer thickness as a function of mean flow velocity for various consistencies. The measured layer thickness is shown only for those flow velocities at which a well defined finite thickness value could be found. Especially with the present measuring techniques, the lubrication layer could not be observed at very low flow rates. It appears that in each case, the regime where the lubrication layer was not found coincides with the low flow rate domain where the loss increases with flow rate. This domain

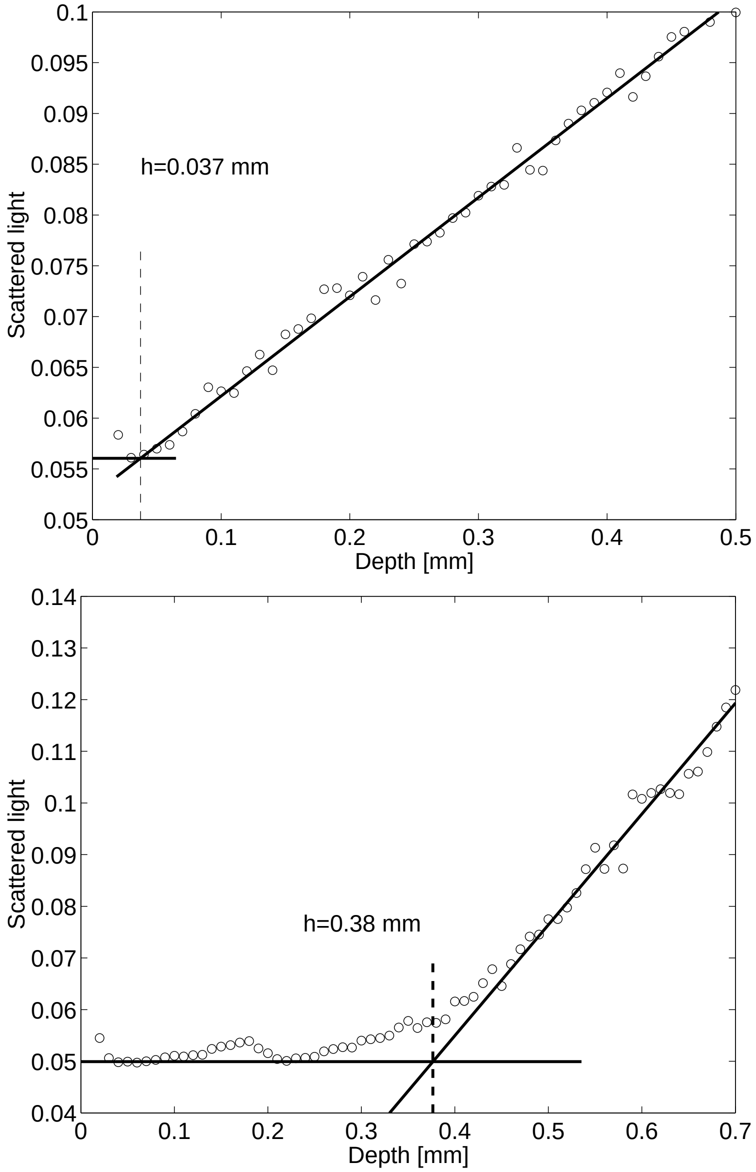

Figure 5.12: The measured intensity of the laser light scattered by fibres as a function of distance from the pipe wall at flow rates $Q = 0.14\,\mathrm{l/s}$ (top) and $Q = 0.54\,\mathrm{l/s}$ (bottom). For each flow rate, the crossing point of two fitted lines defines the thickness of the fibre free lubrication layer.

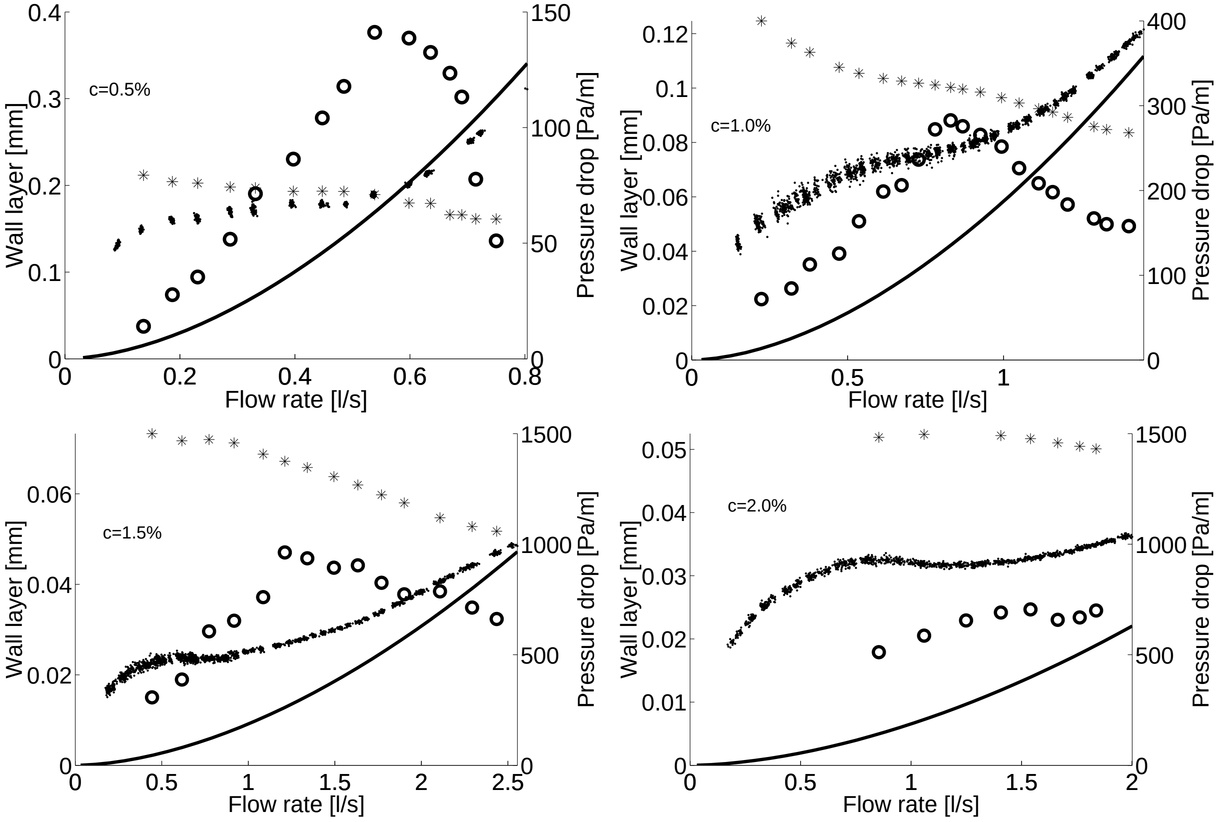

Figure 5.13: Measured pressure drop (small dots) and wall layer thickness (open circles) versus flow rate for pine suspension at consistencies 0.5% – 2.0% (by weight). Solid line is the pressure drop of water calculated using Eq. (4.4), and stars give the thickness of the viscous sublayer ($y^+ = 5$) for water at each value of loss.

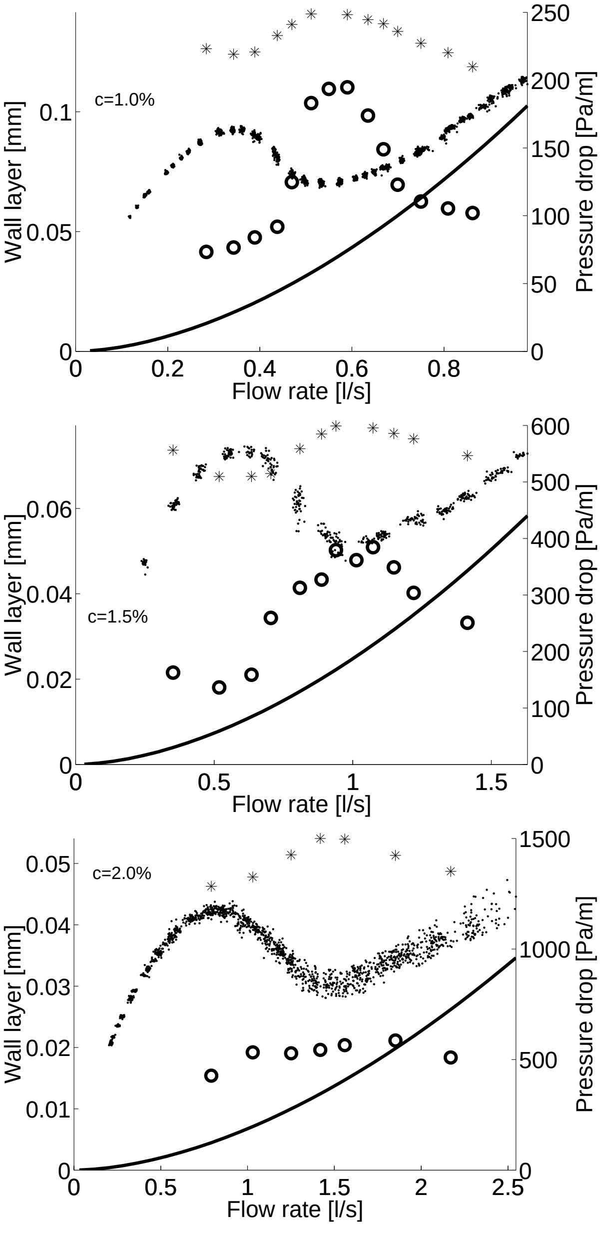

Figure 5.14: As Fig. 5.13, but for birch suspension at consistencies 1.0% – 2.0% (by weight).

is naturally identified as the plug flow regime with direct fibre-wall contact. An observable lubrication layer appears at the flow rate corresponding to the local maximum in the loss curve (birch) or to the point where the loss curve levels off (pine). Above that flow rate, the measured value of the lubrication layer thickness first grows with flow rate, reaches a maximum and then starts to decrease. In general, the thickness decreases with consistency and the location of maximum point becomes less definite. The flow rate corresponding to the maximum layer thickness (where observable in the data) falls approximately at the same point, where the loss curve again starts to grow. This domain is identified as the plug flow regime with lubrication layer. The observed decrease of the layer thickness after the maximum is most likely due to incipient turbulence, *i.e.* turbulence in the fluid phase (that was not observed with the present methods). This turbulence is not yet strong enough to cause macroscopic breakage of the fibre network, but only to bend and dislodge individual fibres that are loosely bound to the fibre plug surface. These fibres can then be randomly displaced towards the pipe wall by fluctuations of fluid velocity, and thereby cause increased light scattering as they traverse the laser beam. The apparent decrease of lubrication layer thickness may thus be explained by dispersion of the fibre plug surface layer due to fluid phase turbulence. In this region the measured lubrication layer thickness decreases and pressure loss increases but macroscopic rupture of fibre plug is not yet observed.

5.3 Flow regimes of wood fibre suspension in a straight pipe

Based on the experimental results discussed above, the main qualitative features of flow of wood fibre suspensions in straight pipe are now summarized. Direct observation using various experimental methods suggests that one can divide the flow into five different regimes according to flow rate. These regimes are shown in Fig. 5.15, where the measured loss curves as a function of flow rate for pine fibre suspension at different consistencies are plotted. Figure 5.16 illustrates the five qualitatively different flow regimes discussed below. The numbering coincides with that shown in the context of loss data, Fig. 5.15. Below, the relevant phenomena taking place in each of these regimes will be shortly discussed.

Regime I: plug flow with wall contact

In this regime the intensity of turbulence is high immediately after the source (constriction, pump, *etc.*), and the suspension is in a fluidized state where the fibre phase is broken into flocs. The intensity of the turbulence decays rapidly downstream from the source, and the fibre phase forms into a continuous network. In this process, the turbulent energy of fibres is partly captured as the elastic energy of the network. This elastic energy manifests itself as an elastic force that pushes fibres towards the pipe wall. Notice that the quantitative details of this elastic force may depend on the initial turbulent intensity and the way the turbulence decays, *i.e.* the history of the suspension. The inertial lift force, on the other hand, repels fibres from the wall. In this regime of low flow velocity, the elastic force is, however, large enough to keep the fibre plug in a contact with the wall. Thus the fibre network forms into a state that spans through the pipe, and no observable lubrication layer is found. The radial force balance of the fibre plug is maintained between the elastic force, the lift force, and a support force by the wall. The support force give rise to mechanical friction between the fibre plug and the pipe wall, increasing the loss.

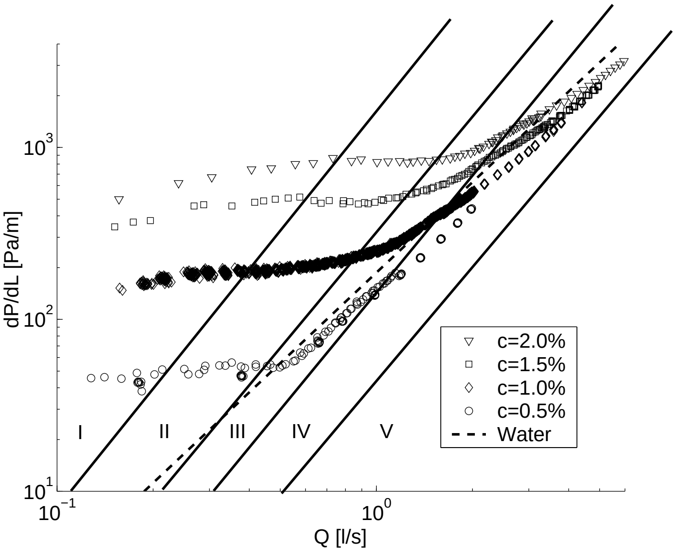

Figure 5.15: Measured loss vs. flow rate for pine fibre suspension in a $D = 40\,\mathrm{mm}$ flow channel for various consistencies (by weight). Dashed line is the standard curve for pure water in a hydraulically smooth pipe, and solid lines divide the flow domain into five main regimes (labeled I - V) based on the flow behaviour (see Fig. 5.16)

Regime II: plug flow with lubrication layer

This regime is quite similar to the regime I, with the exception that the lift force is large enough to keep the fibres away from the pipe wall, on the average. Thus the fibre network

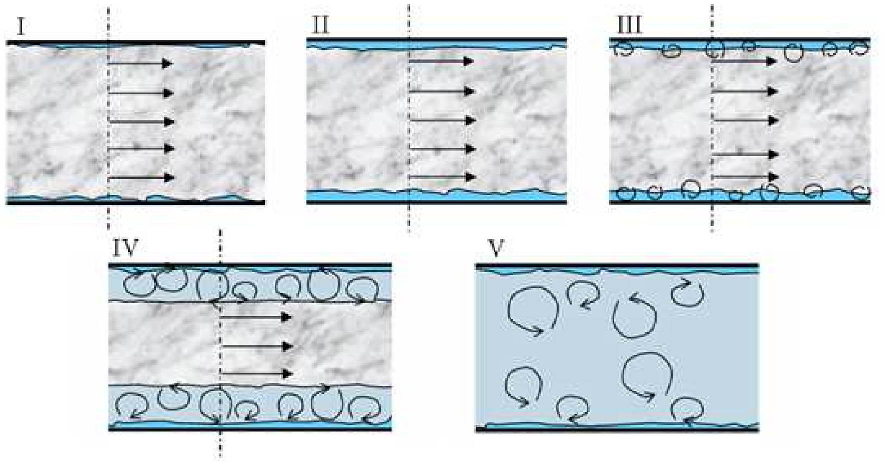

Figure 5.16: The main regimes of fully developed flow of fibre suspensions. (I) Plug flow regime with direct fibre-wall contact, (II) plug flow regime with lubrication layer, (III) plug flow regime with incipient (fluid phase) turbulence, (IV) mixed flow regime and (V) fully turbulent flow regime

forms into a state where there is a fibreless lubrication layer next to the pipe wall. The thickness of this layer increases with flow rate. Due to the lubrication layer, the loss saturates of may even decrease with increasing flow rate.

Regime III: plug flow with smearing annulus

In this regime the loss increases approximately linearly with flow rate, and the behaviour of the lubrication layer thickness is ambiguous. Fluctuations in the fluid phase (incipient turbulence) deform and disengage individual fibres on the surface of the fibre plug. These fibres are randomly displaced towards the wall into the lubrication layer by the fluctuations in the fluid velocity, which eventually renders the lubrication layer unobservable.

Regime IV: Mixed flow

In this regime the dependence on the flow rate of the loss is approximately quadratic. The turbulence induced by the high flow velocity and the strong wall friction prevents fibres from forming a continuous network near the walls. Thus the fibre plug is only formed at the core and a turbulent annulus remains at the walls.

Regime V: Full turbulence

In this regime the turbulence created by strong wall friction prevents the formation of the fibre plug throughout the pipe, and the suspensions remains in a fluidized state. The transition from mixed flow regime IV into fully turbulent regime V is gradual and no sharp change in loss behaviour can be observed. The dependence on the flow rate of the loss remains close to quadratic in the transition, thus the exact flow rate at which the fibre plug core disappears can not be identified from loss data. This topic will be discussed in greater detail in Sect. 6.1 utilizing the results from velocity profile measurements. At very high flow rates, the loss behaviour approaches that of pure carrier fluid.

Although the classification discussed above and depicted in Figs. 5.15 and 5.16 is very similar to those presented previously (see *e.g.* Ref. [Duf97]), there are some subtle differences. In particular, the existence and nature of regime III and identification of the different flow regimes in the loss data are now more precisely defined. Notice also, that the present classification is based on direct experimental evidence on various features of the flow.

The results reported in this chapter may not seem to add much to the qualitative understanding of the developing flow of fibre suspension in decaying turbulence. They do, however, indicate that the new experimental method utilized here can be used to gain much more detailed information on the flow behaviour as has been previously possible. Based on already these results, even the qualitative behaviour of the pipe flow can be further specified at least in two respects. Firstly, unlike often phrased, for a pipe flow in mixed or turbulent flow regions (after a pump, say) the wall friction does *not* break the continuous fibre network. Instead, wall friction prevents such a network from ever forming within an annulus of some thickness or in the entire pipe. (Actual breaking of fibre network would only take place if the flow was first stopped to allow the continuous network to form, and then resumed.) Even though this difference may appear quite superficial, it can have some significance, *e.g.*, when using the measured values of disruptive shear stress of the fibre network in predicting pipe flow behaviour. It is not clear, without further investigation, that the value of disruptive shear stress measured by actually breaking an existing network by applied shear stress is the proper value to be used, *e.g.*, in predicting the transition from plug flow to mixed and turbulent flow regions in conventional pipe flows. Secondly, the appearance of the fibre free lubrication layer in the plug flow regime is often explained by mechanical models based on shear deformation of the network induced by the wall stress, and the resulting reduction of plug diameter [MDT71]. For a pipe flow brought about by a pump, such a model is unphysical simply because the undeformed state of the network never existed. Instead, the fibre plug formes from the fluidized state in decaying turbulence after a pump or any fluidizing device is originally of diameter slightly less than that of the pipe. The existence of lubrication layer is more likely due to inertial lift force that acts on particles moving near the wall. This phenomenon leads to a tubular pinch effect where the fibres are repelled from the wall and the fibre plug is formed in a state where the lift force is balanced by the elastic force of the network. The elastic force, in turn, is affected by the turbulent energy of fibres, partially stored as the elastic energy of the forming network.

In the next chapter this qualitative depiction of the flow behaviour will be utilized in a more detailed theoretical and semiempirical analysis of the flow dynamics. This analysis, in turn, is then used in deriving new physically justified loss correlation formulas for the flow of wood fibre suspension in straight, smooth pipes.

Chapter 6

Velocity profiles and loss correlation

In this chapter correlations for frictional losses of wood fibre suspension flow in a straight pipe are derived. These correlations cover a large range of flow rates from the plug-flow regimes to the fully turbulent regime. The approach used here is based on detailed information on flow profiles and is thus analogous to that used to derive the conventional loss correlations of Newtonian liquids. In the plug-flow regimes, the velocity profile is found by analytically solving a set of two-phase equations of the flow, while in the mixed and turbulent regimes a suitable parameterization of the measured profiles discussed in Chapter 5 is utilized. The loss correlations are then found by integrating these velocity profiles over the cross section of the pipe.

6.1 Velocity profiles in the plug flow regimes

In the plug-flow regimes all the relevant phenomena take place in a very narrow annulus next to the pipe wall. Typically the width of this annulus is less than 1 mm, *i.e.* below the spatial resolution of the pulsed ultrasound Doppler device used to measure the velocity profiles. On the other hand, flow is non-turbulent and one can resort to modeling of the flow field. Based on earlier knowledge and the experimental results presented in this monograph, a novel approach to the dynamics of the lubrication layer was introduced (see chapter 5). Here a simple two-phase model for closed-channel flow of wood-fibre suspension in this regime is considered. This model includes all the dynamical features of the flow discussed in chapter

5 for the plug-flow regimes. The model is based on the averaged flow equations that were derived in chapter 2, and it will be presented in a closed form ready for solution. In the model, the lubrication layer is modeled as a response to the inertial transverse lift force acting on the fibres near the pipe wall. The form of the lift force used in the model is qualitatively supported by the numerical simulations described in sections 3.3 and 3.4.

Thus the plug-flow regimes I and II shown in Fig. 5.16 are considered, and a laminar two-phase flow model for the regimes is derived. The model takes into account the direct contact friction between fibres and pipe wall at low flow rates and existence of lubrication layer at higher flow rates (see Fig. 6.1). The lubrication layer is formed due to repulsive inertial lift force that is known to act on fibres moving near the wall. The averaged fluid flow is assumed to be steady and fully developed, *i.e.* fluid velocity is longitudinal

$$\mathbf{u}_\mathrm{f} = u_\mathrm{f}(r)\hat{\mathbf{e}}_z. \tag{6.1}$$

Fibres move as a rigid plug with a constant velocity

$$\mathbf{u}_\mathrm{s} = u_\mathrm{s}\hat{\mathbf{e}}_z. \tag{6.2}$$

At very low flow rates the fibre plug is indirect contact with the pipe wall. As the flow rate increases, a lubrication layer of pure carrier fluid occurs next to the pipe wall. The width of the lubrication layer is small compared to the pipe radius. In the case where lubrication layer exists, the velocity of the fluid within the thin layer is given approximately by the linear profile

$$\mathbf{u}_\mathrm{f}(r) = -\frac{R}{\mu_\mathrm{f}}\frac{\partial \tilde{p}_\mathrm{f}}{\partial z}(R-r) = \frac{\tau_w}{\mu_\mathrm{f}}y \tag{6.3}$$

where r and z are the radial and axial coordinates, respectively, μ_f is the dynamic viscosity of the fluid, $\tilde{p}_\mathrm{f}$ is the fluid pressure, R is the radius of the pipe, y is the distance from the wall and τ_w is the wall shear stress. The fluid velocity at the surface of the fibre plug is thus given by

$$u_0 = \frac{\tau_w}{\mu_\mathrm{f}}h, \tag{6.4}$$

where h is the thickness of the lubrication layer.

Inside the fibre core, the system is modeled as two interacting continua, and the governing two-phase equations for momentum are obtained by (volume) averaging the corresponding equation for each phase. The flow inside the core is described by the equations that have

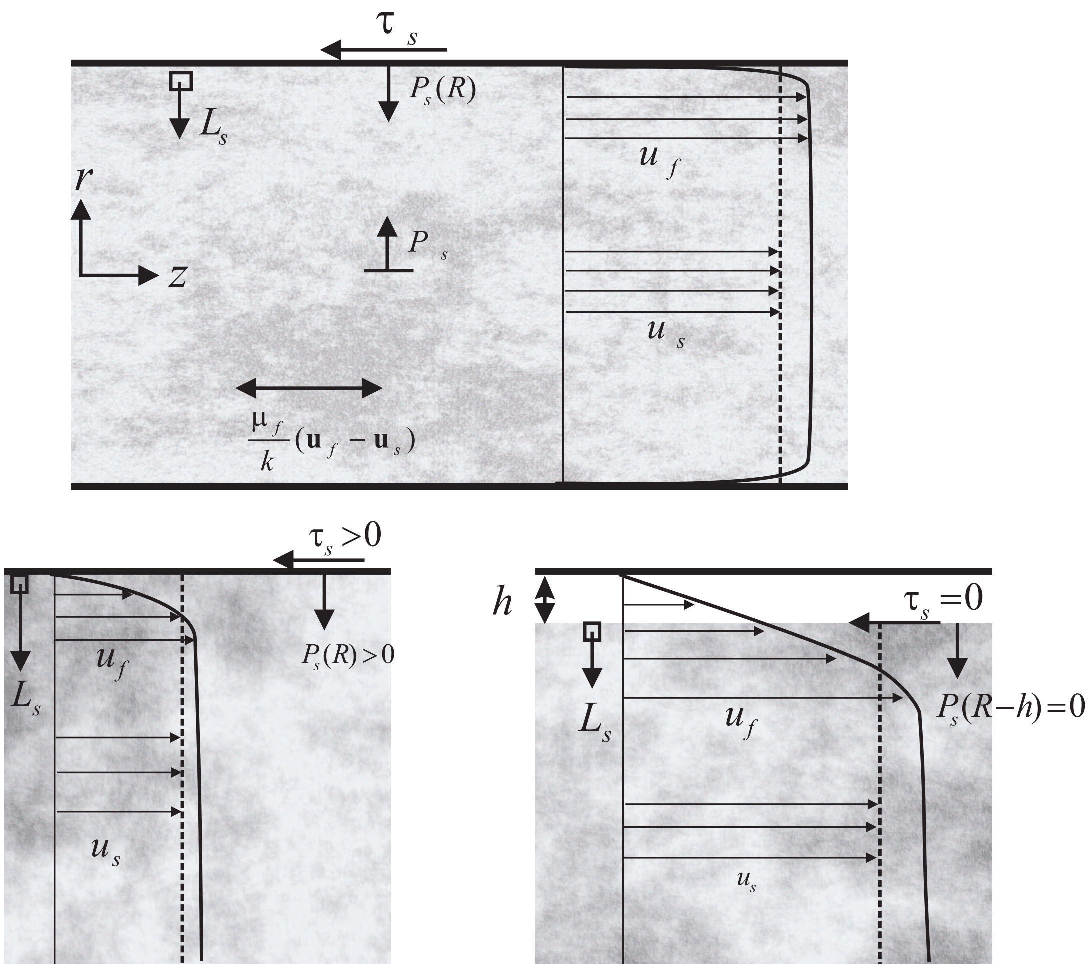

Figure 6.1: Schematic view of the plug flow of fibre suspension. A close up view at the wall with the fibre plug in a contact with the wall (bottom left) and with a lubrication layer (bottom right).

been derived in section 2.3.2. The porosity of the fibre plug ϕ is assumed to be constant, hence the equations for the conservation of mass, Eqs. (2.59) and (2.60), are satisfied for the longitudinal flow field of Eqs. (6.1) and (6.2). The conservation of momentum is described by Eqs. (2.70) and (2.62), namely

$$\begin{aligned} \phi \nabla \tilde{p}_{\mathrm{f}} &= \nabla \cdot \langle \tau_{\mathrm{f}} \rangle - \frac{\mu_{\mathrm{f}}}{k}(\bar{\mathbf{u}}_{\mathrm{f}} - \bar{\mathbf{u}}_{\mathrm{s}}) - L_{\mathrm{s}} \hat{\mathbf{e}}_r && (6.5) \\ -\nabla \cdot \langle \sigma_{\mathrm{s}} \rangle &= +\frac{\mu_{\mathrm{f}}}{k}(\bar{\mathbf{u}}_{\mathrm{f}} - \bar{\mathbf{u}}_{\mathrm{s}}) + L_{\mathrm{s}} \hat{\mathbf{e}}_r. && (6.6) \end{aligned}$$

were L_{s} is the lift force applied on the unit volume of the fibre plug by the carrier fluid. It is assumed in Eqs. (6.5) and (6.6) that the effect of gravity can be neglected. The average stress tensor of the fluid phase given by Eq. (2.68) simplifies in the current case in the form

$$\langle \tau_{\mathrm{f}} \rangle = \phi \mu_{\mathrm{f}} \left((\nabla \bar{\mathbf{u}}_{\mathrm{f}}) + (\nabla \bar{\mathbf{u}}_{\mathrm{f}})^{\mathrm{T}} \right). \tag{6.7}$$

The longitudinal component of the equation for the carrier fluid, Eq. (6.5), can be written in the form

$$-\phi \frac{\partial \tilde{p}_{\mathrm{f}}}{\partial z} + \phi \mu_{\mathrm{f}} \left(\frac{\mathrm{d}^2}{\mathrm{d}r^2} u_{\mathrm{f}} + \frac{1}{r} \frac{\mathrm{d}}{\mathrm{d}r} u_{\mathrm{f}} \right) - \frac{\mu_{\mathrm{f}}}{k}(u_{\mathrm{f}} - u_{\mathrm{s}}) = 0. \tag{6.8}$$

The proper boundary conditions for this equation are the velocity at the plug surface given by Eq. (6.4), and zero velocity gradient at the pipe axis. With these boundary conditions, the exact solution of Eq. (6.8) is

$$u_{\mathrm{f}}(r) = u_{\mathrm{f0}} \left[1 - \frac{I_0(r^*)}{I_0(R^*)} \right] + u_0, \tag{6.9}$$

where

$$u_{\mathrm{f0}} = u_{\mathrm{s}} - u_0 - \frac{\phi k}{\mu_{\mathrm{f}}} \frac{\partial \tilde{p}_{\mathrm{f}}}{\partial z}, \tag{6.10}$$

$I_0(x)$ is the modified Bessel function of the first kind of order zero, $r^* = r/\sqrt{\phi k}$ is a dimensionless radial coordinate, and $R^* = (R - h)/\sqrt{\phi k}$ is a dimensionless plug radius.

The length scale $\sqrt{\phi k}$ of the velocity profile is typically of the order of 10^{-3} m to 10^{-5} m so that the arguments of the Bessel functions in Eq. (6.9) are large. The velocity profile can thus be approximated by an exponential function

$$u_{\mathrm{f}}(r) = u_{\mathrm{f0}} \left[1 - \exp(-y^*) \right] + u_0, \tag{6.11}$$

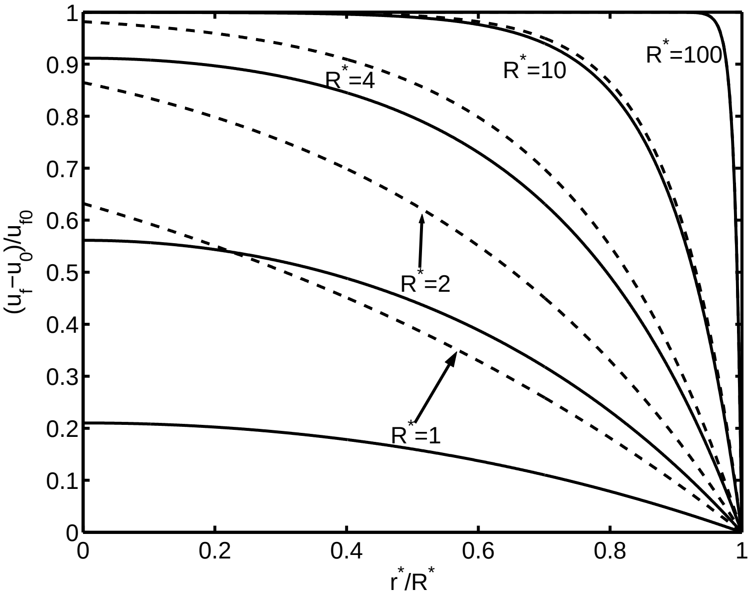

Figure 6.2: The calculated scaled velocity profiles for various values of dimensionless plug radius R^*. Solid lines are the exact solutions given by Eq. (6.9), while dashed lines show the approximations given by Eq. (6.11).

where $y^* = R^* - r^*$ is the nondimensional distance from the plug surface. The reduced flow velocity $(u_\mathrm{f} - u_0)/u_\mathrm{f0}$ is shown in Fig. 6.2 as a function of nondimensional radial distance $r^*/R^* = r/(R-h)$ for selected values of R^* in the range 1-100. The difference between the exact solution and the approximation is large with small nondimensional plug radius, but decreases with increasing radius (decreasing permeability). The relative difference is below 2% for $R^* = 10$, and for $R^* = 100$ the absolute difference is below the line thickness of the graph.

The velocity of the fibre plug can be solved from the condition that the sum of the forces acting on the plug is zero in the steady state. The forces acting on the plug can be identified by integrating the longitudinal component of the momentum equation (6.6) over the cross-section of the fibre core. The resulting equation manifests a balance between two forces, namely the total Darcy's drag applied by the carrier fluid and the extra mechanical friction with the pipe wall (present in the case where lubrication layer does not exist, *i.e.* $h = 0$). Darcy's drag can be obtained by integrating the velocity profile for the carrier fluid, Eq. (6.11). Combining these two results and replacing wall shear stress for pressure gradient yields the plug velocity in a form

$$u_{\mathrm{s}} = \frac{1}{\mu_{\mathrm{f}}}\sqrt{\frac{k}{\phi}}\left((1-\frac{h}{R})\tau_w - \tau_{\mathrm{s}}\right) - \frac{2\phi k}{\mu_{\mathrm{f}} R}\tau_w + u_0. \tag{6.12}$$

Here the shear stress at the plug surface τ_{s} is the (yet unknown) mechanical wall friction per unit area. Finally, combining Eqs. (6.11) and (6.12) gives the velocity profile of the carrier fluid in the form

$$u_{\mathrm{f}}(r) = \frac{1}{\mu_{\mathrm{f}}}\sqrt{\frac{k}{\phi}}\left((1-\frac{h}{R})\tau_w - \tau_{\mathrm{s}}\right)\left[1-\exp(-\frac{y}{\sqrt{\phi k}})\right] + u_0, \tag{6.13}$$

where u_0 is given by Eq. (6.4).

Notice that equations (6.12) and (6.13) are valid for both plug-flow regimes I and II shown in Fig. 5.16, and even for the percolating regime, where the fibre plug is stagnant and only fluid flow occurs. It now remains to develop an appropriate model for the shear stress at the plug surface τ_s and for the thickness of the lubrication layer h. Clearly, τ_s must depend on the radial structural stress of the fibre network at pipe wall. Thus the radial stress balance equation of the fibre plug is considered, *i.e.* the radial component of Eq. (6.6)

$$-\frac{\partial}{\partial r}P_{\mathrm{s}} + L_{\mathrm{s}} = 0. \tag{6.14}$$

Here, $L_{\mathrm{s}}(\leq 0)$ is the inertial lift force per unit volume acting on the fibres and P_{s} is the radial normal stress of the fibre network. In what follows it will be called simply the structural stress. (Notice that the structural stress arises originally from turbulent energy partially converted into elastic energy of the network that forms in the decaying turbulent flow field). According to the numerical results presented in Chapter 3, the lift force decays rapidly with the distance from the wall - typically within a few particle diameters. Notice that the length scale associated with this decay is not known in the current case. It may be, *e.g.*, the average fibre length or the surface roughness of the fibre plug rather than the fibre radius.

Since the length scale associated with the lift force is not known, a global balance equation for the structural stress of the fibre network is considered instead. Integration of Eq. (6.14) gives the structural stress at the surface of the fibre plug

$$P_{\mathrm{s}}(R-h) = P_{\mathrm{s}}(0)|_h + \int_0^{R-h} L_{\mathrm{s}}\, dr = P_{\mathrm{s}}(0)|_h - P_{\mathrm{L}} \tag{6.15}$$

where $P_{\mathrm{s}}(0)|_h$ is the structural stress at the centre of the pipe. (The notation is chosen to emphasize that the stress in the centre may depend on the lubrication layer thickness h.) The quantity $P_{\mathrm{L}}(\geq 0)$ gives the integrated contribution of lift force on structural stress and depends on flow rate. The integrated lift force is chosen to be modeled as

$$P_{\mathrm{L}} = \frac{1}{2}\rho_{\mathrm{f}} u_{\mathrm{s}}^2 C_{\mathrm{L}}, \tag{6.16}$$

where ρ_{f} is the density of the carrier fluid, C_{L} is the lift force coefficient and $\mathrm{R}e_{\mathrm{s}} = \rho_{\mathrm{f}} u_{\mathrm{s}} \sqrt{k}/\mu_{\mathrm{f}}$ is the fibre-network Reynolds number.

At low values of flow rate, fibres are in contact with the wall ($h = 0$) and the structural stress at the surface of the fibre plug is positive, *i.e.* $P_{\mathrm{s}}(R) > 0$. The radial force balance is then maintained between structural stress, lift force and the support force by the wall. The latter is proportional to P_{s} and automatically adjusts itself so that there is no macroscopic deformation of the plug. Consequently, the structural stress at the centre of the plug is constant; $P_{\mathrm{s}}(0)|_{h=0} \equiv P_{\mathrm{s}0}$. Furthermore, it is assumed that the mechanical friction stress is then proportional to $P_{\mathrm{s}}(R)$:

$$\tau_{\mathrm{s}} = C_{\mathrm{s}} P_{\mathrm{s}}(R) = C_{\mathrm{s}}\left(P_{\mathrm{s}0} - P_{\mathrm{L}}\right), \tag{6.17}$$

where C_{s} is a friction coefficient. As the flow rate is increased, P_{L} increases, and $P_{\mathrm{s}}(R)$ and τ_{s} decrease and eventually become zero. As the flow rate is increased beyond this point, lubrication layer develops. Consequently, fibre consistency and structural pressure well inside the plug increase by a small but finite amount. The structural pressure at the plug boundary $P_{\mathrm{s}}(R-h)$ vanishes for all $h > 0$. The excess stress ΔP_{s} at pipe centre for a finite value of lubrication layer thickness h is now defined by

$$P_{\mathrm{s}}(0)|_h = P_{\mathrm{s}0} + \Delta P_{\mathrm{s}}(h). \tag{6.18}$$

For small values of h, it is postulated that $\Delta P_{\mathrm{s}} = \frac{1}{\Gamma}h$ where Γ is a constant. This relation gives a natural constitutive model for lubrication layer thickness, namely

$$h = \Gamma \Delta P_{\mathrm{s}} = \Gamma (P_{\mathrm{s}}(0)|_h - P_{\mathrm{s0}}) = \Gamma (P_{\mathrm{L}} - P_{\mathrm{s0}}), \tag{6.19}$$

where the latter equality follows from Eq. (6.15) since $P_{\mathrm{s}}(R-h) = 0$. Reorganizing the equations given above, one can now rewrite the final results for frictional stress and lubrication layer thickness in a compact form as

$$\begin{cases} \tau_{\mathrm{s}} = \max(0, C_{\mathrm{s}}(P_{\mathrm{s0}} - P_{\mathrm{L}})) \\ h = \max(0, \Gamma(P_{\mathrm{L}} - P_{\mathrm{s0}})) \end{cases} \tag{6.20}$$

Notice that the constants P_{s0} and Γ, related to elastic stress in the fibre plug as $h = 0$ and to rate of change of that stress with respect to h, may depend on flow conditions and not only on fibre properties. In particular, they may depend on the initial turbulent intensity and on the details of turbulence decay and formation of the fibre plug in the developing flow region downstream of the turbulence generator (see Sect. 5.2.1).

There is still some degeneracy in this set of parameters, and the number parameters can be reduced by combining Eqs. (6.20) and (6.16). The frictional stress at the plug surface and the width of the lubrication layer can now be written in the form

$$\begin{cases} \tau_{\mathrm{s}} = \max\left\{0, P^*_{\mathrm{s0}} - C^*_{\mathrm{L}} \times \frac{1}{2}\rho_{\mathrm{f}} u_{\mathrm{s}}^2\right\} \\ h = \max\left\{0, \Gamma^* \left(C^*_{\mathrm{L}} \times \frac{1}{2}\rho_{\mathrm{f}} u_{\mathrm{s}}^2 - P^*_{\mathrm{s0}}\right)\right\} \end{cases} \tag{6.21}$$

where a set of reduced parameters is defined by

$$P^*_{\mathrm{s0}} \equiv C_{\mathrm{s}} P_{\mathrm{s0}} \tag{6.22}$$

$$C_{\mathrm{L}}{}^* \equiv C_{\mathrm{s}} C_{\mathrm{L}} \tag{6.23}$$

$$\Gamma^* \equiv \Gamma / C_{\mathrm{s}} \tag{6.24}$$

The velocity profiles in the plug flow regime are governed by Eqs. (6.4), (6.12), (6.13), and (6.21), which include four free material parameters k, P^*_{s0}, C^*_{L}, and Γ^*. Notice that these parameters depend, in general, on the suspension consistency. The permeability k is the only one of these parameters that explicitly influences the flow of the carrier fluid, see Eq. (6.13). The remaining three parameters govern the dynamics of the lubrication layer via Eqs. (6.21). The evaluation of the material parameters will be postponed until Sect. 6.3 where the parameters are determined by a least-squares fit in the experimental loss data.

Given these basic results one can now find the limiting values of wall stress (pressure gradient) where the fibre plug is first set to motion and where the lubrication layer is first formed. The value τ_{w0} at which the fibre plug starts to move can be solved by setting $u_{\mathrm{s}} = 0$, $\tau_{\mathrm{s}} = C_{\mathrm{s}} P_{\mathrm{s}0} = P^*_{\mathrm{s}0}$ and $h = 0$ in Eq. (6.12), and solving for the wall stress. The result is

$$\tau_{w0} = \left(1 - \frac{2}{R}\phi\sqrt{\phi k}\right)^{-1} P^*_{\mathrm{s}0}. \tag{6.25}$$

When the wall stress is below this limit, the fibre plug is stationary, and the mechanical friction τ_{s} must be calculated from Eq. (6.12) by setting $u_{\mathrm{s}} = 0$ and $h = 0$. The value τ_{w1} at which the lubrication layer is created can be found by setting $P_{\mathrm{s}} = 0$ in Eq. (6.15) to solve for the corresponding plug velocity, and then applying Eq. (6.12). The result is

$$\tau_{w1} = \left(1 - \frac{2}{R}\sqrt{\phi k}\right)^{-1} \left(\frac{2P^*_{\mathrm{s}0}}{C^*_{\mathrm{L}}\mu_{\mathrm{f}}^2/(\rho_{\mathrm{f}} k)}\right)^{1/2} \sqrt{\phi}\mu_{\mathrm{f}}^2/(\rho_{\mathrm{f}} k). \tag{6.26}$$

6.2 Velocity profile in the mixed and turbulent flow regimes

For the turbulent flow regimes III - V, illustrated in Fig. 5.15, one have to rely on the experimental profile correlations that were obtained using pulsed ultrasound Doppler velocimetry, see chapter 5. Figure. 6.3 shows the mean velocity profiles of pine fibre suspension of consistency 1% for flow rate ranging from 1.5 l/s to 5 l/s. Due to noise caused by the wall-fluid interface, the velocity measurement by the PUDV method is not accurate below 1 mm from the wall, and those results are excluded from the profiles shown. A peculiar feature of the measured mean velocity at high flow rates is the S -shaped profile near the wall. (A similar result was obtained recently also by Xu and Aidun for rectangular channels [XA05].) As in the case of Newtonian flows, parameterization of turbulent velocity profiles of fibre suspensions is best done by utilizing the standard non-dimensional wall-layer variables defined by

$$u^+ = u/u^\star \tag{6.27}$$

$$y^+ = yu^\star/\nu_{\mathrm{f}} \tag{6.28}$$

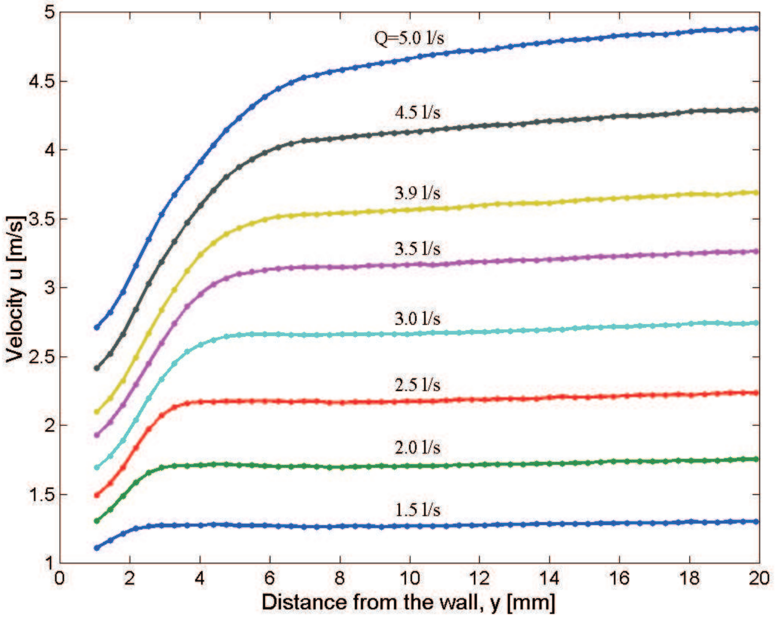

Figure 6.3: Mean velocity profiles of pine fibre suspension at consistency 1% as a function of distance from the pipe wall. The flow rate is varied from 1.5 l/s to 5 l/s where the flow is in the mixed or turbulent flow regimes. The centre line of the acrylic pipe is located at $y = 20\,\text{mm}$.

where $u^\star = \sqrt{\tau_w/\rho_\text{f}}$ is the friction velocity, ρ_f and ν_f are the density and the kinematic viscosity of the fluid and τ_w is the wall shear stress obtained from the pressure drop measurements. Figure 6.4 shows the same velocity profiles as Fig. 6.3 but redrawn in the dimensionless variables. Also shown is the standard logarithmic velocity profile for turbulent Newtonian flow, namely:

$$u^+ = \frac{1}{\kappa}\ln(y^+) + B \tag{6.29}$$

where the constants κ and B have the standard values 0.41 and 5.5, respectively [Whi94]. A remarkable feature of the profiles shown in Fig. 6.4 is that there seems to exist a unique (approximate) envelope curve that corresponds to a limiting velocity profile shape as the flow rate approaches infinity. That envelope curve consists of a logarithmic near wall region where the profile coincides with that of Newtonian flow, a yield region where velocity gradient is higher than that of Newtonian flow, and a core region where the profile again is of the form given by Eq. (6.29) but with a value of constant B above that of Newtonian flows ($i.e.$ $B \sim 5$).

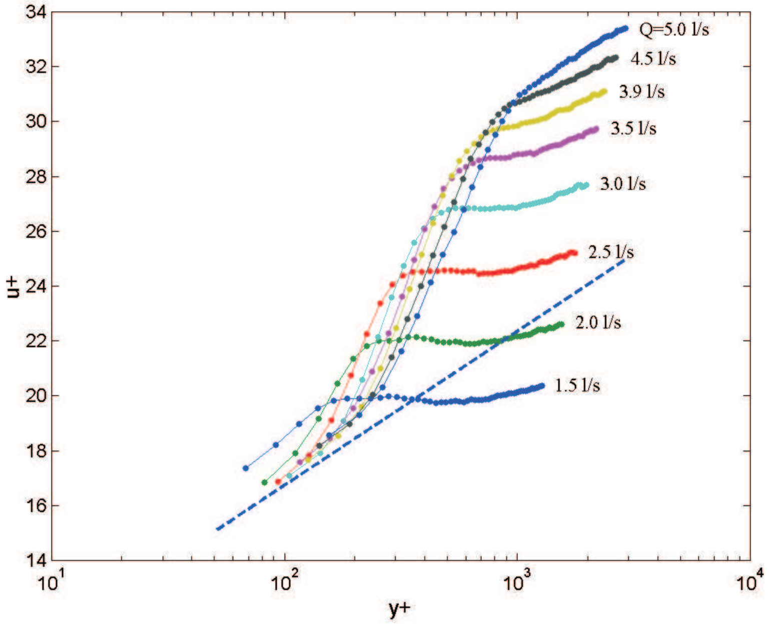

Figure 6.4: Same as Fig. 6.3 but for dimensionless velocity and distance from the pipe wall (see Eq. (6.27). The dashed line is the standard logarithmic profile of turbulent Newtonian flow, Eq. (6.29).

The near wall region extends up to a distance scale $y_L^+ \sim 10^2$. Correspondingly, the core region starts at a distance scale $y_H^+ \sim 10^3$ and extends up to pipe entry at $y^+ = R^+ = Ru^\star/\nu_{\rm f}$. The yield region (in very high flow rate limit) is located between y_L^+ and y_H^+.

At finite flow rates the dimensionless velocity profiles seem to be approximately independent of flow rate in the region near the pipe wall. At distances $y^+ < y_L^+$ the velocity profiles thus approximately coincide with that of Newtonian flow. Above that point in the yield region, the profiles follow the envelope curve up to a certain point $y_C^+ \leq y_H^+$ that depends on flow rate. From that point on, the velocity profiles again become approximately logarithmic with varying slope such that at low flow rates, the slope is zero and approaches the Newtonian profile value ($1/\kappa$ in the logarithmic y^+-scale) as the flow rate increases. The measured profiles can be approximated by a piecewise logarithmic profile of the form.

$$u^+ = \frac{1}{\kappa}\ln(y^+) + B + \Delta u^+ \tag{6.30}$$

where

$$\Delta u^+ = \begin{cases} 0 & 0 < y^+ \leq y_L^+ \\ \frac{\alpha}{\kappa} \ln\left(y^+/y_L^+\right) & y_L^+ < y^+ \leq y_C^+ (\leq y_H^+) \\ \Delta u_P^+ - \frac{\beta}{\kappa} \ln\left(y^+/y_L^+\right) & y_C^+ < y^+ \leq R^+ \end{cases} \tag{6.31}$$

Here, α and β give the slope (relative to Newtonian profile value) of the envelope curve in the yield region and the core region, respectively. Figure 6.5 illustrates the simplified profile and the meaning of various parameters. Notice that the quantities y_L^+ , y_H^+ and α are constants for a given suspension. Instead, β and y_C^+ depend on flow rate (on τ_w) in a manner that remains to be found. Within the present parameterization for each velocity profile at a finite flow rate, y_C^+ denotes the point where the profile departs from the high flow rate envelope curve, and the upper limit of the yield region. (At very low flow rates, that point may appear already at the near wall region in which case the yield region does not exist.) Obviously, the flow is turbulent and the fibre phase is fluidized in the near wall and yield regions. The existence of the yield region is most likely related to quenching of wall induced turbulence due to presence of fibres. As a consequence, the rate of turbulent transfer of longitudinal momentum from the core region towards the wall (and thus, the effective eddy viscosity of the suspension) is reduced. The existence of the yield region is thus identified as the primary

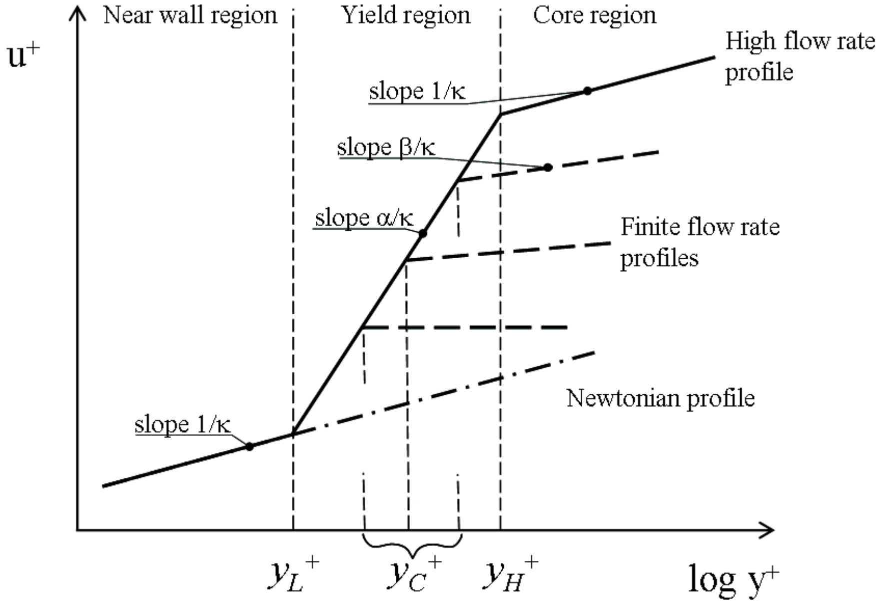

Figure 6.5: The piecewise logarithmic approximation of measured velocity profiles shown in Fig. 6.3. The parameters are as in Eqs. (6.30) and (6.31).

phenomenon underlying the drag reduction found in the mixed and turbulent flow regions. Indeed, according to the present results, set up of the drag reduction regime takes place at the flow rate regime where the yield region in the velocity profile first appears.

At relatively low flow rates, the velocity profile in the core region is flat indicating existence of a central fibre plug and y_C^+ denotes the position of the plug surface. According to the conventional reasoning, plug rupture takes place at the position where the total stress equals the disruptive shear stress τ_D which, in turn, is a material property of the fibre network. This suggests a correlation for y_C^+ in the form

$$y_C^+ = R^+(1 - \tau_D/\tau_w) \tag{6.32}$$

It appears, however, that this correlation is not in accordance with the observed profiles and loss behaviour (see below). As discussed above, the concept of disruptive shear stress as the criterion of plug rupture is somewhat questionable in the case where no actual rupture of once formed fibre network takes place. It is assumed here, instead, that the existence of fluidized annulus and fibre plug is controlled by a critical turbulent intensity that can prevail in the suspension. Lacking the possibility to measure the absolute values of turbulent intensity the assumption is made that the turbulent intensity is correlated with the mean flow velocity gradient, instead of total shear stress level. In other words, we conjecture that the upper limit of the yield region is set by the requirement that the mean velocity gradient is a (material) constant at that location, i.e. that

$$\left.\frac{\mathrm{d}u}{\mathrm{d}y}\right|_{y_C} = \Gamma_C = \text{constant} \tag{6.33}$$

Converting this equation in dimensionless form, solving for y_C^+ in the yield region and taking into account the limitation $y_C^+ \leq y_H^+$ set by the present quite rough parameterization of the profile, leads to the correlation

$$y_C^+ = \min\left(y_H^+, (u^\star/u_C^\star)^2\right), \tag{6.34}$$

where

$$u_C^\star = \sqrt{\frac{\nu_\mathrm{f}\kappa\Gamma_C}{1+\alpha}}. \tag{6.35}$$

Notice that according to Eq. (6.34), y_C^+ does not depend on pipe radius, as it would according to Eq. (6.32). If necessary, this result can be generalized to other parts of the profile and to more refined profile parameterizations. Finally, examination of the profile data suggests correlating the core region slope parameter β with y_C^+ as

$$\beta = 1 - \left(y_C^+/y_H^+\right)^2 \tag{6.36}$$

To summarize, the velocity profiles in mixed and fully turbulent flow regimes are parametrized by Eqs. (6.30) and (6.31) that include four free parameters: y_L^+, y_H^+, α and $u_C^\star$ (or alternatively, Γ_C). Figure 6.6 shows the measured and fitted profiles for 1% pine and 2% birch at several flow rates in the mixed and turbulent regions. The fitted parameter values are given in Table 6.1. Notice however, that for birch suspension, the yield layer seems to be located too close to the wall to be reliably measured by PUDV method for all but the highest flow rates (i.e. within the range 1 mm from the wall). This feature gives rise to some additional uncertainty in the fitted values of profile parameters for 2% birch suspension. A reliable estimation of the uncertainty in the fitted values of the parameters is not possible with the limited set of experimental data used in the present study. For the same reason, the dependence on the consistency and on fibre properties of the parameters cannot be determined based on the current results.

Parameter	Pine 1%	Birch 2%
y_L^+	120	50
y_H^+	880	320
α	1.8	2.4
$u_C^\star$[m/s]	0.0047	0.0125

Table 6.1: Fitted values of profile parameters for 1% pine and 2% birch fibre suspension.

Given the new profile information obtained by the PUDV method, the dynamics of the transition from the incipient turbulent regime via mixed flow regime to the fully turbulent regime (regimes III, IV and V in Fig. 5.15 can now been discussed in more detail.' The incipient turbulence region most likely arises due to growth of the lubrication layer thickness until turbulent fluctuations of the fluid phase can exist between the wall and the fibre plug. The edge of the fibre plug is not sharp, however. Instead, a surface layer exists where the average fibre consistency increases from zero to some constant value within a distance scale set by a structural correlation length of the fibre network (that is left unspecified in this work but can be expected to be of the order of fibre length, but may depend on consistency).

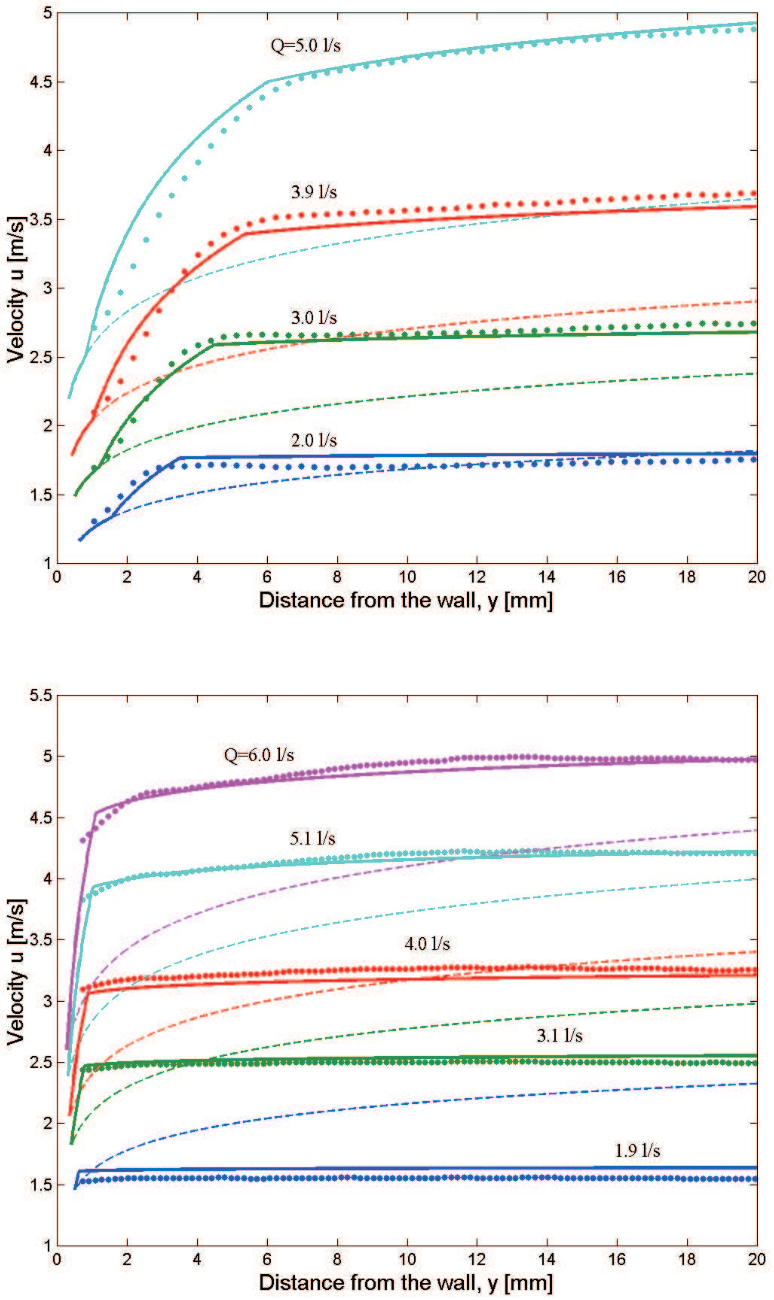

Figure 6.6: Measured velocity values (solid symbols) and fitted profiles (solid lines) at different flow rates in mixed and turbulent flow regimes for 1% pine (top) and 2% birch (bottom). Also shown are the logarithmic Newtonian profiles (dashed lines) corresponding to same values of wall stress (loss) as the measured profiles.

Due to low fibre consistency near the surface, the fluid phase turbulence is not effectively damped until well inside the plug. Consequently, the flow behaviour is dominated by fluid phase turbulence in a region that starts from the outer edge of the viscous sub-layer well inside the fibre free lubrication layer, and extends inside the fibre core a distance of the order of correlation length. This explains the observed behaviour that the velocity profile of fibres approach that of turbulent Newtonian fluid near the wall. Remember that the PUDV techniques could not be applied close enough to the wall such that the linear viscous sub-layer could be resolved.

As the flow rate is increased, turbulence production at the wall increases and fluctuations can prevail deeper in the fibre phase core preventing fibres from forming continuous network within some annular region. Well inside the core, fibre consistency is high leading to effective attenuation of turbulent fluctuations. The attenuation is most effective in the size scale of correlation length. On the other hand, the size scale of the largest eddies, that contain most of the turbulent energy and that are most effective in momentum transfer (i.e. in generating turbulent friction) is set by the distance from the wall. An immediate consequence of the arguments given above is that at a distance of the order of correlation length from the wall, the largest eddies possible at that distance, are effectively attenuated by the fibres. Consequently, the turbulent friction is attenuated leading to the yield layer characterized by increasing velocity gradient and the S-shaped profile shown in Fig. 6.4. (Obviously, this conclusion is based on an assumption that the friction is dominated by turbulence.) The existence of the yield layer, located between y_L^+ and y_C^+ in the schematic illustration of the profile parameterization shown in Fig. 6.5, is the origin of the drag reduction phenomenon - although within the present reasoning that region could more accurately be described as the 'region of flow enhancement'.

As the flow rate is further increased, the turbulent production still increases and the turbulent annulus can diffuse deeper in the fibre core. Entering further away from the wall leaves space to larger eddies that are not anymore attenuated very effectively. As a consequence, the core region can finally remain turbulent due to eddies larger than correlation length. Furthermore, the large scale end of the turbulent spectrum near the pipe centre can become similar to that of pure fluid. At very high flow rates the turbulent momentum transfer and consequently the mean velocity gradient approaches that of turbulent Newtonian flow. That would explain the limiting value of slope in the logarithmic -scale in the core region (see Figs. 6.4 and 6.5).

6.3 Loss correlations

In this section the frictional loss will be studied in detail. The aim is to utilize the modeled velocity profile in the plug flow regime and the parametrized experimental velocity profile in the mixed and turbulent regimes, and thereby derive a semiempirical correlation formula for the loss. The flow rate corresponding to a given friction velocity/wall stress (that yields the loss) is found simply by integrating the velocity profile over the pipe cross section.

6.3.1 Plug flow regimes

For the plug flow regimes, integration of the average bulk velocity $\phi u_\mathrm{f} + (1-\phi)u_\mathrm{s}$ over the cross-section of the pipe using Eqs. (6.12) and (6.13) yields

$$Q = 2\pi R \frac{\phi k}{\mu_\mathrm{f}} \left(\tau_\mathrm{s} - (1-\phi)\tau_w\right) + \pi R^2 u_\mathrm{s} + \frac{\pi R}{\mu_\mathrm{f}} \tau_w h^2 \tag{6.37}$$

Further investigation of Eq. (6.37) reveals that the dominant term on the right side is the second one for all values of wall shear within the plug flow regimes, except of those very close to τ_{w0} where the fibre plug starts to move. As a good approximation valid for most practical cases in the plug flow regimes, one can thus write

$$Q \cong \pi R^2 u_\mathrm{s} \tag{6.38}$$

The permeability is chosen here to be modeled with Eq. (2.56), the result derived by Jackson and James [JJ86]. It should be noticed that the results in Eqs. (2.54) - (2.56) were derived for smooth circular cylinders. Real wood fibres, on the other hand, may have non-circular cross-section, and a rich surface structure. Especially fibrillation due to mechanical processing (beating) increases the specific surface area of fibres, thus the drag on fibres increases and the permeability decreases. Thereby, the effective radius a in Eqs. (2.54) - (2.56) should be considered as a free material parameter that gives the specific permeability scale $k_0 = a^2$.

The values of the material parameters k_0, $P^*_{\mathrm{s}0}$, C^*_L, and Γ^* were found by a least-squares fit of Eq. (6.38) in the experimental loss data separately for each suspension consistency. The results are shown in Figs. 6.7 (pine) and 6.8 (birch). Notice that in the figures shown is the permeability k as is given by Eq. (2.56), and not the specific permeability k_0.

In what follows, the reduced material parameters P_{s0}^*, ${C_{\mathrm{L}}}^*$, and Γ^* are expressed as functions of consistency (the permeability k is given by Eq. (2.56)). To that end, the expected qualitative dependence on the consistency of the material parameters is shortly discussed, and simple analytic expressions are proposed that have these qualitative features.

According to Eq. (6.21), the shear stress at the plug surface, τ_{s}, is in the percolating flow regime (fibre plug is stationary) equal to the reduced parameter P_{s0}^*. This stress corresponds to the loss that is obtained by extrapolating the loss curve to zero flow rate. Equation (6.26) states that the wall shear stress at the local maximum of the loss curve, τ_{w1}, increases with the parameter P_{s0}^*. Further analysis of the governing equations show that the overall level of the loss increases with this parameter, as expected. The experimental loss data clearly demonstrates, on the other hand, that loss increases with consistency. One may thus conclude that the value of parameter P_{s0}^* should increase with consistency. This is clearly the case with the values that were inferred from the fitting procedure described above, these values are shown as open markers in Figs. 6.7 and 6.8.

It may be also seen that the dependence on the consistency of the parameter P_{s0}^* is nonlinear, in general. Moreover, the value of the parameter tends to zero as the consistency approaches the lowest value used in the analysis. This lowest consistency coincides with the threshold value shown on the last line of table 4.2 and 4.3 for pine and birch fibre suspension, respectively. Thus the dependence on the consistency of P_{s0}^* is quite analogous to that of the shear modulus given by Eq. (4.25) and the ultimate shear strength given by Eq. (4.26), and the parameter P_{s0}^* is chosen to be modeled with a similar expression:

$$P_{\mathrm{s0}}^* = \tau_0(\max(c, c_0)/c_0 - 1)^{\alpha_\tau}, \tag{6.39}$$

where c is the percentage consistency, c_0 is the threshold consistency for the plug formation, and τ_0 and α_τ are free material parameters.

As can be seen from the experimental results shown in Figs. 5.13 and 5.14, the thickness of the lubrication layer decreases with increasing consistency. Equation (6.19) states, on the other hand, that the thickness of the layer increases with the parameter Γ^*. Thus one may conclude that Γ^* decreases with increasing consistency. The parameter Γ^* is chosen to be written in a power-law form

$$\Gamma^* = \Gamma_0 c^{\alpha_\Gamma}, \tag{6.40}$$

Γ_0 and α_Γ are free material parameters. One expects Γ^* to decrease with increasing consistency, thus the exponent α_Γ should be negative. The material parameter C_{L}^* is expressed in the form

$$C_{\mathrm{L}}{}^* = C_{\mathrm{L}0} c, \tag{6.41}$$

where $C_{\mathrm{L}0}$ is a free material parameter. Notice that the formulas given in Eqs. (6.39)- (6.41) do not have direct physical justification, but were chosen merely as they have the correct qualitative behaviour and reproduce the experimental results with reasonable accuracy.

At this point our model contains six material parameters defined by Eqs. (6.39)- (6.41) and (2.56), namely k_0, τ_0, $C_{\mathrm{L}0}$, Γ_0, α_τ, and α_Γ. It is tempting to evaluate the values of these parameters by fitting Eqs. (6.39)- (6.41) and (2.56) into values of the material parameters k_0, $P_{\mathrm{s}0}^*$, C_{L}^*, and Γ^* that are shown as open markers in Figs. 6.7 and 6.8. It was found, however, that this does not reproduce good approximation to the observed loss data. Instead, the values of these parameters were found for each wood species by fitting the model in all the experimental loss data at all consistencies in one go. The results are shown in Table 6.2. The fitted functions are shown as solid lines in Figs. 6.7 and 6.8. Notice that a reliable estimation of the uncertainty in the fitted values of the parameters is not possible with the limited set of experimental data. The measured loss data and the loss predicted by the model are shown in Figs. 6.9 and 6.10 for pine and birch fibre suspensions, respectively. The model reproduces the loss data with moderate accuracy, the difference between the calculated and the experimental losses is of the same order as the scatter in the experimental data itself. At the point where the lubrication layer is formed, the model produces a sharp corner in the loss curve. This is a consequence of the simplification made in the model. The fibre network is considered as a sharp-edged plug that undergoes an abrupt transition from the state with wall contact to the sate with lubrication layer. In this transition the number of fibres in contact with the wall has a discontinuous jump to zero. In reality the surface of the fibre plug has a complicated floc structure that one expects to change as the fibre plug is lifted off the pipe wall. Especially the average number of fibres in contact with the wall decreases smoothly, and there is a gradual rather than sudden transition to the next flow regime with lubrication layer.

Species	k_0 [10^{-9} m^2]	τ_0 [Pa]	$C_{\mathrm{L}0}$	Γ_0 [10^{-6} m/Pa]	α_τ	α_Γ
Pine	1.0	0.12	0.0012	93	3.1	-3.7
Birch	0.58	3.6	0.0008	310	2.0	-4.8

Table 6.2: Fitted parameters for pine and birch fibre suspensions

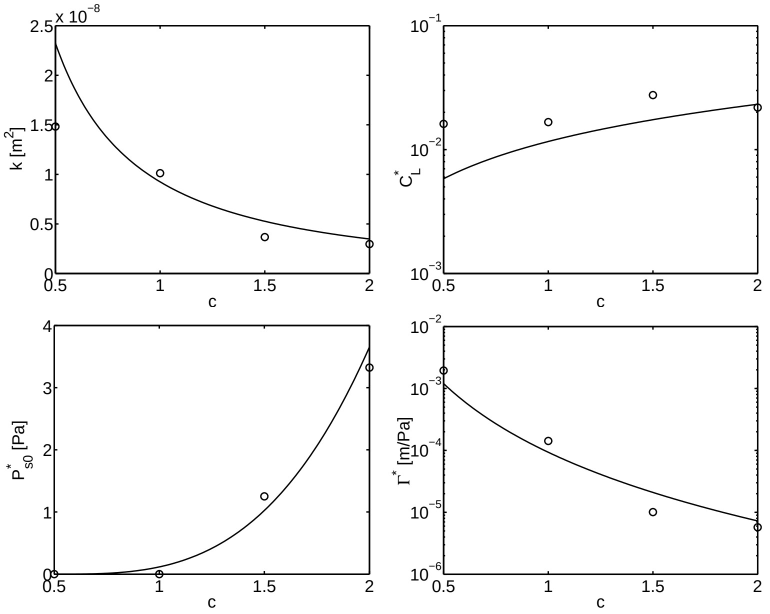

Figure 6.7: The values of the physical parameters determined by a least-squares fit in the experimental data for pine fibre suspension. Open markers are the values calculated for each consistency separately, while the solid lines are given Eqs. (2.56), and (6.39)- (6.41).

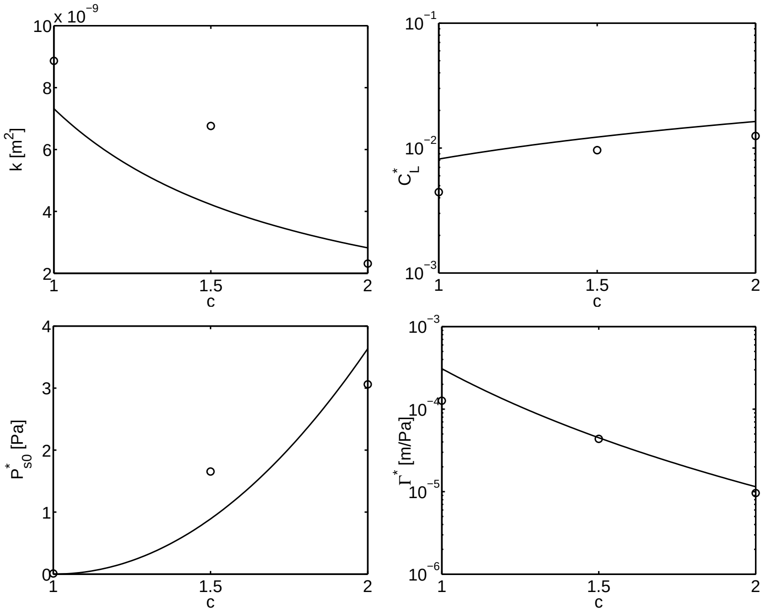

Figure 6.8: As Fig. 6.7 but for birch fibre suspension.

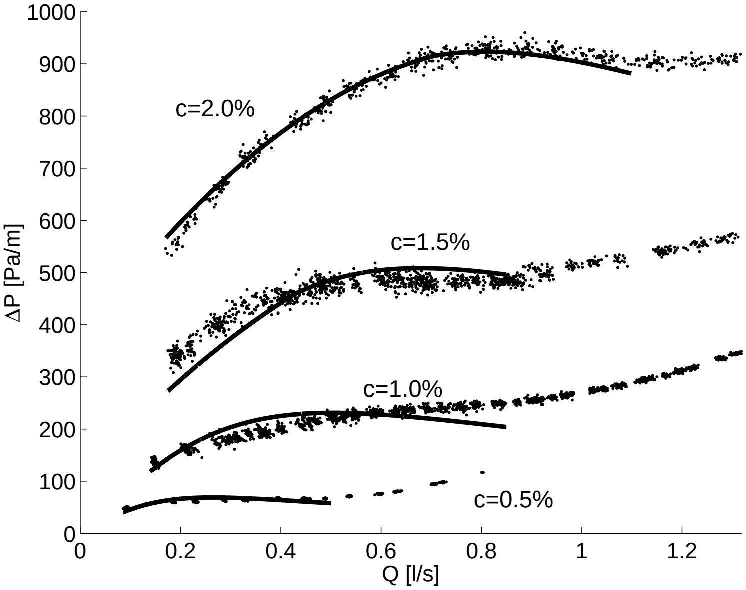

Figure 6.9: Measured (small markers) and calculated (solid line) loss as a function of flow rate for pine suspension at consistencies 0.5%–2.0%.

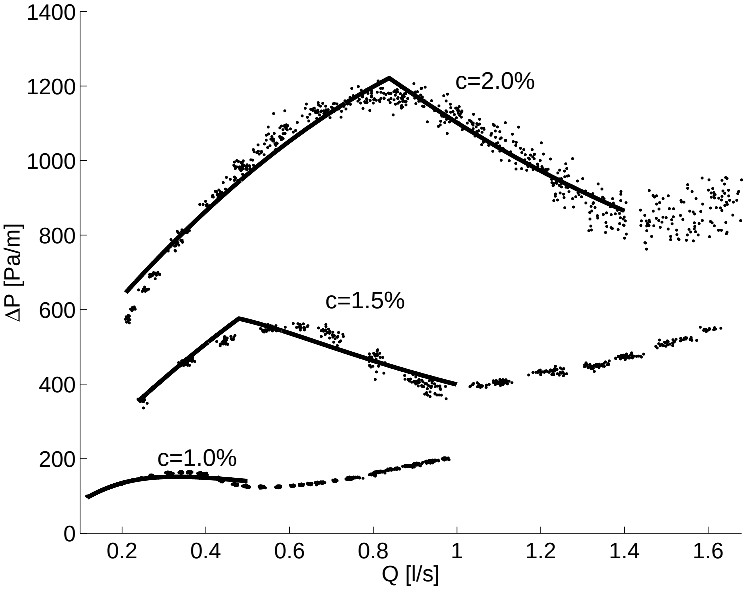

Figure 6.10: As Fig. 6.9, but for birch suspension at consistencies 1.0% – 2.0%.

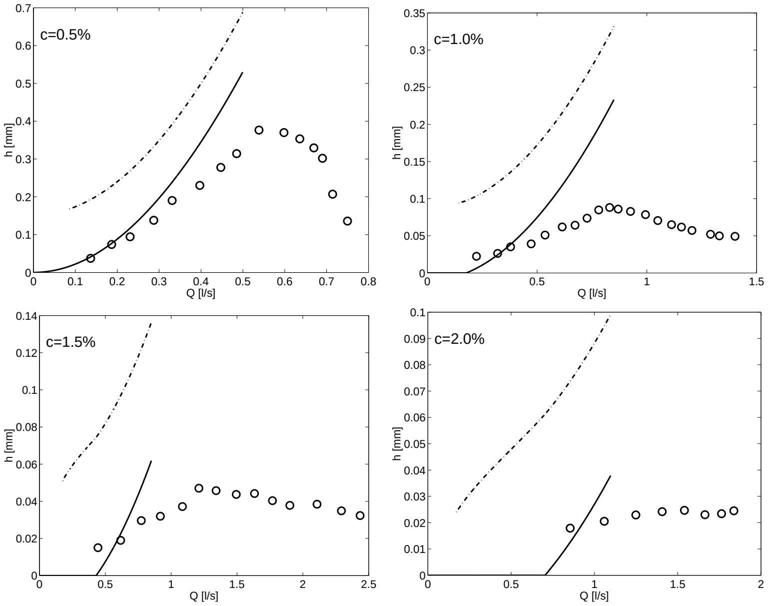

Figure 6.11: The thickness of the wall layer as a function of flow rate for pine suspension at consistencies 0.5% – 2.0%. Open markers are the experimental results, solid line is given by the two-phase model, and dashed line is given by Eq. (4.8).

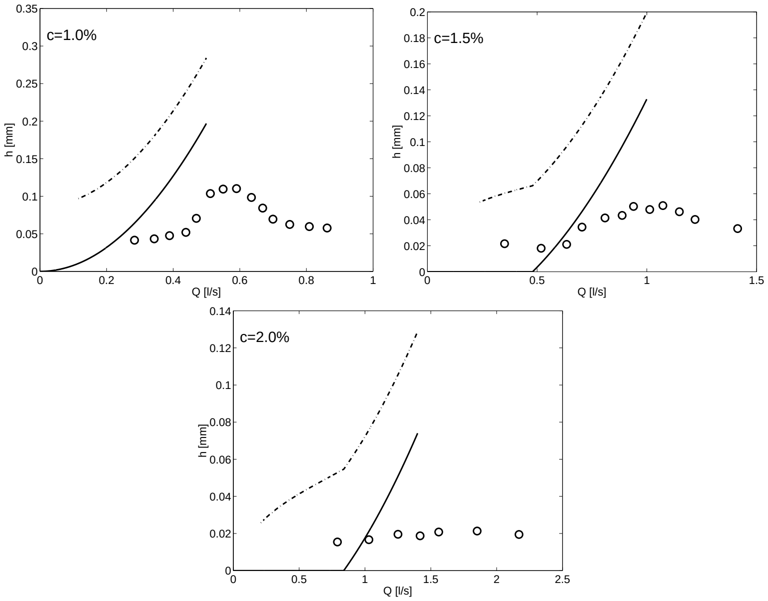

Figure 6.12: As Fig. 6.11, but for birch suspension at consistencies 1.0% – 2.0%.

The measured width of the lubrication layer and the width predicted by the model are shown in Figs. 6.11 and 6.12 for pine and birch fibre suspensions, respectively. Even though the model predicts layer widths that are larger than the measured values, the qualitative behaviour of the modeled results is quite similar to the experimental results. The difference between the results is most likely due to the fact that in the model the fibre plug is considered as a sharp-edged object, while in reality the plug surface has an irregular floc structure and individual fibres are protruding out of the plug as well. The intensity of the light reflected from the fibres increases substantially as the incoming beam hits the outermost fibre flocs. Thus the location of the plug surface as given by the laser-optical measurement is close to this depth. From modeling point of view, on the other hand, the effective surface of the plug seen by the fluid flow is deeper inside the roughness layer of the plug, and the layer thickness predicted by the model is larger than observed thickness.

6.3.2 Mixed and turbulent flow regimes

For mixed and turbulent regions, integration of the velocity profile given by Eqs. (6.30) and (6.31) yields

$$Q^+ = Q_0^+ + \Delta Q_1^+ + \Delta Q_2^+, \tag{6.42}$$

where

$$\begin{aligned}
Q_0^+ &= \pi (R^+)^2 \frac{1}{\kappa} \left[\ln R^+ + B\kappa - \frac{3}{2} \right] && (6.43) \\
\Delta Q_1^+ &= \pi (R^+)^2 \frac{\alpha}{\kappa} \left[\ln \left(\frac{y_C^+}{y_L^+} \right) + \frac{1}{2} \left(\left(\frac{y_C^+}{R^+} \right)^2 - \left(\frac{y_L^+}{R^+} \right)^2 \right) \right. \\
&\quad \left. -2 \left(\left(\frac{y_C^+}{R^+} \right) - \left(\frac{y_L^+}{R^+} \right) \right) \right] && (6.44) \\
\Delta Q_2^+ &= \pi (R^+)^2 \frac{\alpha}{\kappa} \left[\ln \left(\frac{y_C^+}{y_L^+} \right) + \frac{1}{2} \left(\left(\frac{y_C^+}{R^+} \right) - 3 \right) \left(\left(\frac{y_C^+}{R^+} \right) - 1 \right) \right] && (6.45)
\end{aligned}$$

Here, the first term Q_0^+ is the contribution of the standard Newtonian profile, the second term ΔQ_1^+ gives the additional flow contribution due to yield region and the constant velocity contribution in the core region. The third term ΔQ_2^+ includes the effect of the non-zero slope in the core region (that becomes significant at high flow rates, see Fig. 6.5). Finally the flow rate Q in physical dimensions is given in terms of the dimensionless flow rate as

$$Q = \frac{\nu_{\mathrm{f}}^2}{u^\star} Q^+. \tag{6.46}$$

This equation gives the required correlation between the flow rate and loss. Figure 6.13 shows the measured loss for 1% pine and 2% birch suspensions together with the correlations given by Eqs. (6.42) - (6.45). For the turbulent regime, the loss is calculated using the parameter values given in Table 6.1 as obtained from a fit to profile data. Notice that while knowing the profile parameters y_l^+, y_H^+, α and $u_C^\star$ immediately yields an accurate loss correlation, the inverse is not true: knowledge of loss behaviour alone does not yield unique values of profile parameters. Consequently, a direct fit of Eqs. (6.42) - (6.45) in the turbulent regime would lead to even closer agreement with the loss data as the one shown in Fig. 6.13, but with parameter values that do not reproduce good approximation to the measured profiles through Eqs. (6.30) and (6.31).

As shown by Fig. 6.13, the agreement between measured and calculated loss behaviour is very good in the present cases. At the relatively low consistencies considered here, the mixed and turbulent flow regimes are obviously the most important regimes from practical point of view. At those domains, the loss correlation discussed above is based on a somewhat arbitrary and suggestive parameterization of the flow profile, the generality of which can not be assured given the rather small amount of data yet available. However, even more important than the explicit functional form of the loss correlation given by Eqs. (6.42)- (6.46), these formulas suggest a certain scaling law of the correlation, namely that

$$Q^+ = Q^+(R^+, u^\star/u_C^\star), \tag{6.47}$$

i.e. that the dimensionless flow rate of suspension depends only on two quantities, the dimensionless pipe radius R^+ and the ratio $u^\star/u_C^\star$, where $u_C^\star$ is a material parameter related to the critical turbulent intensity that is sufficient to keep the fibre phase fluidized. Furthermore, it appears that the primary variable here is R^+. Instead, the dependence on $u^\star/u_C^\star$ is relatively weak and limited to low flow rate end of the mixed flow region. As a good approximation one can then drop the dependence on $u^\star/u_C^\star$ in Eq. (6.47). In particular, using Eqs. (6.42)-(6.45) in the high shear stress limit, and using the approximation valid for large pipes that $y_H^+, y_H^+ << R^+$ one gets

$$Q^+ \approx Q_0^+ + \Delta Q_\infty^+ \tag{6.48}$$

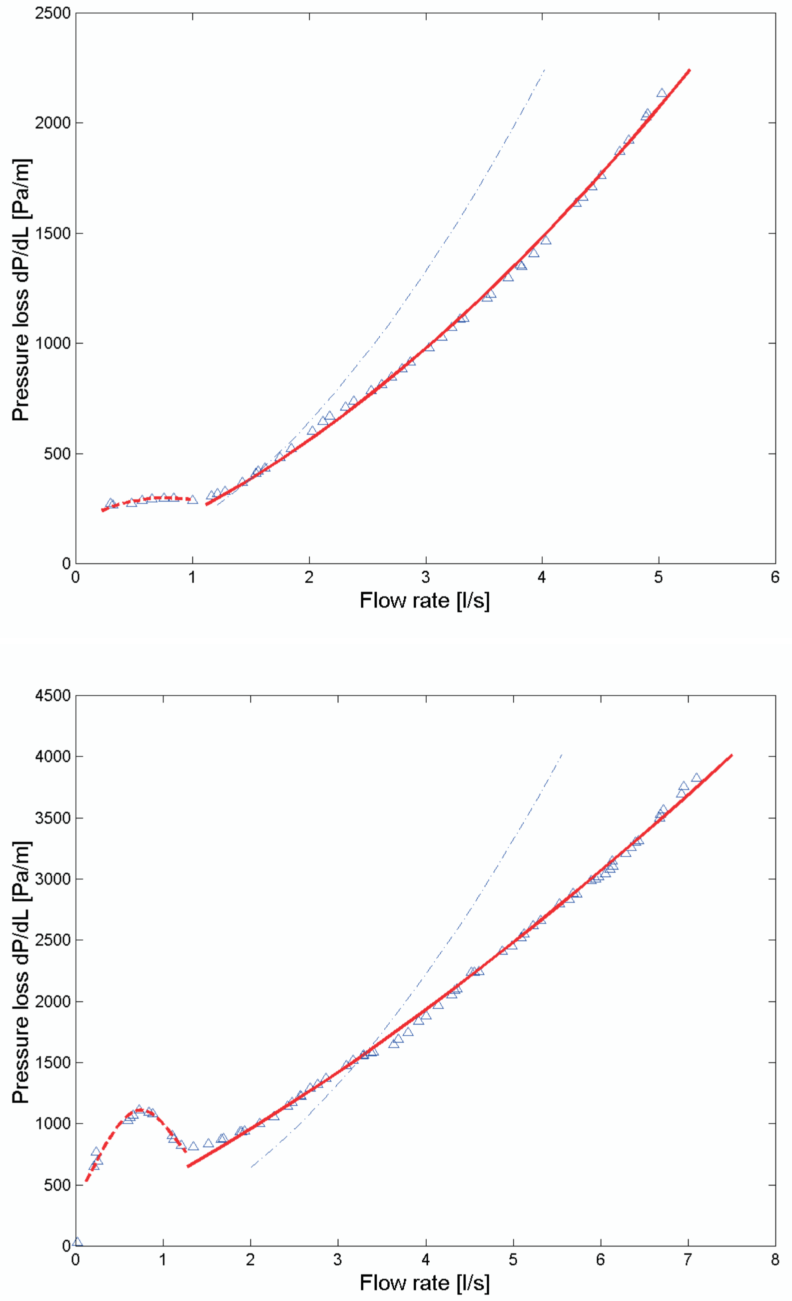

Figure 6.13: Measured (symbols) and calculated loss for plug flow (dashed line) and turbulent regime (solid line) as a function of flow rate for 1% pine (top) and 2% birch (bottom). Also shown is the Newtonian correlation for smooth pipe turbulent flow (dash-dotted line).

where Q_0^+ is given by Eq. (6.43) and

$$\Delta Q_\infty^+ = \lambda_1 R^+ + \lambda_2 (R^+)^2 \tag{6.49}$$

Instead of four material parameters for the velocity profiles (see Table 6.1), one is now left with only two material parameters λ_1 and λ_2 that are related to the original profile parameters as

$$\lambda_1 = 2\pi \tfrac{\alpha}{\kappa} \left(y_H^+ - y_L^+ \right) \tag{6.50}$$

$$\lambda_2 = \pi \tfrac{\alpha}{\kappa} \ln \left(y_H^+ / y_L^+ \right) \tag{6.51}$$

In order to test the scaling law Eq. (6.47), in Fig. 6.14 is shown the loss data measured at the flow laboratory of Techinal Research Center of Finland for 1% commercial fine, LWC and SC pulps in three different standard steel pipe sizes DN100, DN200 and DN300 [Luu]. The measurement was done only in mixed and turbulent regimes where the three pulps show very similar loss behaviour. No profile information is available. Also shown in Fig. 6.14 are the results obtained by fitting Eqs. (6.48) and (6.49) using only the data for the smallest pipe size, DN100. The curves for the two larger pipes then ensue purely from the proposed scaling law. The fitted values of the two parameters are $\lambda_1 = 96600$ and $\lambda_2 = 7.33$. As discussed above, knowledge of loss behaviour alone does not yield unique values of profile parameters. It was, however verified that plausible values of profile parameters can be chosen such that the loss behaviour shown in Fig. 6.14 is reproduced also by Eqs. (6.42)- (6.45).

6.4 Summary

Velocity profiles were studied in detail both in the plug-flow and the turbulent regimes. In the plug-flow regimes, velocity profiles were inferred from a simple two-phase model that is based on the averaged flow equations. In the model, the lubrication layer is modeled as a response to the inertial transverse lift force acting on the fibres near the pipe wall. The model contains four material parameters that describe the flow resistance of fibre network and the dynamics of the formation of the lubrication layer. The velocity profiles predicted by the model are typical to plug flow, and all the shearing occurs in a narrow wall layer the width of which is less than 1 mm.

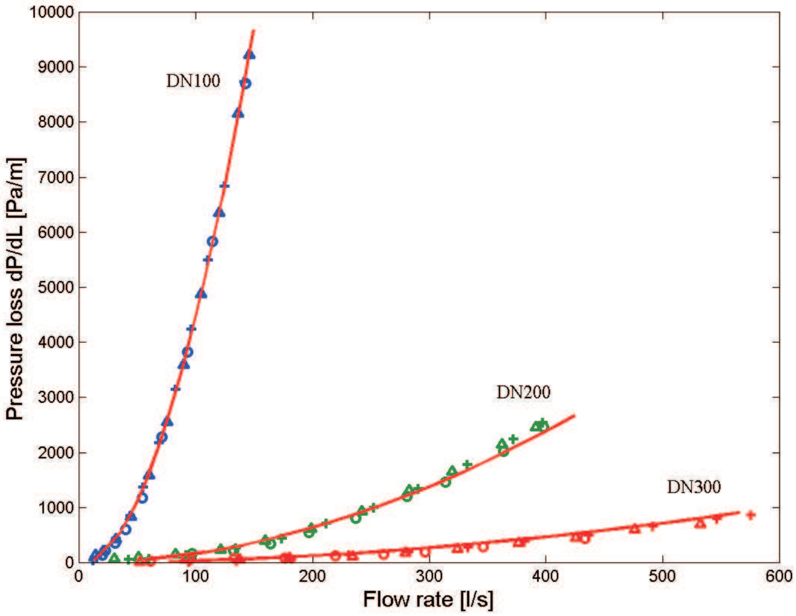

Figure 6.14: Measured loss as a function of flow rate for 1% commercial fine paper (□), LWC (O) and SC (+) pulps [Luu]. The measurement was done for three different standard steel pipes, DN100 ($\phi = 110.3\,\mathrm{mm}$), DN200 ($\phi = 215.1\,\mathrm{mm}$) and DN300 ($\phi = 300\,\mathrm{mm}$). Solid lines show the fitted behaviour according to Eqs. (6.48) and (6.49). The fit was done using the data for DN100 pipe only.

In the mixed and turbulent regimes the measured profiles were utilized. There seems to exist a unique envelope curve that corresponds to a limiting velocity profile shape as the flow rate approaches infinity. That envelope curve consists of a logarithmic near wall region where the profile coincides with that of Newtonian flow, a yield region where velocity gradient is higher than that of Newtonian flow, and a core region where the profile again is of the logarithmic form. The measured profiles were approximated by a piecewise logarithmic profile that contains four free material parameters that depend on consistency, in general. These parameters were determined by a direct least-squares fit in the experimental velocity profiles.

A semiempirical correlation formula for the loss was derived by utilizing the modeled velocity profile in the plug flow regime and the parametrized experimental velocity profile in the mixed and turbulent regimes. The flow rate corresponding to a given wall shear stress was found simply by integrating the velocity profile over the pipe cross section.

In the plug flow regimes, the values of the material parameters of the two-phase model were found by fitting the loss correlation predicted by the model in the observed loss. The modeled thickness of the lubrication layer behaves qualitatively in the same way as the observed one, yet the modeled values are in all cases larger than the experimental values. This difference is most likely due to the fact that in the model the fibre plug is considered as a sharp-edged object, while in reality the plug surface has a irregular floc structure and and individual fibres protruding out of the plug.

In the mixed and turbulent regimes, integration of the parametrized profiles yielded a loss correlation that agrees with high accuracy with the observed loss behaviour. Moreover, the derived loss correlation suggests a certain scaling law that can be used to predict loss in a pipe that has different diameter as the pipe that is used to fix the material parameters. The scaling law was tested in a case where the material parameters were fitted in loss data for a DN100 pipe. The loss predicted by the scaling law for a DN200 and A DN300 pipe agreed with the observed loss with high accuracy.

The existence of the yield region in the mixed and turbulent regimes is most likely related to quenching of wall induced turbulence due to presence of fibres. As a consequence, the rate of turbulent transfer of longitudinal momentum from the core region towards the wall is reduced. The existence of the yield region is thus identified as the primary phenomenon underlying the drag reduction found in the mixed and turbulent flow regions.

According to the measured velocity profiles in the mixed and turbulent regimes, two mechanisms are effective in the transition from mixed to fully turbulent flow. First, increase of turbulent intensity near the wall leads to annulus of disrupted fibre phase and a central fibre plug, the radius of which slowly decreases with flow rate. Second, at high enough flow rates, large scale fluctuations can persist throughout the core and the 'degree of fluidization' gradually increases with flow rate in the entire central core. At very high flow rates the large scale turbulent structure of the core region is similar to that of pure fluid (at the same wall shear stress) indicating 'fully fluidized' state of flow.

Chapter 7

Conclusions

In the second chapter of this monograph the multiphase equations were recapitulated that can be used to model flows of liquid-particle suspensions, and flows in porous medium. Derivation of a generic set of multiphase equations was first reviewed using the method of volume averaging. A plausible set of constitutive relations was then applied to render the equations applicable to liquid-particle suspensions, to flows in porous medium, and to the flow of wood fibre suspension in the plug flow regime, in particular.

In the third chapter the interaction forces between the phases were studied with direct numerical simulations, and the emphasis was on the forces acting on solid particles in a flow near a solid wall. Specifically, the hydrodynamic forces acting on stationary solid cylinders were studied. It was found that hydrodynamic lift forces, *i.e.* forces perpendicular to the main flow direction, do exist in the flows of liquid-particle suspensions. These forces arise due to inertial effects, and are thereby complicated and rather poorly understood even for a case where a single particle is suspended in the flow. In the single-cylinder case, it was found that the nondimensional hydrodynamic drag and lift forces mainly depend on two nondimensional parameters, namely the dimensionless distance from the wall, and the ratio of the slip Reynolds number to the shear Reynolds number. It was found that the hydrodynamic force acting on a rigid matrix of long cylinders is qualitatively similar both for a matrix of unidirectional cylinders and for a matrix of cylinders with random orientation. The drag force is largest near a moving wall and approaches zero monotonically with increasing distance from the wall. Close to the moving wall the simulated drag force deviates considerably from the drag force predicted by Darcy's law. Numerical simulations indicate strongly repulsive lift force near the moving wall, and the maximum value of repulsion decreases as the gap width is increased. This strong repulsion decays within a distance that is $2-3$ times the cylinder radius and $5-10$ times the cylinder radius for unidirectional and random orientations of the cylinders, respectively. At that distance, the lift force acting on unidirectional cylinders changes to weak attraction, which decays rapidly with increasing distance as the fluid velocity approaches zero. For randomly oriented cylinders no region of significant attraction was found. The total lift force acting on the cylinders is strongly repulsive when the width of the gap between the moving wall and the fibre matrix is small, and decreases monotonically with increasing gap width. For unidirectional cylinders, the total lift force changes into attraction at the distance that is of the order of the cylinder radius. For randomly oriented cylinders, the total lift remained repulsive in all the simulations, and was close to zero for the largest gap width used that was 2.3 times the cylinder radius.

In the fourth chapter the unique flow behaviour of wood fibre suspensions was described at a qualitative level. Some characteristic features found in experimental frictional loss correlations were summarized, various flow regimes were studied, and the flow phenomena that are known to produce the observed loss correlation were discussed shortly. Next the most relevant efforts on modeling the flow of wood fibre suspension in straight pipes and on design equations and methods for determining friction loss were reviewed. The methods to characterize the various regimes of fibre flocculation and formation of coherent fibre networks were also reviewed. A few estimates of the threshold consistency above which coherent fibre networks may form were recorded.

In the fifth chapter the experimental work was described that was carried out on the flow properties of wood fibre suspensions on straight pipes. New experimental methods were used to acquire better grasp on the flow phenomena responsible for the peculiar flow properties. The thickness of the lubrication layer in the plug-flow regimes was inferred for fully developed flow with a novel technique that is based on measuring the intensity of laser light reflected by fibres. The transient behaviour of the flow after a sudden step that acted as a turbulence generator was also studied. The detailed time-dependent velocity profiles in such developing flow were measured with a pulsed ultra-sound velocimetry technique. From these velocity profiles, the local intensity of velocity fluctuations was calculated. Based on the results of these experiments, the flow was divided into five different regimes according to flow rate.

With the measuring techniques used in this study, the lubrication layer could not be observed at very low flow rates. The regime where the lubrication layer was not found coincides with the low flow rate domain where the loss increases with flow rate. This domain is identified as the plug flow regime with direct fibre-wall contact. In this regime the intensity of turbulence is high immediately after the source (constriction, pump, *etc.*), and the suspension is in a fluidized state where the fibre phase is broken into flocs. The intensity of the turbulence decays rapidly downstream from the source, and the fibre phase forms into a continuous network. In this process, the turbulent energy of fibres is partly captured as the elastic energy of the network. This elastic energy manifests itself as an elastic force that pushes fibres towards the pipe wall. The inertial lift force, on the other hand, repels fibres from the wall. In this regime of low flow velocity, the elastic force is, however, large enough to keep the fibre plug in a contact with the wall. Thus the fibre network forms into a state that spans through the pipe, and no observable lubrication layer is found. The radial force balance of the fibre plug is maintained between the elastic force, the lift force, and a support force by the wall. The support force gives rise to mechanical friction between the fibre plug and the pipe wall, increasing the loss.

An observable lubrication layer appears at the flow rate corresponding to the local maximum in the loss curve (birch) or to the point where the loss curve levels off (pine). Above that flow rate, the measured value of the lubrication layer thickness grows with flow rate until it reaches a maximum. This domain is identified as the plug flow regime with lubrication layer. In this regime the lift force is large enough to keep the fibres away from the pipe wall, on the average. Thus the fibre network forms into a state where there is a fibreless lubrication layer next to the pipe wall. The fibre plug slides on top of this lubrication layer, and the loss saturates or may even decrease with increasing flow rate.

In the next domain the measured thickness of the lubrication layer decreases with increasing flow rate. The observed decrease of the layer thickness is most likely due to incipient turbulence, *i.e.* turbulence in the fluid phase (that was not observe with the present methods). This turbulence is not yet strong enough to cause macroscopic breakage of the fibre network, but only to bend and dislodge individual fibres that are loosely bound to the fibre plug surface. These fibres can then be randomly displaced towards the pipe wall by fluctuations of fluid velocity, and thereby cause increased light scattering as they traverse the laser beam. The apparent decrease of lubrication layer thickness may thus be explained by dispersion of the fibre plug surface layer due to fluid phase turbulence. This domain is identified as the plug flow regime with smearing annulus. In this regime, the loss increases approximately linearly with flow rate.

As the flow rate increases, the overall turbulent intensity increases and the high intensity region extends further downstream. Above a certain flow rate, the increased wall friction now prevents fibres from forming continuous network near the walls. Instead, a turbulent annulus remains near the walls and a continuous network is formed only at the core. This is seen as the turbulent intensity maxima near the walls and a slightly more rounded mean flow profile in the developed flow region. This regime is identified as mixed flow regime. In this regime the dependence on the flow rate of the loss is approximately quadratic.

When the flow rate is high enough, the turbulence created by strong wall friction prevents the formation of the fibre plug throughout the pipe, and the suspensions remains in a fluidized state. This domain is identified as a fully turbulent regime. The dependence on the flow rate of the loss remains close to quadratic in the transition, thus the exact flow rate at which the fibre plug core disappears can not be identified from loss data. At very high flow rates, the loss behaviour approaches that of pure carrier fluid.

In the sixth chapter velocity profiles were studied in detail both in the plug-flow and the turbulent regimes. In the plug-flow regimes, velocity profiles were inferred from a simple two-phase model that is based on the averaged flow equations. In the model, the lubrication layer is modeled as a response to the inertial transverse lift force acting on the fibres near the pipe wall. The model contains four material parameters that describe the flow resistance of fibre network and the dynamics of the formation of the lubrication layer. The velocity profiles predicted by the model are typical to plug flow, and all the shearing occurs in a narrow wall layer the width of which is less than 1 mm.

In the mixed and turbulent regimes the measured profiles were utilized. There seems to exist a unique envelope curve that corresponds to a limiting velocity profile shape as the flow rate approaches infinity. That envelope curve consists of a logarithmic near wall region where the profile coincides with that of Newtonian flow, a yield region where velocity gradient is higher than that of Newtonian flow, and a core region where the profile again is of the logarithmic form. The measured profiles were approximated by a piecewise logarithmic profile that contains four free material parameters that depend on consistency, in general. These parameters were determined by a direct least-squares fit in the experimental velocity profiles.

A semiempirical correlation formula for the loss was derived by utilizing the modeled velocity profile in the plug flow regimes and the parametrized experimental velocity profile in the mixed and turbulent regimes. The flow rate corresponding to a given wall shear stress was found simply by integrating the velocity profile over the pipe cross section.

In the plug flow regimes, the values of the material parameters of the two-phase model were found by fitting the loss correlation predicted by the model in the observed loss. The modelled thickness of the lubrication layer behaves qualitatively in the same way as the observed one, yet the modelled values are in all cases larger than the experimental values. This difference is most likely due to the fact that in the model the fibre plug is considered as a sharp-edged object, while in reality the plug surface has a irregular floc structure and and individual fibres protruding out of the plug.

In the mixed and turbulent regimes, integration of the parametrized profiles yielded a loss correlation that agrees with high accuracy with the observed loss behaviour. Moreover, the derived loss correlation suggests a certain scaling law that can be used to predict loss in a pipe that has different diameter as the pipe that is used to fix the material parameters. The scaling law was tested in a case where the material parameters were fitted in loss data for a DN100 pipe. The loss predicted by the scaling law for a DN200 and A DN300 pipe agreed with the observed loss with high accuracy.

The experimental results reported in this monograph may not seem to add much to the qualitative understanding of the flow behaviour of wood fibre suspension in straight pipes. They do, however, indicate that the new experimental methods utilized here can be used to gain much more detailed information on the flow behaviour as has been previously possible. Based on already these results, even the qualitative behaviour of the pipe flow can be further specified to some extent.

Unlike often phrased, for a pipe flow in mixed or turbulent flow regions the wall friction does not break the continuous fibre network. Instead, wall friction prevents such a network from ever forming within an annulus of some thickness or in the entire pipe.

The appearance of the fibre free lubrication layer in the plug flow regime is often explained by mechanical models based on shear deformation of the network induced by the wall stress, and the resulting reduction of plug diameter. For a pipe flow brought about by a pump, such a model is unphysical simply because the undeformed state of the network never existed. Instead, the fibre plug forms from the fluidized state in decaying turbulence after a pump or any fluidizing device is originally of diameter slightly less than that of the pipe.

The drag reduction found in the mixed and turbulent flow regimes is due to a yield region in the velocity profile. The existence of this region is most likely related to quenching of wall induced turbulence due to presence of fibres. As a consequence, the rate of turbulent transfer of longitudinal momentum from the core region towards the wall is reduced.

According to the measured velocity profiles, two mechanisms are effective in the transition from mixed to fully turbulent flow. First, increase of turbulent intensity near the wall leads to annulus of disrupted fibre phase and a central fibre plug, the radius of which slowly decreases with flow rate. Second, at high enough flow rates, large scale fluctuations can persist throughout the core and the 'degree of fluidization' gradually increases with flow rate in the entire central core. At very high flow rates the large scale turbulent structure of the core region is similar to that of pure fluid (at the same wall shear stress) indicating 'fully fluidized' state of flow.

With the novel experimental methods used in this work, new information was inferred about the flow behaviour of wood fibre suspension in straight pipes. However, there are a few aspects that have to be considered further. Probably the most important thing that should be studied is the scaling of loss with pipe diameter. Within the present study, it was only tested in the turbulent flow regime in a single case. Further experiments are necessary for proper validation of the derived loss correlations. On the other hand, the experimental methods used in this study and the results reported here make possible new experimental works on related phenomena, *e.g.* mixing of chemicals by turbulence in paper making processes.

Appendix A

Appendix

A.1 The crowding factor

The crowding factor N is the average number of fibres in a spherical volume that has diameter equal to the length of a fibre [KS92]. The average mass of fibres in such volume, m_{fibres}, can be calculated by multiplying the volume of the sphere by the consistency of suspension:

$$m_{\text{fibres}} = \frac{4}{3}\pi \left(\frac{L}{2}\right)^3 c_m, \tag{A.1}$$

where L is the average length of a fibre and c_m is the consistency of the suspension. The average total length of the fibres in the volume is

$$\Sigma L_{\text{fibres}} = \frac{m_{\text{fibres}}}{\omega} = \frac{\pi}{6}\frac{c_m L^3}{\omega}, \tag{A.2}$$

where ω is the fibre coarseness (mass per unit length). Notice that in writin Eq. (A.1) coarseness is assumed to be constant, while in reality it usually depends, *e.g.*, on fibre length. The crowding factor can now be expressed in the form

$$N = \frac{\Sigma L_{\text{fibres}}}{L} = \frac{\pi}{6}\frac{c_m L^2}{\omega}. \tag{A.3}$$

The total length of fibres in a unit volume of suspension equals c_m/ω. The volume fraction of fibres is calculated by multiplying the total length with the average cross-sectional area of a fibre. For cylindrical fibres the volume fraction can be expressed in the form

$$\phi_{\mathrm{s}} = \frac{c_m}{\omega} \times \pi \left(\frac{d}{2}\right)^2 = \frac{\pi}{4}\frac{d^2 c_m}{\omega}. \tag{A.4}$$

By combining Eqs. (A.4) and (A.3), the crowding factor can be expressed in an alternative form as

$$N = \frac{2}{3}\phi_{\mathrm{s}} A^2. \tag{A.5}$$

A.2 The solid volume fraction versus the consistency

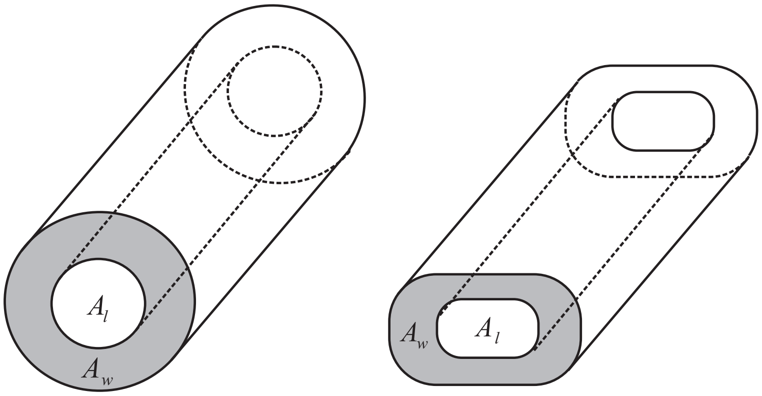

Figure A.1: Schematic view of the fibre structure, A_w is the fibre wall made of cellulose, and A_l is the lumen.

In this appendix correlations between the solid volume fraction and the solid mass fraction are derived for fully saturated fibres. To that end, fibres are considered as tubes that have wall made of cellulose, and a cavity, a *lumen*, at the centre, see Fig. A.1.

First the ratio of the cross-sectional area of the lumen to the cross-sectional area of the fibre wall is solved by considering a case where the lumen is filled by air. The mass of a fibre is $m_{\mathrm{fibre}} = L\omega$ and the volume of the fibre is $V_{\mathrm{fibre}} = LA_0$ where $A_0 = A_l + A_w$ is the area of the fibre cross-section and A_l and A_w are the cross-sectional areas of the lumen and the fibre wall, respectively. Thus the bulk density of the fibre can be given as

$$\rho_{\mathrm{fibre}} = \frac{m_{\mathrm{fibre}}}{V_{\mathrm{fibre}}} = \frac{L\omega}{LA_0} = \frac{\omega}{A_0}. \tag{A.6}$$

On the other hand, the mass of the air inside the lumen is negligible compared to the mass of the fibre wall, which can be calculated by multiplying the volume of the fibre wall LA_w by the density of cellulose $\tilde{\rho}_{\mathrm{c}}$, *i.e.* $m_{\mathrm{fibre}} = LA_w\tilde{\rho}_{\mathrm{c}}$. Thus the bulk density can be expressed in an alternative form

$$\rho_{\mathrm{fibre}} = \frac{m_{\mathrm{fibre}}}{V_{\mathrm{fibre}}} = \frac{LA_w\tilde{\rho}_{\mathrm{c}}}{LA_0} = \frac{A_w\tilde{\rho}_{\mathrm{c}}}{A_w + A_l}. \tag{A.7}$$

Combining Eqs. (A.6) and (A.7), and solving for the ratio A_l/A_w, one gets

$$\frac{A_l}{A_w} = \frac{A_0\tilde{\rho}_{\mathrm{c}}}{\omega} - 1. \tag{A.8}$$

Now saturated fibres are considered that have their lumens filled by water. The water inside the lumen is forced to move with the fibre and is thus considered as bound water. The moisture ratio of bound water of a fibre MR_{b} is defined as the ratio of the mass of bound water to the mass of the fibre wall:

$$\mathrm{MR}_{\mathrm{b}} = \frac{A_l\tilde{\rho}_{\mathrm{w}}}{A_w\tilde{\rho}_{\mathrm{c}}}. \tag{A.9}$$

Using Eq. (A.8), the moisture ratio of bound water can be given as

$$\mathrm{MR}_{\mathrm{b}} = \left(\frac{A_0\tilde{\rho}_{\mathrm{c}}}{\omega} - 1\right) r. \tag{A.10}$$

where r is the density ratio of water and cellulose:

$$r = \frac{\tilde{\rho}_{\mathrm{w}}}{\tilde{\rho}_{\mathrm{c}}}. \tag{A.11}$$

The overall moisture ratio of a suspension is defined as the ratio of the total mass of water to the mass of oven-dried fibres (the mass of cellulose in the fibre walls). Notice that here the mass of water includes both the bound water inside the lumens and the free carrier water outside the fibres. A sample volume of suspension is considered here that has the total mass of $m = m_c + m_w$, where m_c is the mass of cellulose and m_w is the total mass of bound and free water. Thus the moisture ratio MR is:

$$\mathrm{MR} = \frac{m_w}{m_c} = \frac{m - m_c}{m_c} = \frac{1-c}{c}, \tag{A.12}$$

where c is the percentage consistency of the suspension, *i.e.* the ratio of the mass of cellulose to the total mass:

$$c = \frac{m_c}{m}. \tag{A.13}$$

The total volume of the sample V can be written in the form $V = V_w + V_c$ where V_w and V_c is the total volume occupied by water and cellulose (fibre walls), respectively. In addition, the total volume occupied by water can be written as $V_w = V_{wf} + V_{wb}$ where V_{wf} and V_{wb} is the volume filled by free water and bound water, respectively. Now the moisture ratio can be written in the form

$$\mathrm{MR} = \frac{m_w}{m_c} = \frac{V_w \tilde{\rho}_\mathrm{w}}{V_c \tilde{\rho}_\mathrm{c}} = \frac{\frac{V - V_{wf}}{V_c} V_w \tilde{\rho}_\mathrm{w}}{(V - V_{wf})\tilde{\rho}_\mathrm{c}} \tag{A.14}$$

The following identity holds for the volumes:

$$(V - V_{wf})V_w = (V - V_{wf} - V_c)V + V_{wf}V_c = V_{wb}V + V_{wf}V_c. \tag{A.15}$$

Inserting Eq. (A.15) into Eq. (A.14) results in

$$\mathrm{MR} = \frac{\frac{V_{wb}}{V_c} V \tilde{\rho}_\mathrm{w} + V_{wf}\tilde{\rho}_\mathrm{w}}{(V - V_{wf})\tilde{\rho}_\mathrm{c}} = \frac{\frac{V_{wb}\tilde{\rho}_\mathrm{w}}{V_c\tilde{\rho}_\mathrm{c}} + \frac{V_{wf}}{V}\frac{\tilde{\rho}_\mathrm{w}}{\tilde{\rho}_\mathrm{c}}}{1 - \frac{V_{wf}}{V}}. \tag{A.16}$$

The first term in the numerator of Eq. (A.16) equals the moisture ratio of bound water $\mathrm{MR_b}$, and $\phi = V_{wf}/V$ is the porosity of the suspension. Thus the moisture ratio can be written as

$$\mathrm{MR} = \frac{\mathrm{MR_b} + \phi r}{1 - \phi}. \tag{A.17}$$

Combining Eqs. (A.17) and (A.12) one can write the following correlation between the volume fraction of fibres ϕ_s and the consistency of the suspension,

$$\phi_\mathrm{s} = \frac{(\mathrm{MR_b} + r)c}{1 - (1 - r)c} \tag{A.18}$$

Furthermore, combining Eqs. (A.4) and (A.18) one gets the following expression for the consistency,

$$c_m = \frac{4\omega}{\pi d^2} \frac{(\mathrm{MR_b} + r)c}{1 - (1 - r)c}. \tag{A.19}$$

Equation (A.19) can be inverted to get the following expression for the consistency,

$$c = \left(\mathrm{MR_b} + r + (1-r)\frac{\pi d^2 c_m}{4\omega} \right)^{-1} \frac{\pi d^2 c_m}{4\omega}. \qquad (A.20)$$

Notice that it has been assumed in Eqs. (A.4), (A.19), and (A.20) that the fibres have circular cross-section.

Bibliography

[BA98] J.-F. Bloch and J.-L. Auriault. Heat transfer in nonsaturated porous media: modelling by homogenisation. *Transport in Porous Media*, (30):301–321, 1998.

[Bea72] J. Bear. *Dynamics of Fluids in Porous Media.* American Elsevier, New York, 1972.

[Bh50] W. Brecht and H. heller. A study of pipe friction losses of paper stock suspensions. *Tappi*, 33(9), 1950.

[Bre62] F. P. Bretherton. Slow viscous motion round a cylinder in a simple shear. *J. Fluid Mech.*, 12:591–613, 1962.

[Bri47] H. C. Brinkman. A calculation of viscous force exerted by a flowing fluid on a dense swarm of particles. *Appl. Scient. Res. Ser. A*, 1:27–34, 1947.

[BS78] Yu. A. Buyevich and I. N. Shchelchkova. Flow of dense suspensions. *Prog. Aerospace Sci.*, 18:121–150, 1978.

[BT83] Ray E. Bolz and George L. Tuve, editors. *CRC handbook of Tables for Applied Engineering Science.* CRC, 2nd edition, 1983.

[Buy71] Yu. A. Buyevich. Statistical hydromechanics of disperse systems. part 1. physical background and general equations. *J. Fluid Mech.*, 49(3):489–507, 1971.

[Buy92a] Yu. A. Buyevich. Heat and mass transfer in disperse media - i. averaged field equations. *nt. J. Heat Mass Transfer*, 35(10):2445–2452, 1992.

[Buy92b] Yu. A. Buyevich. Heat and mass transfer in disperse media - ii. constitutive equations. *Int. J. Heat Mass Transfer*, 35(10):2453–2463, 1992.

[CB68] R. G. Cox and H. Brenner. The lateral migration of solid particles in poiseuille flow – i theory. *Chem. Engn Sci.*, 23:147–173, 1968.

[CFX94] Computational Fluid Services. *User Guide*, 1994.

[CH77] R. G. Cox and S. K. Hsu. The lateral migration of solid particles in a laminar flow near a plane. *Intl. J. Multiphase Flow*, 3:201–222, 1977.

[CM71] R. G. Cox and S. G. Mason. Suspended particles in fluid flow through tubes. *Ann. Rev. Fluid Mech.*, 3:291–316, 1971.

[CM94] P. Cherukat and J. B. McLaughlin. The inertial lift on a rigid sphere in a linear shear flow field near a flat wall. *J. Fluid Mech.*, 263:1–18, 1994.

[CP07] J. Chastanet and V. Pavan. Thermal behaviour of gas flows in micro porous media under klimkenberg conditions. Ecole Des Mines d'Albi, France, 2007. Eurotherm Seminar N81 Reactive Heat transfer in Porous Media.

[CTC96] C.T. Crowe, T.R. Troutt, and J.N. Chung. Numerical models for two-phase turbulent flows. *Annu. Rev. Fluid. Mech.*, 28:11–43, 1996.

[DAL90] D.A. Drew, G.S. Arnold, and Jr.R.T. Lahey. Relation of microstructure to constitutive equations. In D.D. Joseph and D.G. Schaeffer, editors, *Two phase flows and waves*, pages 45–56, 1990.

[DL79] D.A. Drew and R.T.Jr. Lahey. Application of general constitutive principles to the derivation of multidimensional two-phase flow equations. *Int. J. Multiphase Flow*, 5:243–264, 1979.

[Dod96] C. Dodson. Fiber crowding, fibre contacts, and fiber flocculation. *Tappi*, 79(9):211–216, 1996.

[Dre71] D.A. Drew. Averaged field equations for two-phase media. *Studies in Applied Mathematics*, 50:133–166, 1971.

[Dre76] D.A. Drew. Two-phase flows: Constitutive equations for lift and brownian motion and some basic flows. *Arch. Rat. Mech. Anal.*, 62(117), 1976.

[Dre83] D.A. Drew. Mathematical modeling of two-phase flow. *Ann. Rev. Fluid Mech.*, 15:261–291, 1983.

[Dre88] D. Drew. The lift force on a small sphere in the presence of a wall. *Chem. Engng Sci.*, 43:769–773, 1988.

[DS71] D.A. Drew and L.A. Segel. Averaged equations for two-phase flows. *Studies in Applied Mathematics*, 50(3):205–231, 1971.

[Duf76] G. D. Duffy. A review and evaluation of design methods for calculating friction loss in stock piping systems. *Tappi*, 59(8):124–127, 1976.

[Duf97] G. G. Duffy. The unique behaviour of wood pulp fibre suspensions. In 9^{th} *International Conference on Transport and Sedimentation of Solid Particles*, September 1997.

[Feu89] F. Feuillebois. Some theoretical results for the motion of solid spherical particles in a viscous fluid. In G. F. Hewitt, J. M. Delhaye, and N. Zuber, editors, *Multiphase Science and Technology*, volume 4, pages 583–789. Hemisphere, 1989.

[FHJ94] J. Feng, H. H. Hu, and D. D. Joseph. Direc simulation of initial value problems for the motion of solid bodies in a newtonian fluid. part 2. couette and poiseuille flows. *J. Fluid Mech.*, 277:271–301, 1994.

[FLU98] Fluent Inc. *User's Guide*, 1998.

[FR95] B. Ferréol and D. H. Rothma. Lattice-boltzmann simulations of flow through fontainebleau sandstone. *Transport in Porous Media*, 20:3–20, 1995.

[Gha95] G. K. Ghaddar. On the permeability of unidirectional fibrous media: A parallel computational approach. *Phys. Fluids*, 7(11):2563–2586, 1995.

[Haa] S. Haavisto. Private communication.

[Ham04] D. Hammarström. A model for simulation of fibre suspension flows. Licentiate Thesis, KTH, Stockholm, Sweden, 2004.

[Hap59] J. Happel. Viscous flow relative to arrays of cylinders. *AIChE J.*, 1959.

[Häm93] J. Hämäläinen. *Mathematical Modeling and Simulation of Fluid Flows in the Headbox of Paper Machines.* PhD thesis, University of Jyväskylä, Jyväskylä, Finland, 1993.

[HRGP03] P. Huber, J. C. Roux, N. Gelgacem, and C. Pierre. Suspension crowding for a general fibre-length distribution: application to flocculation of mixtures of short and long papermaking fibres. *Journal of Pulp and Paper Science*, 2003.

[HS89] G.-J. Hwang and H.H. Shen. Modeling the solid phase stress in a fluid-solid mixture. *Int. J. Multiphase Flow*, 15(2):257–268, 1989.

[HS91] G.-J. Hwang and H.H. Shen. Modeling the phase interaction in the momentum equations of a fluid-solid mixture. *Int. J. Multiphase Flow*, 17(1):45–57, 1991.

[Hwa89] G.-J. Hwang. *Modeling two-phase flows of a fluid and solid mixture.* PhD thesis, Clarkson University, 300 N.Zeeb Rd. Ann Arbor, MI 48106, 1989.

[Ish75] M. Ishii. *Thermo-fluid dynamic theory of two-phase flow.* Eyrolles, France, 1975.

[JJ86] G. W. Jackson and D. F. James. The permeability of fibrous porous media. *Can. J. Chem. Eng.*, 64:364, 1986.

[JL90] D.D. Joseph and T.S. Lundgren. Ensemble averaged and mixture theory equations for incompressible fluid-particle suspensions. *Int. J. Multiphase Flow*, 16:35–42, 1990.

[KD78] Møller K. and Duffy G. D. An equation for predicting transition-regime pipe friction loss. *Tappi*, 61:63–66, 1978.

[KKH+98] A. Koponen, D. Kandhai, E. Hellén, M. Alava, A. Hoekstar, M. Kataja, K. Niskanen, P. Sloot, and J. Timonen. Permeability of three-dimensional random fiber webs. *Phys. Rev. Lett.*, 80(4):716–719, 1998.

[KS92] R. J. Kerekes and C. J. Schell. Characterization of fibre flocculation regimes by a crowding factor. *Journal of Pulp and Paper Science*, 18(1):32–38, 1992.

[Kuw59] S. Kuwabara. The forces experienced by randomly distributed parallel circular cylinders or spheres in viscous flow at small reynolds numbers. *J. Phys. Soc. Japan*, 1959.

[LA85] D. Leighton and A. Acrivos. The lift force on a small sphere touching a plane in the presence of a simple shear flow. *J. Appl. Math. Phys.*, 36:174–178, 1985.

[Lad94] A. J. C. Ladd. Numerical simulations of particulate suspensions via a discretized boltzmann equation. part i. theoretical foundation. *J. Fluid Mech.*, 271:285, 1994.

[Lam75] H. Lamb. *Hydrodynamics.* Dover, 6th edition, 1975.

[LD76] P. F. W. Lee and G. D. Duffy. An analysis of the drag reducing regime of pulp suspension flow. *Tappi*, 59:119–122, 1976.

[Lea80] L. G. Leal. Particle motions in a viscous fluid. *Ann. Rev. Fluid Mech.*, 12:435–476, 1980.

[LL87] L. D. Landau and E. M. Lifshitz. *Fluid Mechanics*, volume 6 of *Course of theoretical physics.* Pergamon, 2nd edition, 1987.

[Luu] V.-M. Luukkainen. Private communication.

[Mas54] S. G. Mason. Fibre motion and floccation. *Pulp Paper Mag. Can*, 1954.

[McL91] J. B. McLaughlin. Inertial migration of a small sphere in linear shear flows. *J. Fluid Mech.*, 224:261–274, 1991.

[MD64] R. Meyer and Wahren D. On the elastic properties of three-dimensional fibre networks. *Svensk Papperstidning*, 1964.

[MDT71] K. Møller, G. D. Duffy, and A. L. Titchener. The laminar plug flow regime of paper pulp suspenions in pipes. *Svensk Papperstidning*, (24):829–835, 1971.

[MRC02] Rahman M., Verhoeven R., and Brebbia C.A., editors. *Advances in Fluid Mechanics IV*, pages 207–216. WIT Press, 2002.

[Myr98a] B. Myréen. Modelling the flow of pulp suspensions in pipes. part 1. *Paperi ja Puu - Paper and Timber*, (5):497–504, 1998.

[Myr98b] B. Myréen. Modelling the flow of pulp suspensions in pipes. part 2. *Paperi ja Puu - Paper and Timber*, (7):791–798, 1998.

[Nig79] R.I. Nigmatulin. Spatial averaging in the mechanics of heterogeneous and dispersed systems. *Int. J. Multiphase Flow*, 5:353–385, 1979.

[PP57] I. Proudman and J. R. A. Pearson. Expansions at small reynolds numbers for the flow past a sphere and a circular cylinder. *J. Fluid Mech.*, 2:237–262, 1957.

[QdL92] Y. H. Qian, D. d'Humiéres, and P. Lallemand. Lattice bgk models for navier-stokes equation. *Europhys. Lett.*, 17:479–484, 1992.

[RSM92] Benzi R., Succi S., and Vergassole M. The lattice boltzmann equation: Theory and applications. *Phys. Rep.*, 222(3):145–197, 1992.

[SA72] T. J. Stenuf and K. P. Anumolu. Pluf flow of fibre suspensions. *Tappi*, 55(9):1387–1388, 1972.

[Saf65] P. G. Saffman. The lift on a small sphere in a slow shear flow. *J. Fluid Mech.*, 22:385, 1965.

[Sal97] J. Salmela. Kuitususpensiovirtauksen seinämäkerroksen paksuusmittaus. Pro Gradu Thesis, University of Jyväskylä, Jyväskylä, Finland, 1997.

[SK88] R. M. Soszynski and R. J. Kerekes. Elastic interlocking of nylon fibres suspended in liquid. *Nordic Pulp and Paper Research Journal*, (4):172–179, 1988.

[Sko93] P. Skordos. Initial and boundary conditions for the lattice boltzmann method. *Phys. Rev. E*, 48(6):4823 – 4842, 1993.

[Sl91] S. Skali lami. *Contribution a l'etude de l'ecoulement de pate a papier interaction flocculation-turbulence.* PhD thesis, l'Institut National Polytechnique de Lorraine, 1991.

[Soo90] S.L. Soo. *Multiphase Fluid Dynamics.* Science Press, Beijing, 1990.

[SS62] G. Segré and A. Silberberg. Behaviour of macroscopic rigid spheres in poiseuille flow. part 2. experimental results and interpretation. *J. Fluid Mech.*, 14:136–157, 1962.

[TD64] N. Thaleń and Wahren D. Shear modulud and ultimate shear strength of some paper pulp fibre networks. *Svensk Papperstidning*, 1964.

[TIS88] TIS0410-14. Generalized method for determining the pipe friction loss of flowing pulp suspensions. Technical report, Tappi, 1988.

[VC76] P. Vasseur and R. G. Cox. The lateral migration of a spherical particle in two-dimensional shear flows. *J. Fluid Mech.*, 78:385–413, 1976.

[VC77] P. Vasseur and R. G. Cox. The lateral migration of spherical particles sedimenting in a stagnant bounded fluid. *J. Fluid Mech.*, 80:561–591, 1977.

[Wea74] R.C. Weast, editor. *CRC handbook of chemistry and physics.* CRC Press, 55th edition, 1974.

[Whi94] F. M. White. *Fluid Mechanics.* McGraw-Hill, New York, 3rd edition, 1994.

[Whi06] F. M. White. *Viscous fluid flow.* McGraw-Hill, New York, 3rd, international edition edition, 2006.

[XA05] H. Xu and C. K. Aidun. Characteristics of fiber suspension flow in a rectangular channel. *Int. J. Multiphase Flow*, 2005.